Dissertation

Deciphering the Intricate Interaction Network in the ß-Catenin Destruction Complex – The Axin-1 Paradigm

submitted by

Sarah STRYECK MSc

for the Academic Degree of

Doctor of Philosophy (PhD)

at the

Medical University of Graz

Gottfried Schatz Research Center for Cell Signaling, Metabolism & Aging

Molecular Biology & Biochemistry

under the supervision of

Prof. Dr. Tobias MADL

2019

Declaration

I hereby declare that this thesis is my own original work and that I have fully acknowledged by name all of those individuals and organizations, that have contributed to the research for this thesis. Due acknowledgement has been made in the text to all other material used. Throughout this thesis and in all related publications I followed the "Standards of Good Scientific Practice and Ombuds Committee at the Medical University of Graz".

Parts of this thesis have been published in:

Sarah Stryeck, Angela Horvath, Bettina Leber, Vanessa Stadlbauer, Tobias Madl. *NMR spectroscopy enables simultaneous quantification of carbohydrates for diagnosis of intestinal and gastric permeability.* **Scientific Reports**, doi: 10.1038/s41598-018-33104-8 (2018)

Sarah Stryeck, Ruth Birner-Grünberger, Tobias Madl. *Integrative metabolomics as emerging tool to study autophagy regulation.* **Microbial Cell** 4, doi: 10.15698/mic2017.08.584 (2017)

Co-authors that contributed to the data in this thesis:

Angela Horvath

Department of Internal Medicine, Division of Gastroenterology and Hepatology, Medical University of Graz

Bettina Leber

Department of Surgery, Division of Transplantation Surgery, Medical University of Graz

Vanessa Stadlbauer-Köllner

Department of Internal Medicine, Division of Gastroenterology and Hepatology, Medical University of Graz

Ruth Birner-Grünberger

Research Unit for Functional Proteomics and Metabolic Pathways, Institute of Pathology, Medical University of Graz

Tobias Madl

Gottfried Schatz Center for Cell Signaling, Metabolism and Aging, Medical University of Graz

I confirm that all co-authors have agreed to use their data in my thesis (signed confirmations are availabe). I have included the permission to reprint data from the open access journal Scientific Reports and the open access journal Microbial Cell in the appendix.

Date …….

Acknowledgements

Sarah Stryeck received funding from FWF (P 28854) and the Medical University of Graz through the PhD Program Molecular Medicine.

Sarah Stryeck is a recipient of a DOC Fellowship of the Austrian Academy of Sciences at the Gottfried Schatz Research Center for Cell Signaling, Metabolism and Ageing.

Sarah Stryeck conducted a research stay at the UMC Utrecht in the group of Madelon Maurice which has been funded by the Marietta-Blau Fellowship (OEAD), by the Exzellenzstipendium (IV Kärnten) and by the Forschungsstipendium (Medical University of Graz).

I thank Tobias Madl, Madelon Maurice and Klaus Zangger for being part of my thesis committee, and for supervising/discussing my project in our meetings.

I am very thankful for all the people that contributed to the work described in this thesis: In the Gottfried Schatz Research Center for Cell Signaling, Metabolism and Aging, the Graier group, namely **Benjamin Gottschalk**, helped with their expertise in super-resolution microscopy in order to obtain SIM images. **Gerd Leitinger, Maximilian Schinagl and Karin Kornmüller** assisted with electron microscopy imaging.
At the University Medical Center in Utrecht, The Netherlands, **Madelon Maurice and her group** helped a lot by introducing all different cell biology techniques used in this thesis. **Eline van Kappel** gave rise to the project with her preliminary observations and I thank **Alba Cristobal Gonzalez de Durana** for the nice teamwork on the Axin-1 project.

Finally, I also thank the whole **Madl group** for the great working atmosphere, for the thrilling discussions about our projects and our after work activities. I thank **Tobias** for the opportunity to do my PhD studies in his group and for his great scientific input when it comes to planning projects, applying for grants and writing papers.

Apart from all the work related help I had during my PhD, I am very grateful for all the people around me who supported and understood me and who listened to me during the last years.

Meli, Mama, Isolde - Thank you for all the support and for encouraging me to do it my way. **Christiane and Corina** - Thanks for our great personal and scientific discussions. I admire your positive attitudes although times are not always easy – I could learn a lot from you. **Gesa** – We're in the same boat ☺ I highly enjoyed sharing the office with you. Thank you for the great discussions, for your support, your understanding at any time! **Emil** – thank you so much for our bioinformatics sessions and our discussions about career and science. Keep on your motivation! ☺ **Therese** – I greatly enjoyed the time with you in the lab and I am happy that our friendship also lasts in girls' night outs and boulder sessions! **Anna and Denise** – you both made the lab a great place. I will miss being in your office and forgetting the time chatting with you ☺ **Andrea** – I cannot say how much I enjoyed working in your immediate vicinity. You are a great teacher, understander and coach. **Dagmar** – I really appreciate your loving kindness and your sympathetic ear that you have for everybody.

Roman – I truly thank you from the bottom of my heart for your support during the years of my studies. You were there... on Sundays at 8 am with error messages on the SampleJet, at midnight to do the last titration point, for six months in Utrecht. You were there in every hour of joy, excitement, frustration and sadness. A thousand words cannot describe how much you mean to me. Your encouragement and your understanding helped me to handle each and every situation. It would not have been possible without you. Thank you! ♥

Table of content

DECLARATION 2

ACKNOWLEDGEMENTS 4

ABBREVIATIONS AND DEFINITIONS 11

ZUSAMMENFASSUNG 15

ABSTRACT 17

AIMS AND MOTIVATION 19

INTRODUCTION PART I 22

Membrane-less organelles in cells 22

Mis-regulation of phase separation in disease 23

Axin-1 as model system for phase separation in cancer 24

Regulation of Canonical Wnt-signaling pathway 26

Functional details of the ß-catenin destruction complex 28

Axin-1 regulation by post-translational phosphorylation 31

Wnt signaling and diseases 33

Central aim 34

INTRODUCTION PART II 35

NMR-based metabolomics 35

Setup of metabolomics studies 36

Data analysis in NMR-based metabolomics studies 38

Liver cirrhosis 40

Triple-sugar test for liver cirrhosis patients 40

Detection of carbohydrates in urine 41

Central aim 42

MATERIAL AND METHODS PART I 43

Plasmids 43

Primers 45

Protein production 46

Protein purification 46

NMR assignment experiments 48

NMR relaxation experiments 48

Secondary chemical shifts 49

NMR interaction studies 49

Chemical shift perturbations 50

NMR phosphorylation assays 50

Fluorescence anisotropy 50

Turbidity experiments 51

Electron microscopy 51

Differential interference contrast microscopy 51

Isothermal Titration Calorimetry 52

Small-angle X-ray scattering 52

Sequence conservation analysis 53

Cell culture 53

ß-catenin dependent luciferase assays 54

Western blotting 54

Immunofluorescence microscopy 55

Structured Illumination Microscopy 55

MATERIAL AND METHODS PART II 56

Participants 56

Collection of sample material 57

List of reagents 57

Preparation of urine 57

Nuclear Magnetic Resonance Spectroscopy 58

Data processing 60

Principal component analysis 60

Metabolite determination 61

Relaxation-enhancement experiments 61

RESULTS – FINDINGS PART I 62

Axin-1^{DIX} domain harbors BSs within the Axin-1^{IDR} 62

Axin-1 auto-inhibition does not interfere with oligomerization 74

Axin-1^{DIX} binding does not interfere with ß-catenin binding 76

Dephosphorylation does not dissolve *puncta* 79

Deletion of single BSs is not sufficient to dissolve *puncta* 84

BS deletions restore *puncta* formation in presence of a cancer mutation 85

Axin-1 performs phase separation 91

RESULTS – FINDINGS PART II 99

JRES as homo-nuclear decoupling experiment 99

Identification of reference compounds in a urine sample 102

Quantification of carbohydrates in urine 105

DISCUSSION PART I 109

Axin-1 and cancer 109

Phase separation in Wnt signaling 114

Perspective/open questions 115

Restoration of puncta formation as a drug target 117

Role of the Hrr in Axin-1 117

Relevance of overexpression model 119

Evolutionary conservation of Axin-1 119

DISCUSSION PART II 122

NMR spectroscopy as a diagnostic tool 122

PRE agents 123

BIBLIOGRAPHY 125

APPENDIX 143

Buffers and solutions 143

List of publications and licences 147

Abbreviations and Definitions

$^{2}H_2O$	deuterium oxide
ß-TrCP	F-box/WD repeat-containing protein 1A
µM	micromolar
ADP	adenosine diphosphate
ALS	amyotrophic lateral sclerosis
APC	adenomatous poliposis coli
ATP	adenosin triphosphate
Axin-1^{DIX}	Dishevelled/Axin domain of Axin-1
Axin-1^{IDR}	intrinsically disordered region of Axin-1
Axin-1^{RGS}	regulator of G-protein signaling domain of Axin-1
BCD	ß-catenin binding domain
BME	ß-mercaptoethanol
BS	binding site
BSA	bovine serum albumine
CK1	casein kinase 1
CPMG	Carr-Purcell-Meiboom-Gill sequence
CSP	chemical shift perturbations
DAXX	death domain associated protein
DAPI	4′,6-diamidin-2-phenylindol
DIC	differential interference contrast
DIPSI	decoupling in presence of scalar interactions
Dsh	Dishevelled
DTT	dithiothreitol
E816G	amino acid exchange glutamic acid-to-glycine on position 816
E.coli	*Escherichia coli*
F802A	amino acid exchange phenylalanine-to-alanine on position 802
FRAP	fluorescence recovery after photobleaching

FRET	förster resonance energy transfer
FTD	frontotemporal dementia
FtsZ	filamenting temperature-sensitive mutant Z
FUS	fused in sarcoma
fw	forward
Fz	Frizzled
GFP	green fluorescent protein
GSK3ß	glycogen synthase kinase 3ß
HEK293T	human embryonic kidney 293T cells
HeLa	Henrietta Lacks cells
HLY78	4-ethyl-5-methyl-5,6-dihydro-[1,3]dioxolo[4,5-j]phenanthridine
hnRNPA1	heterogeneous nuclear ribonucleoprotein A1
HPLC	high performance liquid chromatography
Hrr	histidine-rich region
HSQC	heteronuclear single quantum coherence spectroscopy
IPTG	isopropyl-β-D-thiogalactopyranosid
JRES	^{1}H homo-nuclear J-resolved 2D correlation experiments
kDa	kilo dalton
LB	Luria Bertani
LC	low complexity
LEF	lymphoid enhancer binding factor 1
LLPS	liquid-liquid phase separation
LRP5/6	low-density lipoprotein-receptor related protein 5/6
min	minute
mL	milliliter
mM	millimolar
mRNA	messenger ribonucleic acid
MS	mass spectrometry
NaCl	natrium chloride
ng	nanogram

NH_4Cl	ammoniumchloride
nM	nanomolar
nm	nanometer
NMR	nuclear magnetic resonance
noesy	nuclear overhauser enhancement spectroscopy
NTA	nitrilotriacetic acid
O-PLS-DA	orthogonal partial least square discriminant analysis
OD_{600}	optical density at 600 nm
PBS	phosphate buffered saline
PCA	principal component analysis
PFA	paraformaldehyde
PRE	paramagnetic relaxation enhancement
RFP	red fluorescent protein
RNA	ribonucleic acid
rpm	rotations per minute
RT	room temperature
rv	reverse
s	second
SEC	size exclusion chromatography
Ser	serine
SIM	structured illumination microscopy
SPOP	speckle-type POZ protein
$T_{1/2}$	half-life
T_1	spin lattice-relaxation
TCF	T-cell specific transcription factor
TDP-43	TAR DNA binding protein 43
TEV	tobacco etch virus
Thr	threoinine
TLE	transducin-like enhancer protein
TSP	3-(trimethylsilyl)propionic-2,2,3,3-d_4-acid

USP34	Ubiquitin-carboxyl-terminal hydrolase 34
V801A	amino acid exchange valine-to-alanine on position 801
Val	valine
Wnt	Wingless related integration site
YAP/TAZ	Yes-Associated Protein/Transcriptional co-activator with PDZ-binding motif

Zusammenfassung

In den letzten Jahren gab es vermehrt Beweise, dass in Zellen membranlose Organellen im Zytoplasma und im Nukleus vorkommen, welche für die Zellen von großer Bedeutung sind. Proteine, welche die Fähigkeit besitzen phasengetrennte Kondensate auszubilden, umfassen z.B. hnRNPA1, FUS oder TDP-43. Diese Proteine wurden in mutierter oder de-regulierter Form auch schon im Zusammenhang mit neurodegenerativen Erkrankungen durch die Ausbildung von nicht-nativen Proteinaggregaten in Neuronen beschrieben. Die Bedeutung dieser flüssig-flüssig Phasentrennung in Krebserkrankungen ist jedoch noch unklar. Daher untersuche ich in meiner Doktorarbeit das Protein Axin-1, welches Phasentrennung im Zytoplasma durchführt und schon mit Krebserkrankungen assoziiert wurde. Es ist ein Schlüsselelement im sogenannten ß-Catenin Destruktionskomplex, welcher den Wnt Signalpfad reguliert. In der Literatur ist bekannt, dass sich Axin-1 über intramolekulare Interaktionen autoreguliert. Diese multivalenten Interaktionen wurden außerdem schon als Kennzeichen von flüssig-flüssig Phasentrennung beschrieben.

Das zentrale Ziel dieser Arbeit ist einen Beitrag zum Verständnis der Axin-1 Selbstregulierung zu leisten, um auch die Ausbildung der makromolekularen phasengetrennten Kondensate und den Effekt von Krebsmutanten darauf zu verstehen. Daher verwendete ich eine Kombination aus strukturbiologischen und zellbiologischen Techniken, um die Auto-Regulierung des Proteins zu untersuchen.

Die Ergebnisse des Projektes zeigten, dass drei verschiedene Regionen in der Axin-1^{IDR} mit einer Bindestelle an der Axin-1^{DIX} interagieren. Die Oberfläche der Bindungsstelle an der strukturierten Axin-1^{DIX} überlappt nicht mit der Oberfläche, die für die Axin-1^{DIX} Oligomerisierung wichtig ist. Im Widerspruch zur Literatur steht unsere Entdeckung, dass die Axin-1^{DIX} Interaktion mit der Axin-1^{IDR} nicht zu einer Verdrängung von ß-Catenin führt, da sich die Lokalisation der Bindestellen an der Axin-1^{IDR} unterscheidet. Außerdem konnten wir zeigen, dass post-translationale Phosphorylierung von Axin-1 zwar die Aktivität des Proteins reguliert, nicht aber die Ausbildung der phasengetrennten Kondensate. Schlussendlich wurden mit einer

Krebsvariante des Proteins, welche eine Mutation in der Axin-1^{DIX} Bindestelle aufweist, Rollen der Axin-1^{IDR} Bindestellen analysiert.
Mit dieser Arbeit wurden wichtige intramolekulare Interaktionen im Protein Axin-1 aufgeklärt. Die Daten in dieser Arbeit sind daher essentiell um die Bedeutung von flüssig-flüssig Phasentrennung in Krebserkrankungen zu verstehen.

Im zweiten Kapitel der Arbeit wird eine Methodenentwicklung im Bereich der NMR Spektroskopie erläutert. Leberzirrhose ist ein häufiger Endpunkt von Erkrankungen der Leber und unter anderem zählt eine erhöhte Magen- und/oder Darmpermeabilität zu den klinischen Symptomen. Durch die orale Verabreichung von Zuckerlösungen und der Bestimmung der Konzentrationen im Urin kann diese erhöhte Durchlässigkeit diagnostiziert werden. Momentan fehlt jedoch eine zuverlässige Methode für die Quantifizierung der Kohlenhydrate.
Das Ziel dieser Arbeit war mithilfe von NMR Spektroskopie eine Methode zu entwickeln, welche die zuverlässige und schnelle Bestimmung der Zucker im Urin ermöglicht.
In den Ergebnissen konnten wir zeigen, dass sogenannte JRES Experimente eine gute Methode sind, um in einer komplexen Matrix wie Urin die Zucker ohne Zweifel zu identifizieren und zu quantifizieren. Diese Methode stellt eine gute Alternative zu den bisherigen Techniken für die Zuckerbestimmung dar und könnte durch die geringen Messzeiten auch von klinischer Bedeutung werden.

Abstract

During the last years, emerging evidence on the presence and importance of so-called membrane-less organelles in the cytoplasm but also in the nucleus of eukaryotes arose. Proteins capable of forming phase separated condensates (e.g. hnRNPA1, FUS, TDP-43) have already been linked to neurodegeneration due to formation of non-native protein aggregates in neuronal cells. The importance of liquid-liquid phase separation (LLPS) in cancer diseases still remains elusive. Therefore, I studied in my PhD project the protein Axin-1, which phase separates and which has already been linked to cancer diseases. It is a key element in the ß-catenin destruction complex, which regulates canonical Wnt signaling. In the literature, it has already been reported, that Axin-1 regulates its activity via self-binding. Such multivalent interactions are also a hallmark of LLPS.

The central aim of this thesis is to contribute to the current understanding of Axin-1 auto-regulation, the formation of macromolecular assemblies within the cytoplasm (so-called *puncta*) and the effect of cancer mutations on those processes. Hereby I used a combination of structural biology and cell biology techniques in order to decipher intra-molecular interaction within the protein Axin-1.

The key findings of the project were that three different regions Axin-1^{IDR} interact with the Axin-1^{DIX}. The interaction interface on the Axin-1^{DIX} was the same for all three Axin-1^{IDR} fragments, but it differs from the Axin-1^{DIX} oligomerization interface. In contrast to current assumptions in literature, the Axin-1^{DIX} interaction does not displace ß-catenin, since the binding sites on the Axin-1^{IDR} differ. In addition, post-translation phosphorylation, which is an important regulatory modification of the protein, regulates its activity, but is not sufficient to dissolve *puncta*. Finally, a cancer variant of the protein with a mutation located in the Axin-1^{DIX}, E816G, in the Axin-1^{DIX}-Axin-1^{IDR} interaction interface has been studied, and revealed an important role for the Axin-1^{IDR} binding sites.

During this thesis, intramolecular interactions within Axin-1 are studied, binding sites are mapped and effects of a cancer mutation in the binding interface are studied. Those

data reveal important features for the phase separation of Axin-1 and are therefore essential in order to understand the importance of condensate formation in cancer.

In the second chapter of my work I focus on a method development in NMR spectroscopy. Liver cirrhosis is one of the common end points of liver diseases. Besides other symptoms, increased gastric or intestinal permeability is one of the hallmarks of advanced liver damage. By oral administration of carbohydrate solutions and the detection thereof in urine, increased permeability can be diagnosed. However, techniques for sugar detection and quantification are limited, due to interfering substances or long measurement times.

The main aim of this project was to develop a NMR-based method in order to enable a fast and robust quantification of carbohydrates in urine.

In our results we were able to show that JRES experiments are a useful tool for the reliable identification and quantification of the carbohydrates.

This method builds a good alternative to commonly available techniques and might become an interesting approach for clinical applications.

Aims and motivation

In this thesis I describe two projects I investigated during my PhD studies, and provide a collection of all collaboration projects I was involved in during four years at the Medical University of Graz. For all those projects I used structural biology methods, such as solution NMR spectroscopy, fluorescence anisotropy or isothermal titration calorimetry in order to answer specific research questions. All projects intended to decipher unprecedented mechanisms in signal transduction, and metabolism research.

In part I of this thesis, I elaborate on Axin-1, which is a central protein of the ß-catenin destruction complex in the Wnt signal transduction pathway. Mutant variants of the protein have already been linked to cancer/neoplastic diseases. Since multivalent binding events were discovered in the work of my thesis, which remind of the multivalency that is needed in phase separation, and since it is described that Axin-1 forms macromolecular protein assemblies in the cytoplasm, we hypothesize that the protein also performs phase separation. Here, we investigate also the role of cancer mutations on phase separation, and speculate about a potential contrary role of functional LLPS for cancers compared to neurodegenerative diseases. (Fig. 1)

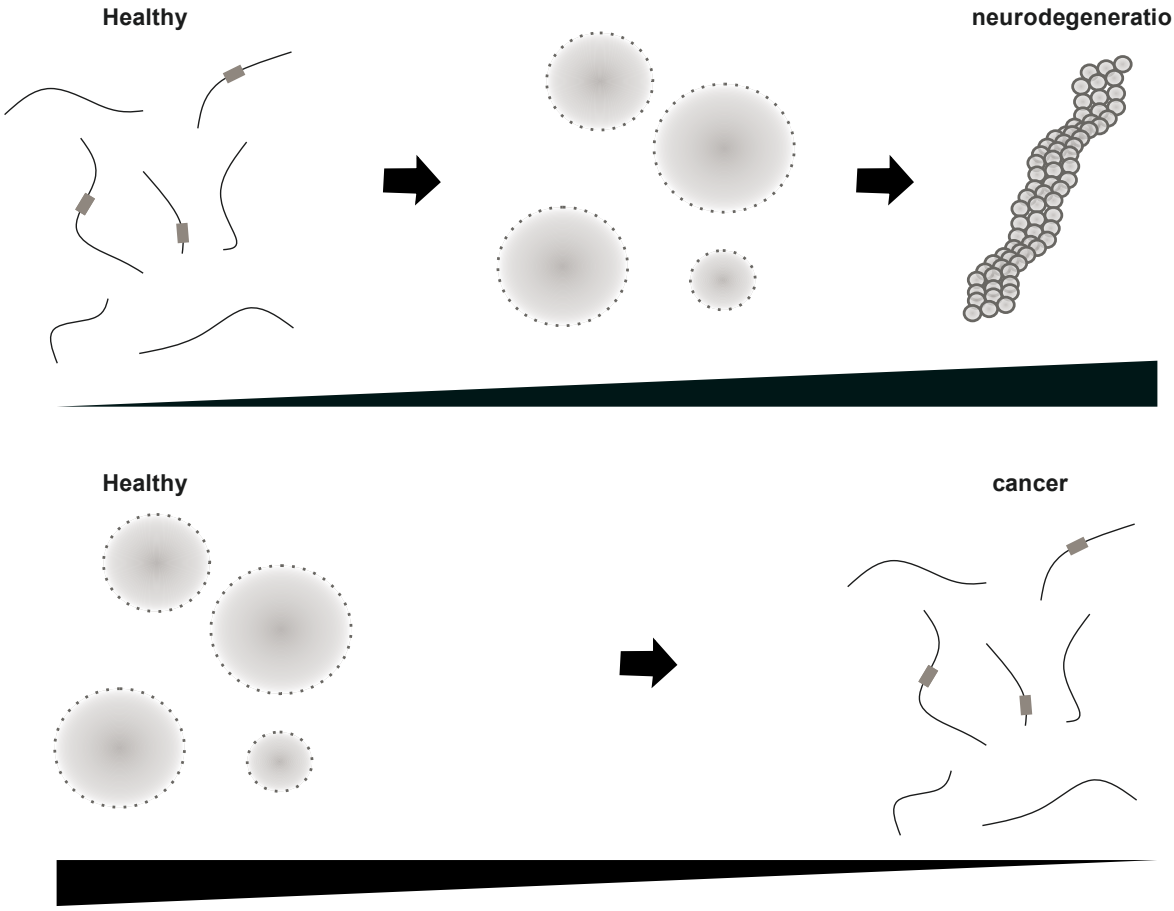

Figure 1: Model for phase separation in cancer

For neurodegeneration it has already been shown, that liquid droplet formation acts as a seed and thereby promotes protein aggregation and fiber formation. In contrast to that, we hypothesize that tumor suppressor proteins need LLPS, which provides an active environment for proteins. In presence of cancer mutations, phase separation is disrupted and tumor suppressor proteins are inactive.

In part II of this thesis, I present a method for the detection of different carbohydrates in urine. In clinics, carbohydrates are administered to liver cirrhosis patients in order to detect increased gastric or intestinal permeability. However, there is a lack of fast and reliable methods to quantify excreted carbohydrates in urine. Therefore, a NMR-based setup was used for the reliable quantification of carbohydrates which also brings potential for high-throughput applications in clinics. Apart from liver cirrhosis, increased intestinal permeability is an important parameter for celiac disease, Crohn's disease, type 1 diabetes and food allergies.(1) (Fig. 2) NMR-based metabolomics is an emerging technique, which provides essential analytical robustness and reproducibility, which is important for clinical applications.(2, 3) Therefore, NMR spectroscopy has already been used for numerous applications such as lipoprotein determination (4) or newborn screening for metabolic disorders.(5, 6)

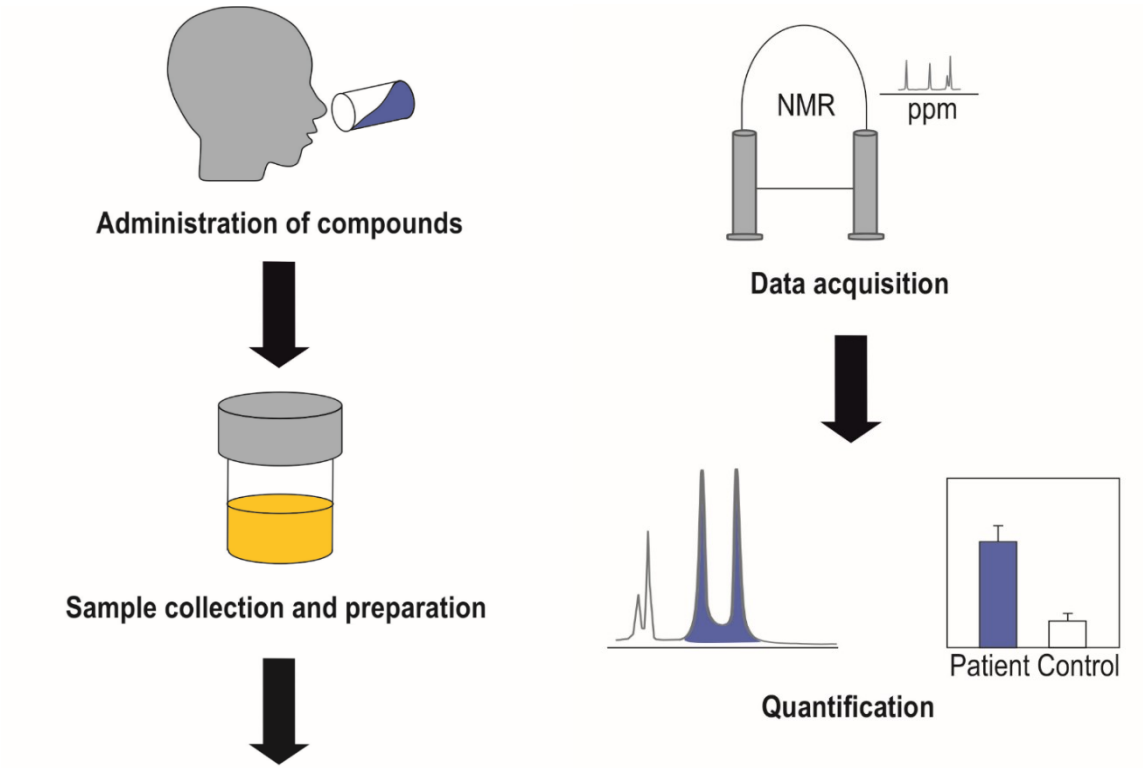

Figure 2: Workflow for NMR-based sugar quantification in urine

Introduction Part I

Membrane-less organelles in cells

Eukaryotes harbor, in contrast to prokaryotes, a highly organized compartment structure in the cytoplasm enabling tight regulation of metabolism but also signaling which is needed for proper cellular function. Those compartments comprise membrane-bound eukaryotic organelles like mitochondria, endoplasmic reticulum or lysosomes.(7) During the last years, emerging evidence on the presence and importance of so-called membrane-less organelles in the cytoplasm but also in the nucleus of eukaryotes arose. Examples of nuclear membrane-less organelles include nuclear speckles and the nucleolus, whereas cytoplasmic organelles lacking a membrane coating are so-called stress granules and processing bodies. Those types of organelles have already been studied in detail and are inevitable for processes like control of gene expression machinery, ribosomal subunit synthesis, stress response and mRNA turnover, respectively.(8-10) However, all of those phase separated assemblies are made up by different molecules/proteins, which makes extensive studies on them necessary. Nowadays, more and more membrane-less organelles are discovered and their regulation and function is studied in detail.(11-15) Those membrane-less organelles are termed in different ways, including biomolecular condensates, liquid droplets or stress granules. However, all those expressions intend to address assemblies formed by LLPS.

Membrane-less organelles consist of proteins or proteins and RNA molecules that perform LLPS. Hereby non-stoichiometric assemblies of those proteins (homo- or heteroassemblies) or proteins and RNA molecules (including cofactors) convene and form special scaffolds that separate from the cytoplasm or nuclear environment and share similarities to gels. Thereby, biomolecular condensates provide a stabilizing environment for RNA molecules. The main hallmarks of those condensates include multivalent interactions of scaffold proteins, which are important proteins for the assembly of multiprotein/RNA complexes, concentration-dependent formation,

dynamic exchange, and chemical properties distinct from the environment.(16-20) Multivalent interactions of proteins within the droplets occur via folded binding domains, disordered regions or even only short sequence motifs with a few key residues. Cooperative homo- or heterotypic non- covalent interactions of those domains/motifs give rise to phase separated droplets.(21) However, those multivalent interactions need a certain concentration threshold of the molecules involved in the interactions in order to elicit condensate formation by liquid demixing. In turn, decreased protein concentrations will reduce the occurrence of interactions and therefore dissolve the droplets again.(22) Despite the complicated network in protein complexes within phase separated membrane-less organelles due to multivalent interactions, they remain highly dynamic and exchange steadily with the environment.(11) Dynamics of those condensates can also be tightly regulated. For instance, LAF-1 (ATP-dependent RNA helicase laf1) droplets demonstrate increased molecular dynamics in presence of RNA.(16, 23) However, these dynamics follow a certain order, since phase separated proteins create distinct chemical properties which are important for the function of the proteins. These chemical properties of phase separated assemblies have already been described for different systems, for instance FtsZ (Filamenting temperature-sensitive mutant Z). Filaments of FtsZ relocate upon depolymerization, suggesting a shift according to microenvironments present in the condensates.(14, 24-26)

Mis-regulation of phase separation in disease

As already indicated in several studies, phase separation is essential for control of gene expression machinery, ribosomal subunit synthesis, stress response and mRNA turnover.(8-10) However, exaggerated multivalent interactions of proteins within liquid droplets can lead to incorrect assembly and therefore to protein aggregation. In line with this, proteins capable of forming phase separated condensates (e.g. hnRNPA1, FUS, TDP-43) have already been linked to neurodegeneration due to formation of non-native protein aggregates in neuronal cells.(11, 12, 15, 27) For example, RNA-binding protein FUS forms with its low complexity (LC) domains a hydrogel-like structure. In presence of a mutation in the nuclear localization signal or in absence of post-

translational arginine methylation, proper formation of phase separated organelles is disrupted in amyotrophic lateral sclerosis (ALS) or frontotemporal dementia (FTD), respectively. Hereby the dynamic protein assembly will undergo a transition to a fibrillary hydrogel, which is toxic for cells.(11-13)

Despite the current knowledge about the importance of proper regulation of phase separation in neurodegeneration, phase separated proteins involved in cancer and their regulation have not yet been well studied. Since proliferative and neurodegenerative diseases have already been shown to demonstrate contrary features in terms of (de-)regulation, e.g. arginine methylation, where cancer diseases are linked to hyper-methylation (28), whereas neurodegenerative diseases are mainly linked to hypo-methylation (11), it can be speculated that also the phenomenon of LLPS is contrary regulated in proliferative and neurodegenerative diseases. Bouchard et al. (2018) have already reported a disrupted condensate formation of the nuclear tumor suppressor speckle-type POZ protein (SPOP) in presence of cancer mutations. Hereby the interaction of mutant SPOP with death domain associated protein (DAXX) is disturbed, correlating with loss of function of the tumor suppressor protein.(29) This study suggests a crucial physiological role of phase separation and links it to cancer/neoplastic disorders. In contrast to neurodegeneration, reduced phase separation might be the trigger for cancer development.

Axin-1 as model system for phase separation in cancer

Apart from the protein SPOP, there are other proteins involved in cancer/neoplastic disorders, which have the ability to form macromolecular assemblies within cells. Examples include proteins in the canonical Wingless-related integration site (Wnt) signaling pathway, namely Axin-1 and Dishevelled (Dsh). They have been reported to form so-called *puncta* upon overexpression.(30-34) Those Axin-1 *puncta* share similarities with liquid droplets, however, they have never been termined alike. For Axin-1, those *puncta* have already been investigated using structured illumination microscopy (SIM).(31) Hereby super-resolution microscopy enables the observation of a network formed by the protein Axin-1-RFP upon overexpression, and a co-localization

of Adenomatous Polyposis Coli – GFP (APC), another member of the ß-catenin destruction complex. In addition, the dynamics of those *puncta* have already been measured using fluorescence recovery after photobleaching (FRAP) and indicate an exchange of proteins with the environment.(35) Based on these studies, it is conceivable, that formation of Axin-1 *puncta* is a process related or similar to phase separation and therefore further studies will provide more insights into cancer-related phase separation as already discussed in a recent review.(36)

In my PhD project, I focus on the rate-limiting key element of the ß-catenin destruction complex, Axin-1, in order to understand its physiological regulation via multivalent interactions, and deregulations of those in cancer.

Axin-1 is involved in canonical Wnt signaling, which is one of the most conserved signal transduction pathways in metazoans and essential for several physiological processes including cellular growth, differentiation and adult tissue homeostasis.(37) In mammals, Wnt signaling activity is essential for dorsoventral axis formation in early embryo development and, in later embryo development, for dorsoventral formation of the central nervous system. In fish and frogs, organizing centers are formed by ß-catenin dependent Wnt signaling.(37) Even after birth, Wnt signaling performs different functions of vital importance. For instance, the fate of specification of certain cell types is determined by Wnt signaling events. Human embryonic stem cells develop to cells having hematopoietic potential by activation of Wnt signaling. Progenitor cells can differentiate to, for example, cardiac or muscle cells.(38, 39) Furthermore, Wnt signaling plays a crucial role in mitosis.(40) In addition, Wnt signaling is involved in the establishment of hair follicles, but also in osteoblast maturation and in controlling cell fate along the crypt-villus axis in the gut. Finally, it plays a crucial role in stem cell self-renewal.(41-44) Those essential functions of Wnt signaling implicate that the signal transduction pathway has to be tightly regulated, and that deregulations can result in proliferative diseases.

Regulation of Canonical Wnt-signaling pathway

The canonical Wnt-signaling pathway involves the regulatory degradation of the protein ß-catenin, which is a transcriptional coactivator for the T-cell factor/lympoid enhancer factor (TCF/LEF) family of transcription factors. Degradation of ß-catenin is mediated by the ß-catenin destruction complex consisting of the proteins APC, the scaffold protein Axin-1, Casein Kinase 1 (CK1) and Glycogen Synthase Kinase 3 α and ß (GSK3 α and ß). The destruction complex-mediated reduction of intra-cellular levels of free ß-catenin results in a decreased transcriptional output of Wnt signaling regulated target genes which in turn has a crucial effect on physiological processes.(45-48) Wnt signaling is, in common with other signal transduction pathways, not constitutively active.

The Wnt 'on state' refers to a cellular condition where ß-catenin activates transcription of target genes.(Fig. 3) Upon binding of a so-called Wnt ligand (secreted, hydrophobic glycoprotein) (39) to the Frizzled (Fz) receptor on the plasma membrane, downstream signaling is activated. This binding event induces the translocation of the ß-catenin destruction complex, including Axin-1, to the plasma membrane where it binds low-density lipoprotein receptor-related protein 5/6 (LRP5/6). The cytoplasmic phosphoprotein Dsh is also recruited to the membrane via this signaling cascade and binds to Axin-1 and Fz. These processes inhibit the activity of GSK3ß, which in further consequence prevents phosphorylation, subsequent ubiquitination, and proteasomal degradation of ß-catenin by GSK3ß and F-box/WD repeat-containing protein 1A (ß-TrCP), respectively. Due to the inhibition of the destruction complex, ß-catenin accumulates in the nucleus where it binds to the TCF/LEF family of transcription factors. This binding event leads to expression of their biological numerous target genes by different mechanisms. Possible regulatory mechanisms are displacement of transducin-like enhancer protein (TLE)/Groucho repressors from TCF/LEF but also recruitment of co-activators by ß-catenin.(42, 43, 45-47, 49, 50) Targets include for example proteins involved in mitosis (Cyclin D1), in transcriptional regulation (MYC) and also in Wnt signaling (ß-TrCP, Frizzled and TLE/Groucho). Many of these target genes show putative TCF binding sites.(51-53) The absence of Wnt ligands translates

into low concentrations of nuclear ß-catenin and reduced transcriptional output. This is achieved by efficient trapping of free ß-catenin in the cytosolic ß-catenin destruction complex, which is no longer recruited to the plasma membrane, and subsequent ß-catenin phosphorylation, ubiquitination and proteosomal degradation. Current knowledge indicates a sequential phosphorylation of the N-terminal region of ß-catenin by kinases CK1 (Ser45) and GSK3ß (Ser33, Ser37). These modification events are followed by recognition of modified ß-catenin by ß-TrCP, which is a component of the E3 ubiquitin ligase complex. ß-TrCP initiates subsequent ubiquitination of ß-catenin and therefore targets the protein for rapid degradation by the proteasome.(43, 45, 49, 54-56) However, the detailed molecular mechanisms of ß-catenin trapping and degradation remain elusive.

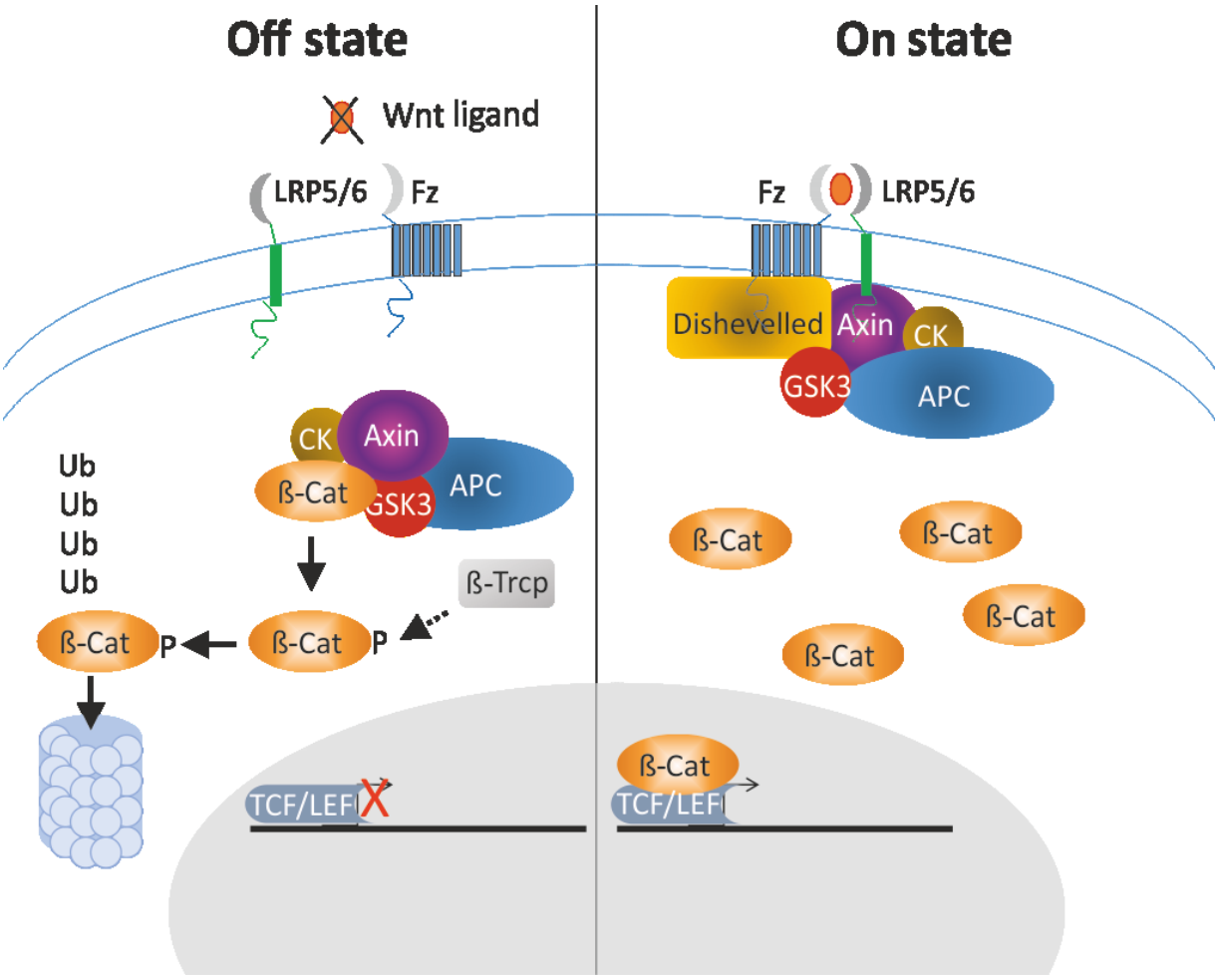

Figure 3: Wnt signaling `on state` and `off state`

Functional details of the ß-catenin destruction complex

The tumor suppressor protein Axin-1 is the key rate-limiting component of the ß-catenin destruction complex. Three key regions of Axin-1 are essential for the correct assembly of the destruction complex, namely the: N-terminal regulator of G-protein signaling domain (Axin-1^{RGS}, Axin-1^{88-211}), C-terminal Dishvelled/Axin domain (Axin-1^{DIX}, Axin-$1^{780-862}$) and the intrinsically disordered region between Axin-1^{RGS} and Axin-1^{DIX} domain (Axin-1^{IDR}, Axin-$1^{211-779}$).(57-59) (Fig. 4 A)

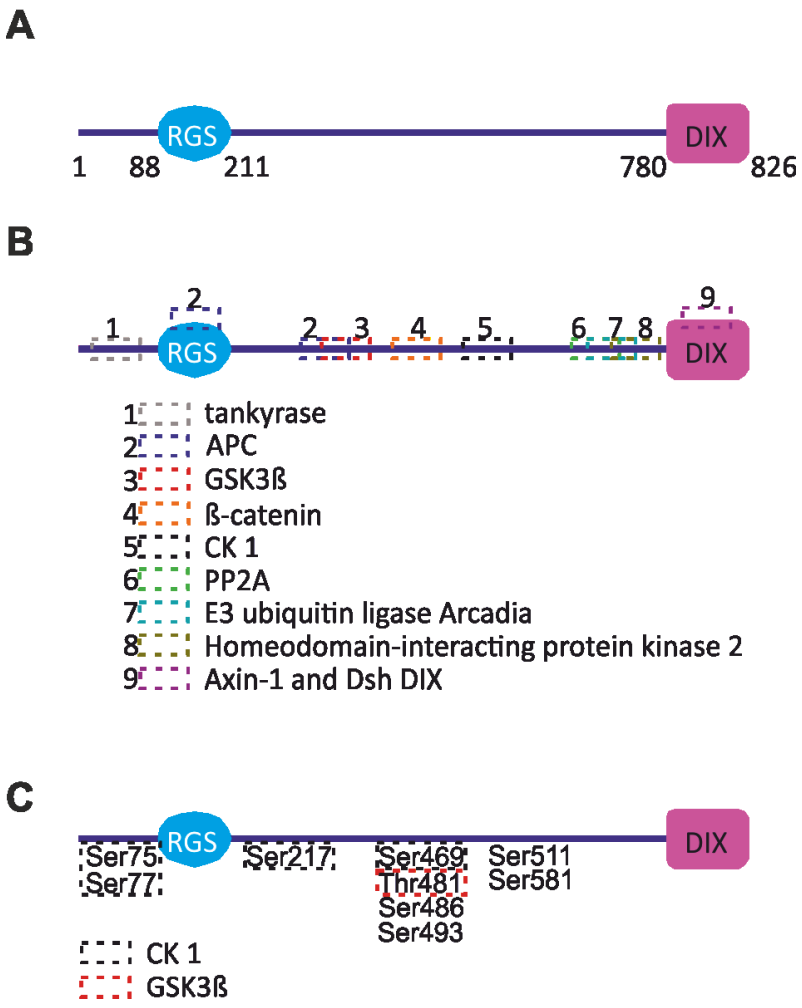

Figure 4: Organization of Axin-1. A. Domains in Axin-1. B. Mapped interaction sites in Axin-1. C. Post-translational modification sites in Axin-1.

Key protein-protein interactions are mediated by the different modules and build up an intricate interaction network in the destruction complex which is not completely understood so far. Several protein-protein interactions have been reported and include binding of i) the APC disordered region to the α-helical Axin-1^{RGS} domain (60, 61), ii) the APC armadillo repeat region to the Axin-1 disordered region (62), iii) ß-catenin to the Axin-1 disordered region (61, 63) and iv) the Axin-1^{DIX}/Dsh^{DIX} for homo- and hetero-oligomerization of Axin-1.(35, 60) On top of that, the Axin-1 disordered regions harbor binding sites for several post-translationally modifying enzymes including kinases (GSK3ß, CK1) (31, 64, 65), tankyrase (32, 66), ß-TrCP (67), E3 ubiquitin-protein ligase Arkadia BS (68), protein phosphatase 2A (65) and recently identified key proteins of other signaling pathways (e.g. Yes-Associated Protein/Transcriptional co-activator with PDZ-binding motif (YAP/TAZ)) (69, 70). The Axin-1^{DIX} is essential for homo-oligomerization of Axin-1 (35) and hetero-oligomerization of Axin-1/Dsh (60), which is an inevitable mechanism for ß-catenin destruction. (Fig. 4 B) The study of Schwarz-Romond et al. indicated that the Axin-1^{DIX} is an essential feature for efficient **puncta** formation.(71) However, Axin-1$^{\Delta DIX}$ constructs or constructs harboring a polymerization-deficient mutant variant of the Axin-1^{DIX} still formed a few cytoplasmic multiprotein assemblies.(35, 71) Therefore, also other interactions in the protein might be involved in phase separation. Noteworthy is also that cancer mutations in the RGS domain also disrupt *puncta* formation.(72) It has been shown that Arg765 and Val810 are important residues for Axin-1 recruitment to the plasma membrane in Wnt signaling.(73)

A few studies focused on Axin-1 regulation. Xie He suggested an active conformation of Axin-1 in case of GSK3ß phosphorylation, whereas the protein was inactive in a dephosphorylated state.(63) FRET measurements showed a localization of the C-terminal Axin-1^{DIX} close to the N-terminal Axin-1^{RGS} domain in absence of Axin-1 phosphorylation. In their studies they revealed an interaction of the ß-catenin-binding domain of Axin-1 with the Axin-1^{DIX} domain, but not the homologous Dsh^{DIX} domain. In addition, it has already been reported that this interaction is abolished in absence of the histidine-rich region (Hrr) around residue 540. They suggested that formation of the Wnt-induced LRP6-Axin signaling complex promoted Axin-1 dephosphorylation and

leads to a closed conformation of Axin-1 through an intramolecular interaction. Inactivation of Axin-1 diminished its association with β-catenin and LRP6, thereby inhibiting β-catenin phosphorylation. High concentrations of ß-catenin can compete against this auto-inhibition event in Axin-1 and can, despite back fold of the Axin-1^{DIX} domain, lead to ß-catenin degradation to avoid an excessive accumulation.(63) Wang et al.(73) used an activator of Wnt signaling, HLY78, which targets the Axin-1^{DIX} domain and thereby promotes an open conformation and Axin1/LRP6 association and finally Wnt activation. Hereby they argued that HLY78 reduces auto-inhibition of Axin-1 by targeting the crucial residues Arg765 and Val810.(73) In contrast, Luo et al. proposed that disordered regions close to the oligomerizing Axin-1^{DIX} domain, far from the motif identified by Kim et al., interact with the Axin-1^{DIX} domain and prevent homo-oligomerization. According to their model, Axin-1 exists in an equilibrium of homooligomer and monomer with an intramolecular loop.(59) These results suggest that there are a lot of discrepancies in literature which cannot be solved using only cell biology studies. For example, Xie He revealed Axin-1^{DIX} binding in a region around residue 460, whereas Luo et al. detected a binding event of the Axin-1^{DIX} domain to the C-terminal region of the intrinsically disordered region in Axin-1. Based on these findings, I propose a model for Axin-1 regulation in which a combination of multiple long-range intra-molecular interactions in Axin-1 regulate its activity. In addition, current knowledge assumes that Axin-1 *puncta* formation depends highly on Axin-1^{DIX}/Axin-1^{DIX} homo-oligomerization, however, oligomerization-deficient mutant variants of the Axin-1^{DIX} are still capable of phase-separation in the cytoplasm.(71) These findings, and the fact that LLPS requires multivalent interactions, lead to the hypothesis, that not only Axin-1^{DIX} oligomerization, but also Axin-1 intra-molecular interactions are crucial for phase separation.

Axin-1 regulation by post-translational phosphorylation

Multiple post-translational modification sites have been identified in Axin-1, and for some of them, functional data are available. These modifications comprise ADP-ribosylation, ubiquitination but also phosphorylation.(74) Axin-1 is ADP-ribosylated by tankyrases. This modification leads to ubiquitination, subsequent proteasomal degradation and therefore translates into low Axin-1 levels.(74) Stability of Axin-1 is retained by C-terminal SUMOylation target sites and also by interaction with ubiquitin-carboxyl-terminal hydrolase 34 (USP34).(75, 76) ADP-ribosylation is mainly involved in down-regulation of cellular Axin-1 levels. Another post-translational modification, Axin-1 phosphorylation, has a more diverse regulatory role affecting interactions and conformations of Axin-1. It is already known that Axin-1 is phosphorylated by CK1 (Ser75, Ser77, Ser217, Ser469) (64), by GSK3ß (Thr481) (65) and also by so far unknown kinases (Ser486, Ser493, Ser511, Ser581) at different putative phosphorylation sites throughout the sequence. (Fig. 4 C) Phosphorylation of Axin-1 by CK1 leads to enhanced binding of GSK3ß and therefore to conformational changes which consequently modulate its affinity for ß-catenin, LRP5/6 and other components of the Wnt signaling pathway.(64) Phosphorylated Axin-1 has been proposed to adopt an active conformation which is accessible for ß-catenin binding whereas dephosphorylation of Axin-1 leads to an auto-inhibitory ‘closed’ conformation, which is then recruited to the plasma membrane via LRP5/6 binding.(63, 73) These phosphorylation events are important for ß-catenin and LRP5/6 binding and therefore for the localization of Axin-1 and finally determine (dis-)assembly and function of ß-catenin destruction complex.(64, 77) (Fig. 5)

The model of Xie He (63) has been proposed by extensive cell-biological assays, where deletion constructs of Axin-1^{IDR} harboring the ß-catenin binding domain (BCD) were able to pull-down Axin-1^{DIX} in the phosphorylated state, whereas a lack of phosphorylation or the H-rich region, did not reveal a pull-down of Axin-1^{DIX}. Therefore it was hypothesized, that phosphorylation and the H-rich region are essential factors for Axin-1^{DIX} binding events to Axin-1^{IDR}, and that a ß-catenin displacement is mediated via Axin-1^{DIX} interaction. However, this study did not map exact binding events, neither on Axin-1^{IDR} nor on Axin-1^{DIX}, and therefore an extensive study of those binding events is needed in order to understand Axin-1 auto-regulation.

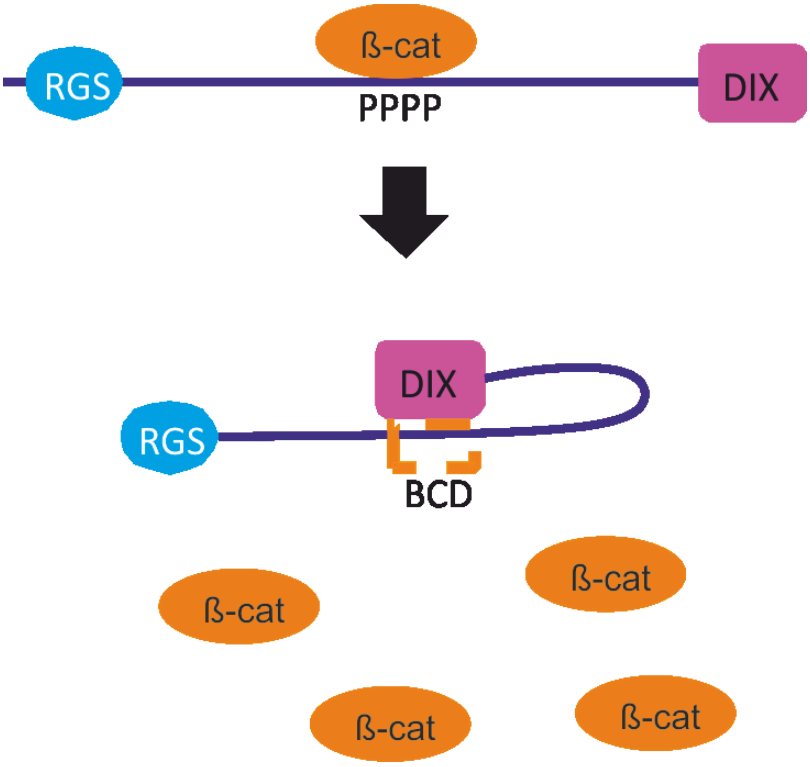

Figure 5: Model for Axin-1 auto-inhibition (63)

Phosphorylated Axin-1 is in an open conformation, therefore accessible for ß-catenin binding. Bound ß-catenin will be phosphorylated and subsequently proteasomal degraded. In absence of post-translational phosphorylation, a back-folding event of Axin-1^{DIX} to Axin-1^{IDR} leads to the closed conformation of the protein, thereby displacing ß-catenin from Axin-1 and resulting in high cytoplasmic/nuclear levels of ß-catenin.

Wnt signaling and diseases

Since the Wnt pathway is inevitable for a great variety of different physiological functions, it is obvious that deregulation of Wnt signaling results in diseases including different types of cancers such as breast and colon cancer.(78-80) Axin-1 variants have been identified to play a role in the development of different types of cancers. Mutant or truncated variants of Axin-1 or -2 are known to lead to stabilization of ß-catenin due to insufficient ß-catenin phosphorylation in the destruction complex.(77) They are associated with a variety of cancer types including medulloblastoma, ovarian endometrial adenocarcinoma, oesophageal squamous cell carcinoma, colorectal cancer and hepatocellular carcinomas.(78-81) Mutations leading to cancers are found in the structured Axin-1^{RGS} and the structured Axin-1^{DIX} domain, but also in the disordered region (e.g. ß-catenin and GSK3ß binding domains). Tumor formation is induced by inhibition or down-regulation of Axin-1 which acts as a tumor suppressor. A downregulation of Axin-1 can, for instance, be mediated by tankyrase, which poly ADPribosylates and thereby destabilizes Axin-1. Tankyrase builds a promising target for Axin-1 dependent cancer therapies using tankyrase inhibitors.(32, 66) Although many studies already investigated Axin-1 and its importance for development of cancer, none of those studies focused on the impact of phase separation and disruption of phase separation in cancer.

Central aim

The central aim of this chapter is to contribute to the current understanding of Axin-1 auto-regulation, the formation of macromolecular assemblies within the cytoplasm and the effect of cancer mutations on those processes. Hereby I used a combination of structural biology and cell biology techniques in order to decipher intra-molecular interaction within the protein Axin-1. State-of-the-art NMR spectroscopy experiments were used in order to verify interactions, as well as to map the exact intra-molecular binding sites (BS) with amino acid resolution. In addition, those experiments were complemented with fluorescence anisotropy experiments, which help to detect small changes in affinities. On a research stay at the University Medical Center Utrecht (UMC Utrecht, the Netherlands) I made use of commonly used ß-catenin dependent luciferase assays and fluorescence microscopy in cells, in order to obtain physiological data supporting the NMR-based data.

Introduction Part II

NMR-based metabolomics

The second chapter of my PhD thesis focuses on the more applied part of my work, which accompanied me during the last four years of my research career: NMR-based metabolomics. In our group of integrated structural biology and metabolism research, I was largely involved in a variety of projects in collaboration with cell biology groups, research groups working with animal models, but also clinicians working with patient's samples. In those projects, we made use of our NMR knowledge and were able to answer specific metabolic research questions using our state-of-the-art NMR-based metabolomics setup, which resulted in a variety of publications.(82-87)

Metabolic profiling is the measurement of the response to genetic modifications as well as other environmental stimuli. Metabolomics provides complementary information to all other 'omics' disciplines including genomics, proteomics or transcriptomics.(88, 89) The measured metabolites are small molecules providing a snapshot of the metabolism in either cells, tissues or biofluids.(90-92) There are thousands of metabolites in the metabolome, which can be identified and quantified due to different chemical properties using techniques like mass spectrometry (MS) or NMR spectroscopy. During the last years, there were recent technological developments, which opened up the application of metabolomics in biological, medical and nutritional research.(93-99)
NMR and MS-based metabolomics have certain advantages/disadvantages and, in combination, they provide the outmost information content about biological samples. For instance, NMR spectroscopy suffers from a lower sensitivity compared to MS, however, it prevails with its high reproducibility and unique spectral signatures.(90, 100) Since the methodological focus of our research group lies in NMR spectroscopy, we used this analytical technique for our studies.(99)

Setup of metabolomics studies

The first and essential step is the verbalization of a specific research question, which will be answered by the metabolomics study. Based on the research question, appropriate sample material can be collected, and it determines whether the study is targeted or untargeted, and which analytical technique and data analysis tool is used.(99-101)

Different biological matrices can be used for metabolomics studies, such as cells, organoids (102), tissues but also biofluids (e.g. urine, serum, liquor). Hereby, any kind of modulation can be used, such as CRISPR/Cas9 technology (103), siRNA treatment (91) or treatment with pharmacological compounds.(92) In any case, proper control conditions have to be selected, samples have to be taken using standard operating procedures, storage conditions have to be controlled and sample size has to be sufficient in order to ensure statistical significance.(99, 104)

Sample preparation usually includes extraction steps such as cell lysis or protein removal.(91, 105) Hereby, cellular metabolites are released using bead homogenizers, material containing large amounts of proteins is extracted using methanol prior to use, in order to avoid line broadening due to protein content in the measurements and enzymatic reactions were quenched.(106) In case volatile compounds were of interest, e.g. trimethylamine (107), or samples did not contain protein, they are mixed with buffer and directly measured.(92, 93) In certain cases, analytical behavior of metabolites can be improved by removal of metabolites due to interaction with silica nanoparticles (108) or by introduction of a cholamine tag which introduces NMR active ^{15}N nuclei.(109)

Targeted metabolomics approaches are optimized for the detection of specific metabolites (92), whereas untargeted studies determine differences in the metabolic fingerprint of samples.(97, 99, 110) In general, NMR-based metabolomics is used for untargeted metabolic studies, and therefore provides a plethora of metabolite information.

NMR spectroscopy provides information about resonance frequencies of NMR active nuclei (^{1}H, ^{13}C, ^{15}N or ^{31}P), where the intensity correlates with metabolite concentrations within the samples. Therefore an internal standard with known concentration can be used for metabolite quantification. Since NMR spectroscopy is a non-destructive method, samples can be measured several times, and with appropriate storage conditions, deviations in the measurements were minimal due to the high reproducibility of the analytical technique.(99, 111)

NMR experiments make use of different pulse sequences which provide information about scalar couplings, chemical shifts, connectivity, special proximity or diffusion properties. In multidimensional NMR experiments information contents are combined, and signal overlap is reduced.(88, 99)

Data analysis in NMR-based metabolomics studies

Chemical shifts and splitting patterns in NMR spectra are used for the identification and quantification of metabolites. Most commonly used NMR experiments in metabolomics research (e.g. ^{1}H ^{1}D one-pulse sequence, nuclear Overhauser effect spectroscopy (NOESY) and CPMG (Carr-Purcell-Meiboom-Gill) pulse sequences with water suppression using presaturation) are fully quantitative and therefore enable direct determination of metabolite concentrations. For quantification, corresponding NMR signals are simply integrated and concentrations are determined using known concentrations of the internal standard.(90, 99, 112, 113)

For the untargeted analysis of samples, a variety of statistical approaches can be used for the complex data sets, such as unsupervised multivariate statistics (e.g. principle component analysis (PCA), hierarchical clustering) and supervised multivariate statistics (e.g. orthogonal partial-least squares discriminant analysis (O-PLS-DA)). The PCA approach identifies data points (e.g. NMR chemical shifts corresponding to distinct metabolites) which indicate large differences between samples. For evaluation of samples and for the determination of outliers, Hotelling's T^2 ellipse is used. O-PLS-DA approaches are used in order to determine specific metabolites signatures lead to differences between the groups, and intra-group variances are excluded (orthogonal components). Cross-validation is an important step to assess the quality of the obtained data and to avoid overfitting of the data by testing data subsets.(99)

In our group, multivariate statistical analysis is performed in order to reveal differences between the groups using MATLAB 2014b (MathWorks) and MetaboAnalyst 4.0.(114) First, unwanted signals in samples (e.g. H_2O, methanol, TSP) are cut out, then NMR spectra are aligned and finally probabilistic quotient normalization is applied in order to correct for sample dilution.(1) Statistical analyses includes PCA, O-PLS-DA and all associated data consistency checks with 7-fold cross-validation.(115) In order to validate the statistical significance of the determined differences between the groups, quality assessment statistic Q is always reported. This measure provides information about cross-validation and is a qualitative measure of consistency between the predicted and original data, with a maximum value of 1. (Fig. 6)(99)

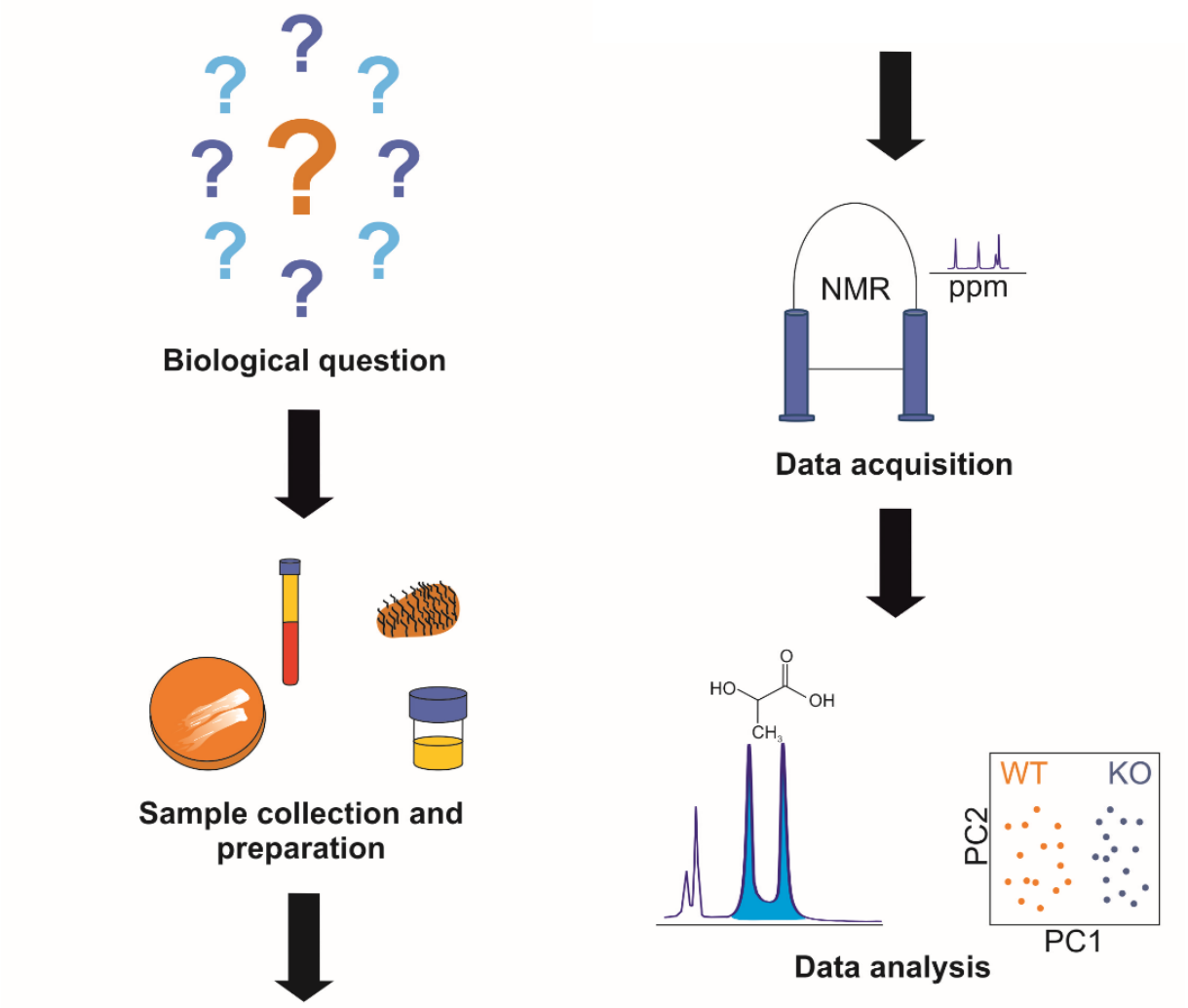

Figure 6: Metabolomics workflow

Apart from the projects, where we act as co-authors and used our techniques to generate data for collaboration groups, some of the projects also originated in the MadI lab, which resulted in a first author review in *Microbial Cell* about metabolomics and its emerging role in autophagy research(99), but also in an original research publication in *Scientific reports*, where we developed a NMR-based method for carbohydrate detection and quantification.(6)

Liver cirrhosis

For several liver diseases cirrhosis is the common end stage, which makes it a global health burden with continuously rising incidence. Liver cirrhosis has already been associated with gut microbiome alterations.(116) In general, microbiome translocation in the circulation is prohibited by tight junction proteins between gastric and intestinal cells, which are regulated by e.g. myosin light chain kinase. However, besides altered liver histology and hepatic venous pressure, increased upper digestive tract and intestinal permeability are clinical signs for advanced liver cirrhosis.(117, 118) In case of increased gastric or intestinal permeability, translocation of bacterial products (e.g. endotoxins) occurs, which results in inflammation.(119, 120) This makes the analysis of increased permeability essential for diagnosis and steering treatment for patients.(6, 121)

Triple-sugar test for liver cirrhosis patients

Analysis of intestinal and gastric permeability is usually mediated via oral administration of carbohydrates, which are not metabolized and chemically inert. After administration, the distribution and the final renal excretion of the compounds is monitored. The current gold standard for the determination of increased permeability is a combination of lactulose, sucrose and mannitol.(83, 122, 123) Those carbohydrates use different cellular pathways, and therefore they enable the determination of deficiencies of mucosal barriers and absorbance efficiencies.(6)

Lactulose and sucrose are two types of carbohydrates using a paracellular route through tight junction proteins between the enterocytes. Therefore, renal excretion of these carbohydrates will be a measure for increased permeability. More precisely, the disaccharide sucrose is typically cleaved into glucose and fructose in the jejunum. Therefore, high abundance of intact sucrose molecules in urine indicate an increased gastric permeability.(124) In contrast, lactulose molecules are an indicator for increased intestinal permeability, due to increased paracellular transport in the systemic circulation and finally urinary excretion.(121, 122) The third carbohydrate, mannitol, is

transcellularly transported, therefore it acts as a reference compound since it is always subject to renal excretion. However, mannitol can be a measure for reduced mucosal absorbance due to villus shortening.(6, 121, 125)

Detection of carbohydrates in urine

The readout of the triple-sugar test is information about the concentration of excreted compounds in urine which indicates either increased upper digestive tract or intestinal permeability. There are different approaches available, which are currently applied for the quantification of carbohydrates. On the one hand, enzymatic assays are used, which can be problematic due to interfering substances such as galactose.(121, 126) On the other hand, chromatographic methods including HPLC/MS require sample preparation steps in order to remove e.g. sodium ions, which can lead to signal suppression in tandem MS detectors.(125) This implicates that there is an urgent need for an accurate, fast and reliable tool for the triple-sugar test. First studies using NMR spectroscopy for carbohydrate quantification in urine have already been made by Jayalakshmi et al.(127) and Kumar et al.(128). One of the potential drawbacks of NMR spectroscopy is the low sensitivity compared to other techniques such as MS. However, this limitation is only relevant for the detection of low concentrated compounds. Carbohydrate concentrations in urine are at least in the micromolar range, therefore, they can be easily detected by standard NMR experiments with a measurement time of 30-60 minutes per sample. Pathologically increased intestinal permeability indices (lactulose/mannitol ratio >0.07) presume high concentrations of carbohydrates (about 100 µM), which require only short NMR measurement times of less than 10 minutes.(6)

Central aim

These standard 1D ^{1}H NMR experiments allowed the quantification of carbohydrates in the complex matrix without any sample preparation steps, there was a severe overlap of metabolite signals in the sugar region.(127, 128) Therefore, we extended this setup by using ^{1}H homo-nuclear J-resolved 2D correlation experiments (JRES). Hereby, the severe signal overlap of 1D experiments is reduced by introducing a second dimension, which separates the chemical shift from the scalar J-coupling. One-dimensional projections of the two-dimensional spectra result in decoupled spectra, where multiplets are reduced to single peaks and the severe signal overlap is reduced.(121) Apart from the advantages which JRES spectra provide for spectral analysis, there are also a few drawbacks which have to be considered. Those features, such as longer acquisition times, higher technical variability and phase-twisted line shapes leading to quantification errors, require prudent usage of the experiments. By taking into account those advantages and disadvantages of JRES experiments, we were able to use this NMR-based tool for carbohydrate quantification in urine.

The main aim of the study was to provide a fast, robust and reliable tool, in order to determine increased permeability in the digestive tract by detecting and quantifying carbohydrates in urine simultaneously. Apart from obtaining quantitative information about carbohydrates after renal excretion, those experiments provide untargeted urinary metabolite profiles without any additional measurement time.(6)

Material and Methods Part I

Since the key protein in this project, Axin-1, is a protein harbouring extensive intrinsically disordered regions, conventional structural biology methods are not applicable. These regions do not occupy rigid structures, which makes the use of X-ray crystallography to study intra-molecular interactions impossible. Therefore, a combination of several complementary techniques in molecular biology, biochemistry and structural biology methods was used to get insight into interactions and mechanisms in the ß-catenin destruction complex *in vitro*. Apart from that, cell biology techniques were used in order to study the protein in a more physiological environment.

Plasmids

Human Axin-1 isoform b was used for structural biology experiments and cell biology experiments. DNA constructs for structural studies were obtained from Genescript®. Genes of interest were cloned in a modified pETM11 vector containing a T7 promotor, a N-terminal polyhistidine tag, a protein A tag as well as a Tobacco Etch Virus (TEV) cleavage site for purification (Z-Tag).

For cell biology experiments, human Axin-1 isoform b with C-terminal V5-tag was subcloned into pcDNA4T/O by standard PCR methods. GFP-tagged human Axin-1b was subcloned into pcDNA3.1(+).

Point mutations were generated by site-directed mutagenesis using Q5 High-Fidelity Polymerase (New England Biolabs).

For the 50µl PCR the reagents were mixed as follows:

10 µl Q5 High Fidelity DNA Polymerase Buffer (5x)
1 µl dNTPs (10 mM)
2.5 µl Forward Primer (10 µM)
2.5 µl Reverse Primer (10 µM)
0.25 µl Q5 High Fidelity DNA Polymerase (2 U/µl)
1 µl DNA Template (20 ng/µl)
32.75 µl Nuclease-free water

Cycling conditions:

Step 1: Initial Denaturation (98°C) 2 minutes
Step 2: Denaturation (98°C) 30 seconds
Step 3: Annealing (primer-dependent) 30 seconds
Step 4: Extension (72°C) 4.5 minutes
Go to Step 2 and repeat 25 times
Step 5: Final Extension (72°C)
Step 6: 2 minutes Hold (10°C)
Step 7: ∞

1 µl of DpnI enzyme was added into the PCR tube and mixed by pipetting. After incubation at 37°C for one hour, 2 µl of the PCR reaction were mixed with 15 µl of Nuclease-free water and heated for 20 minutes at 80°C. 2 µl of 10X T4 Ligase buffer (NEB) and 1 µl of T4 polynucleotide Kinase (PNK-NEB) were added to the chilled tube and incubated for 30 minutes at 37°C. After a ligation step of 2 hours at room temperature using 1 µl of T4 Ligase (NEB), the plasmids were transformed into competent high copy *E.coli* cells (Top10) and constructs were sent for sequencing to GATC biotech.

Primers

Primers for the generation of Axin-1 constructs by site-directed mutagenesis were as follows:

Table 1: Primers for mutagenesis

Construct	Primer
E816G fw	AGACGAAGCGGTGCTGCCGGTGTTTGAAGGCAAGATTATCGG TAAAGTGGAGAAG
E816G rv	TCTGCTTCGCCACGACGGCCACAAACTTCCGTTCTAATAGCCA TTTCACCTCTTC
495-595 fw	GGGCACGTGGCCAAGATG
495-595 rv	AGATCCTTGAAAATAAAGATTTTCGTGGTG
ΔBS1 fw	GCCGGGTCCGTGCCACAAATGCGCGGGCCTGCGTGAT
ΔBS1 rv	CGGCCCAGGCACGGTGTTTACGCGCCCGGACGCACTA
ΔBS2 fw	GAGGCGACCCGTCGTGCGGGTGCGCGTAGCCGTGGC
ΔBS2 rv	CTCCGCTGGGCAGCACGCCCACGCGCATCGGCACCG
ΔBS3 fw	GCGAGCGAGGATGCGGAAAAGGAAATTAGCCGTCATCGTCG
ΔBS3 rv	CGCTCGCTCCTACGCCTTTTCCTTTAATCGGCAGTAGCAGC
ΔAxin-1^{DIX} fw	CGCGCAACCGTAGGACAGCATCG
ΔAxin-1^{DIX} rv	CTACCGCCACCAACCTTAC

Protein production

50 ng of plasmid DNA was added to competent *E.coli* BL21 DE3. After an incubation step of 10 min on ice, a heat shock of 42°C for 45 s was applied in an Eppendorf thermoblock. For regeneration, cells were incubated for one hour in 1 ml of LB media without an antibiotic selection at 37°C shaking in an Eppendorf thermoblock. After incubation, cells were plated on LB-agar plates containing kanamycin for selection. Competent *E.coli* colonies were picked and grown in 10 ml of LB media + kanamycin for selection at 37°C in an incubator overnight. The overnight culture of *E.coli* BL21 DE3 with the genetic information of the protein of interest on a plasmid containing a selection marker was used to inoculate a main culture (1 L LB media or minimal medium (^{13}C glucose and/or ^{15}N ammonium chloride supplemented) + Kanamycin for selection). When grown to an optical density at 600 nm (OD_{600}) of approximately 0.8 at 37°C, the protein expression was induced with 1 mM isopropyl-β-D-thiogalactopyranosid (IPTG) at 20°C overnight. After expression of proteins, cells were harvested by centrifugation (15 min, 6000 rpm, 4°C).

Protein purification

Information for all buffers used for protein purification/experiments are listed in the appendix.

E.coli cells were lysed to isolate the recombinant expressed proteins. The pelleted cells were thawed on ice and re-suspended in 20 ml of Lysis buffer. Cells were sonicated for 24 minutes (1 s on/1 s off; 70 % intensity) on ice and centrifuged for 30-45 minutes at 4 °C (12 000 rpm). The supernatant contains all the soluble cellular protein. In the first step proteins were purified Ni-NTA (Ni-NTA Agarose as stationary phase, Thermo Fisher) gravity columns. The purification is based on binding of His-tagged proteins to Ni^{2+} residues in the column. The column was equilibrated with 25 mL of Buffer A and the supernatant of lysed *E.coli* cells was applied on the column. The flow through was collected and applied a second time to attain a higher yield. Non-specific bound proteins were removed by washing the column with approximately 40 ml of Buffer A

and non-specific bound DNA was removed by washing the column with 25 mL of Buffer A'. The elution of non-specific proteins was monitored using NanoDrop^{TM} (Peqlab). The protein of interest was eluted with 10-15 ml of Elution buffer. To avoid a non-native conformation of the protein, the Z-tag was removed using TEV protease. The concentration of the eluted protein was determined using NanoDropTM (Peqlab) and 2 (w/w) % of TEV protease was added to the protein solution. The sample was incubated for at least 4 hours at 4 °C for cleavage. HiPrep 26/10 Desalting (50 ml, GE Healthcare) on an Äkta pure FPLC system (GE Healthcare) was used for buffer exchange. Column was equilibrated with 60 ml of buffer A at a flow rate of 5 ml/min. The protein elution was applied on the column and eluted fractions were collected depending on the UV absorbance at 280 nm measured by Äkta system detector. In order to avoid Z-tag or TEV protease contamination, the protein was applied on a HisTrap (5 mL, GE Healthcare) on an Äkta pure FPLC system and the flow through containing the cleaved protein was collected.

Due to the Hrr in the protein around residue 540, constructs harbouring this region of the protein were not subject to a HisTrap purification step after TEV cleavage. Full-length Axin-1 was purified from TEV protease and Z-tag using a size exclusion chromatography (SEC) step (Superdex 200 pg 300/10 Increase). Axin-1$^{495-595}$ was purified from Z-Tag and TEV protease using a HiTrap Heparin HP (5ml) column with Buffer A and an increasing gradient of buffer A' (100 % buffer A' in 15 ml).
For all experiments, proteins were subject to SEC. Larger constructs were purified using Superdex 200 pg 300/10 Increase, smaller constructs were purified using Superdex Peptide 300/10 in final buffer.
To obtain higher protein concentrations, Amicon Ultra Centrifugal Filters (Millipore) with a cut off of 10 kDa or 3 kDa were used. Centrifugation steps of 5 – 10 min at 4 °C at 3500 rpm were followed by mixing of the protein solution in the filter to avoid precipitation of the protein due to the concentration gradient.

NMR assignment experiments

Three dimensional assignment experiments of Axin-1$^{495-595}$ and Axin-1$^{351-500}$ were recorded on a 700 MHz Bruker Avance III NMR spectrometer equipped with a TCI cryoprobe or on a 600 MHz Bruker Avance Neo NMR spectrometer equipped with a TXI 600S3 probehead at 298 K. HNCACB spectra (hncacbgp3d) were recorded with spectral widths 13.6543/24.00/62.00 ppm, centered at 4.7/118/39 ppm in ^{1}H/^{15}N/^{13}C, with 1024, 64, 200 points, respectively. HN(CO)CACB spectra (hncocacbgp3d) were recorded with spectral widths 16.02/24.00/62.00 ppm, centered at 4.7/118/39 ppm in ^{1}H/^{15}N/^{13}C, with 1024, 64, 200 points, respectively. HNCANNH type experiments for intrinsically disordered proteins (hncannhgp3d, hncannhgp3d.2) were recorded with spectral widths 13.66/24.00/24.00 ppm or 13.66/24.00/4.00 ppm, centered at 4.7/118/118 ppm or 4.7/117/4.7 ppm in ^{1}H/^{15}N/^{13}C, with 1024, 64, 200 points or 1024, 64, 100 points, respectively.

Assignments of Axin-1^{DIXM2} were transferred from published assignments.(129)

Three-dimensional assignment experiments were processed using NMRpipe (IBBR) (130) and the assignment was performed in CcpNmr Assigment software (3.0.b1)(131).

NMR relaxation experiments

^{1}H^{15}N HetNOE experiments were measured for Axin-1$^{351-500}$ and Axin-1$^{580-650}$ at a concentration of 100 µM. on a 600 MHz Bruker Avance Neo NMR spectrometer equipped with a TXI 600S3 probehead at 298 K. Experiments were recorded with spectral widths 16.0176/19.0033 ppm, centered at 4.7/118.5 ppm, with 2048, 512 points. Experiments were processed using TopSpin software (Bruker, 4.0).

Secondary chemical shifts

Chemical shifts of the protein backbone are sensitive to geometry and can therefore provide information about secondary structures. Therefore secondary chemical shifts were calculated for disordered proteins in order to obtain information about transient structures using following formula:

$$\Delta\delta = \delta_{\text{observed}} - \delta_{\text{random coil}}$$

Random coil chemical shifts were predicted using ncIDP library, which is optimized for intrinsically disordered proteins harbouring many proline residues.(132)

NMR interaction studies

For NMR spectroscopic studies ^{13}C and/or ^{15}N isotopically labelled recombinant proteins were produced in *E.coli*. Samples for NMR measurements contained 90 µM ^{15}N labelled Axin-1 constructs in in NMR buffer with 10% $^{2}H2O$ added for the lock signal. ^{1}H-^{15}N HSQC NMR spectra were recorded at 298 K on a 600 MHz Bruker Avance Neo NMR spectrometer equipped with a TXI 600S3 probehead or on a 700 MHz Bruker Avance III NMR spectrometer equipped with a TCI cryoprobe. NMR spectra with ß-catenin were prepared in ß-catenin buffer. All spectra were recorded with a recycle delay of 1.0 s, spectral widths of 15.9/30 ppm, centered at 4.7/118.0 ppm in $^{1}H/^{15}N$, with 1,024 and 256 points, respectively, and 16 scans per increment. Experiments were processed using TopSpin software (Bruker, 4.0).

Chemical shift perturbations

Normalized chemical shift perturbation for each residue was calculated using following formula:

$$\Delta\delta(\mathrm{ppm}) = \sqrt{(\Delta\delta_{\mathrm{H}})^2 + \left(\frac{\Delta\delta_{\mathrm{N}}}{10}\right)^2}$$

NMR phosphorylation assays

Samples for NMR phosphorylation assays contained 20 µM ^{15}N labelled Axin-1 constructs in NMR buffer with 300 mM NaCl, 10 mM $MgCl_2$, 0.1 mM EDTA, 5 mM ATP, PhosSTOP™ (1x, Roche) were mixed with GSK3ß (10 µM) and 10% $^{2}H2O$ added for the lock signal. ^{1}H-^{15}N HSQC NMR spectra were recorded at 298 K on a 600 MHz Bruker Avance Neo NMR spectrometer equipped with a TXI 600S3 probehead. All spectra were recorded with a recycle delay of 1.0 s, spectral widths of 15.9/30 ppm, centered at 4.7/118.0 ppm in ^{1}H/^{15}N, with 1,024 and 256 points, respectively, and 16 scans per increment. Experiments were processed using TopSpin software (Bruker, 4.0).

Fluorescence anisotropy

For fluorescence anisotropy affinity measurements unlabelled recombinant Axin-1^{DIX} or ß-catenin (full-length or ß-catenin$^{141-304}$) was produced in *E.coli*. Affinity measurements were performed using FITC-tagged synthetic peptides harbouring the sequence of the BSs (LPPAPAWHHFPPRCVDMG, QSSFAWGLEPHSH, KNQKIMQWIIEGE, LRDAHEENPESILDEHVQRVLRT(PO$_4$)PGRQS(PO$_4$)PGPGHRS(PO$_4$)PDS(PO$_4$)).
Samples for anisotropy measurements contained 1000 to 3.9 µM Axin-1^{DIX} domain (M2 or M2 E816G) in NMR buffer, or 100 to 0.39 µM ß-catenin full-length, or 100 to 0.39 µM or 750 – 1.9 µM ß-catenin$^{141-304}$ in ß-catenin buffer. Measurements were performed

on a ZENYTH 3100 (Serial Number: 1085) in Greiner polypropylene microplates with 384 square flat-bottomed wells in a volume of 30 µL with Anthos ADAP Software.

Turbidity experiments

Axin-1 was prepared in NMR buffer at a concentration of 100 µM. The protein was diluted and turbidity measurements were conducted at 620 nm in 96-well plates with 80 µl sample volume using a BioTek Power Wave HT plate reader.

Electron microscopy

Carbon coated copper grids (carbon film coated 400 mesh copper grids, Science Services) were glow discharged for 25 s in a Harrick plasma cleaner (PDC-32G-2) to facilitate protein adsorption. Protein samples were prepared in NMR buffer and deposited on the grid surface. The grid was blotted shortly using Whatman paper. After blotting, the grid was air dried for at least 20 min. Images were obtained using a JEOL JEM 1400-plus electron microscope at 120 kV (TEM Center software, JEOL). The ImageJ (NIH) Software packages was applied for image analysis.

Differential interference contrast microscopy

For DIC, 25 µL of recombinant protein (80 µM) in NMR buffer was plated on 30 mm, No. 1, round glass cover slips and mounted on an Observer D1 microscope with 100x/1.45 oil immersion objective (Zeiss, Germany). Protein assemblies were monitored using HAL 100 halogen lamp and images were captured with an OrcaD2 camera (Hamamatsu, Japan) using VisiView 4.0.0.13 software (Visitron Systems GmbH, Germany).

Isothermal Titration Calorimetry

For ITC experiments, Axin-1 and GSK3ß were prepared in NMR buffer with 300 mM NaCl and 7 mM $MgCl_2$. Binding affinities of Axin-$1^{351-500}$ recombinant protein and Axin-$1^{383-400}$ and Axin-$1^{399-416}$ FITC-labelled synthetic peptides to GSK3ß were determined by ITC on a VP-ITC Microcal calorimeter (Microcal, Northhampton, USA) at 25 °C with 2 µl injections. All proteins/peptides were buffer exchanged before ITC. The GSK3ß concentration in the cell was 10 µM for all measurements. Axin-1 concentration in the syringe was 290 µM. The ITC data were analysed with the programme MicroCal Origin software version 7.0 and single site-binding model.

Small-angle X-ray scattering

SAXS data were recorded with an in-house SAXS instrument (SAXSspace, Anton Paar, Graz, Austria) equipped with a Kratky camera, a sealed X-ray tube source and a Mythen2 R 1 K Detector (Dectris). Thereby Axin-1/GSK3ß complex and the buffer for background subtraction where loaded via an ASX autosampler and measured in a flow cell. The scattering patterns were measured with a 180-min exposure time (180 frames, each 1 min). Radiation damage was excluded on the basis of a comparison of individual frames of the 180-min exposures, wherein no changes were detected. Obtained SAXS data were processed using the SAXSanalysis package (Anton Paar, version 3.0) and analyzed using the ATSAS package (version 2.8.2, Hamburg, Germany). The data were desmeared using GIFT (PCG-Software). The forward scattering (I(0)), the radius of gyration (Rg), the maximum dimension (Dmax), and the interatomic distance distribution function (P(r)) were computed with GNOM. To calculate surface models based on the P(r) functions DAMMIF was employed, which uses GNOM files as input (61). For each structure, 50 simulated annealing runs were and the resulting models were superimposed, averaged and filtered using DAMAVER. Matching models were then clustered by DAMCLUST.

Evolutionary coupling analysis

BIS2Analyszer (www.lcqb.upmc.fr/BIS2Analyzer/) was used for evolutionary coupling analysis.(133) Multiple sequence alignment was performed using Clustal Omega.(134) Due to sequence length limitations, only Axin-1$^{421-826}$ was used for analysis.

Sequence conservation analysis

ConSurf (www.consurf.tau.ac.il/2016) was used for sequence conservation analysis.(135) HMMER algorithm was used for homology search (E-value cutoff 0.0001) in Uniref database. 150 sequences were compared with Bayesian best model (default).

Cell culture

Human Embryonic Kidney 293T (HEK293T) cells were cultured in RPMI Glutamax (Invitrogen) supplemented with 10 % fetal bovine serum (Sigma), 100 units/mL penicillin and 100 units/mL streptomycin (Invitrogen). Cells were cultured in 5% CO_2 at 37°C. Henrietta Lacks (HeLa) cells were cultured in DMEM high glucose (Invitrogen) supplemented with 10 % fetal bovine serum (Sigma), 100 units/mL penicillin and 100 units/mL streptomycin (Invitrogen). Cells were cultured in 5% CO_2 at 37°C.

ß-catenin dependent luciferase assays

For luciferase TOPflash reporter assays HEK293T cells were cultured in 24-well plates and transfected the following day using FuGene 6 (Promega) according to manufacturer's protocol. Cells were transfected with a total amount of 250 ng plasmid per well consisting of: construct of interest, 30 ng TOPFlash or FOPFlash reporter construct, 5 ng of TK-Renilla and supplemented with empty vector. Transfection efficiency in luciferase reporter assays was controlled and normalized by including a constant amount of TK-Renilla reporter plasmid in all transfections. Cells were lysed using 1x passive lysis buffer (Promega) for 20 minutes at room temperature. A volume of 20 µL cell lysate was transferred to a white reading plate and subsequently Firefly Luciferase and Renilla values were measured on a Berthold luminometer Centro LB 960 using the Dual Luciferase reporter kit (Promega) diluted 1:3 in MilliQ water. Luciferase gene is under control of a TCF/LEF promotor, which, in the Wnt 'on state', is transcribed more frequently.

Western blotting

Proteins were detected by running cell lysates on SDS Page gels with 10 % acrylamide. Proteins were subsequently transferred to PVDF membranes (Immobilon-FL, Millipore). Membranes were blocked using Odyssey Blocking buffer (Li-Cor) diluted in PBS (1:1), incubated with primary antibody for 1 hour at RT and secondary antibody for 1 hour at RT in the dark. All antibodies are diluted in Tween (0.5 %). After staining and extensive washing, membranes were scanned using Typhoon biomolecular imager (Amersham). Antibodies used for immunoblotting were mouse anti-V5 (Genscript, 1:5000), goat anti-mouse Alexa 680 (Invitrogen, 1:8000).

Immunofluorescence microscopy

Cells were grown on coverslips in 24 well plates. The following day, cells were transfected with constructs of interest supplemented with empty vector until 250 ng DNA per well. Transfection was performed using FuGene 6 (Promega) according to manufacturer's protocol. After overnight transfection, cells were fixed in 4% paraformaldehyde (PFA) in 50 mM sodium phosphate buffer (pH 7.4) for 1 hour. Subsequently, PFA was quenched using 50 mM NH_4Cl for 30 minutes, followed by blocking with 2% BSA and 0.1% saponin in PBS to permeabilize the cells. Cells were stained with primary antibody for 1 hour, followed by secondary antibody for 45 minutes prior to mounting with Prolong Gold with DAPI (Invitrogen). Images were recorded on a Zeiss LSM-700 confocal microscope.

Structured Illumination Microscopy

Cells were grown on coverslips in 6 well plates. The following day, cells were transfected with constructs of interest supplemented with empty vector until 1000 ng DNA per well. Transfection was performed using PolyJet™ (SignaGen) according to manufacturer's protocol. After 48 hours, cells were fixed in 4% paraformaldehyde (PFA) in 50 mM sodium phosphate buffer (pH 7.4) for 1 hour.
Images were recorded on a on a Nikon-Structured Illumination Microscopy (N-SIM®) System with standard wide field and SIM filter sets and equipped with an Andor iXon3® EMCCD camera. 3D SIM stack was made with Bersen auto local threshold (ImageJ) with r = 2. Chimera Gauß volume filter (0.70) and surface rendering was performed.

Material and Methods Part II

Material and Methods section of this part of the dissertation has already been published elsewhere.(6) The study protocol is available and is uploaded with the dissertation.

Participants

The cohort study of liver cirrhosis patients was performed in Graz at the Medical University from December 2016 until March 2017. Inclusion criteria for patients participating in the study were (I) age of 24 years or above, (II) abstinence from alcohol 48 h prior to study visit and (III) the willingness and ability to give informed consent. Exclusion criteria for patients participating in the study were (I) Alcohol Use Disorders Identification Test 8 or above, (II) CAGE test 2 or above, (III) elevated liver function tests, (IV) pregnancy, (V) breast-feeding and (VI) any disorder or medication that does not allow concomitant consumption of alcohol. No diagnostic criteria were included, all participants (11 male, 5 female) were healthy, with an age of 26 ± 4, a body weight of 82.3 ± 15.6 kg and a BMI (kg/m^2) of 26.4 ± 5.2.(6)

All study procedures were performed after obtaining written informed consent and study was conducted according to the principles of the Declaration of Helsinki. The experimental protocol was approved by the institutional review board of the Medical University of Graz (28-255 ex 15/16) and is registered at clinicaltrials.gov (NCT02568904).(6)

Collection of sample material

In order to establish the protocol for carbohydrate quantification, urine samples of 15 healthy individuals were used. Hereby, participants were administered an aqueous solution containing different carbohydrates (20 g sucrose, 10 g lactulose and 5 g mannitol) as already used in Buhner et al.(136) The intake of the carbohydrate solution by the participants was controlled during five hours, however, the activity of participants was not recorded. After five hours, urine was collected as a full sample. Since urine is a nutrient-rich biofluid, thimerosal (1 mg/ml) was added to urine samples prior to storage at -80°C for inhibition of fungal growth.(6)

List of reagents

lactulose (Laevolac, Fresenius Kabi Austria), mannitol (Fluka), sucrose (Sigma Aldrich Austria) and thimerosal (Sigma Aldrich Austria), sodium phosphate, dibasic (Na_2HPO_4, VWR International), sodium hydroxide (VWR International), hydrochloric acid (32 % m/v, VWR International), and sodium azide (NaN_3, VWR International), 3-(trimethylsilyl) propionic acid-2,2,3,3-d4 sodium salt (TSP, Alfa Aesar, Karlsruhe, Germany), deuterium oxide (^2H_2O, Cambridge Isotope laboratories, Inc. (Tewksbury, MA)).(6)

Preparation of urine

Due to the low protein content, urine samples were not subject to an extraction step prior to NMR experiments. Therefore, deuterated NMR phosphate buffer (1.5 M Na_2HPO_4, 3.236 mM TSP, 0.04 (w/v) % NaN_3; pH adjusted to 7.4 with 8 M HCl and 5 M NaOH) was directly added to urine (10 % buffer, 90 % urine samples) for NMR measurements. This buffer on the one hand keeps the pH of different urine samples stable in order to reliably identify metabolites and on the other hand it contains an internal standard which is important for absolute quantification. Those samples were

transferred into 5 mm NMR tubes with a final volume of 600 µL. Until NMR measurements were performed, urine samples were stored at -20 °C.(6)

Nuclear Magnetic Resonance Spectroscopy

All NMR experiments were performed at 310 K on an Avance Neo Bruker Ultrashield 600 MHz spectrometer equipped with a TXI probe head with Bruker Topspin version 4.0.2.(6)

For one-dimensional experiments following pulse sequences were used: cpmgpr1d, noesygppr1d and reset_psyche_1d.

Using ^{1}H one dimensional experiments with a T_2 filter using Carr-Purcell-Meiboom-Gill sequence and f1 presaturation for water signal suppression (cpmgpr1d) all non-exchangeable protons of small molecules can be detected in a deuterated buffer solution and signal of proteins is suppressed.

Using ^{1}H one dimensional experiments with presaturation delay during relaxation and mixing time (noesygppr1d) all non-exchangeable protons can be detected in a deuterated buffer solution.

Using a pseudo 2D sequence and broadband homo-nuclear decoupling using the psyche element (reset_psyche_1d) all non-exchangeable protons can be detected in a deuterated buffer solution and complex splitting patterns will be resolved.(6)

Table 2: Pulse sequences used for one-dimensional NMR experiments (6)

	scans	**size of fid**	**spectral width (Hz)**	**d1 (s)**
cpmgpr1d	128	73728	11904.76	4
noesygppr1d	128	98304	98304	4
reset_psyche_1d	8	4096/1024 F2/F1	11904.762	16

For two-dimensional experiments following pulse sequences were used: jresgpprqf, zggpw5 and dipsi2gpphpr.

Using ^{1}H homo-nuclear J-resolved 2D correlation experiments with presaturation during the relaxation delay (jresgpprqf) all non-exchangeable protons of small molecules can be detected in a deuterated buffer solution for either Chenomx quantification (d1 = 2 s) or MestreNova quantification (d1 = 16 s).

Using homo-nuclear, phase sensitive Hartman-Hahn transfer experiments (dipsi2gpphpr) all non-exchangeable protons can be detected in a deuterated buffer solution.

Using a modified version of the zggpw5 pulse sequence preceding a saturation recovery block) before the first 90° pulse and using water suppression with the w5 sequence T1 times for the carbohydrates and TSP were determined. Delays were chosen as follows: 0.01, 0.22, 0.54, 1.05, 1.84, 3.08, 5.01 (duplicated), 8.01, 12.69, 20.00 s.(6)

Table 3: Pulse sequences used for two-dimensional NMR experiments (6)

	scans	**size of fid (F2/F1)**	**spectral width (Hz, F2/F1)**	**d1 (s)**
dipsi2gpphpr	16	8192/400	11904.76/19.8313	2
zggpw5 for T1	128	73728/11	11904.76/5882.353	0.1
jresgpprqf	4	16384/32	10000.00/16.6583	2
jresgpprqf	4	16384/32	10000.00/16.6583	16

Data processing

Bruker Topspin version 4.0.2 was used for processing of spectral data after acquisition, including fourier transformation, one-dimensional exponential window multiplication of the FID and phase correction. Baseline correction, window multiplication, linear prediction and phase correction was performed for spectral processing of decoupling in presence of scalar interactions (DIPSI) experiments. Bruker processing AU program proc_jres.be was used for processing of 2D J-resolved experiments. Hereby a back prediction produces a symmetric echo and as a result, FID and apodization maxima are on the very same spot.(137-139) Positive adsorptive projections of the processed two-dimensional JRES spectra were calculated for Chenomx. Pseudo two-dimensional reset psyche experiments were processed using Bruker AU program proc_reset.
F2 dimension processing was performed for saturation recovery experiments for T_1 determination. They were phase corrected and imported into Bruker Dynamics Center in order to determine T_1.(6)

Principal component analysis

In order to perform a principal component analysis (PCA) Matlab® vR2014a (Mathworks, Natick, Massachusetts, United States) was used. Unwanted/unnecessary regions around the water (4.7 ppm) and TSP (0 ppm) signals were cut, and finally probabilistic quotient normalization was performed to correct for differences in sample metabolite dilution.(6)
To reveal aberrant carbohydrate concentrations within urine samples, multivariate statistical analysis was performed using MetaboAnalyst 4.0.(6, 140)

Metabolite determination

Chenomx NMR Suite Professional 8.2 (Chenomx Inc.) was used for concentration determination of carbohydrates and creatinine. In order to do that, adsorptive positive projections of the indirect dimension of two-dimensional JRES spectra of lactulose, sucrose and mannitol with TSP as an internal standard were imported into the Chenomx NMR Suite Library Manager using the Compound Builder Module. Hereby, concentrations of the internal standard as chemical shape indicator and concentrations of carbohydrates were provided for the reference samples. Selection of NMR signals of interest in the isolated standard samples were used in order to provide a unique signature of carbohydrates in Chenomx profiler. Transformation of peak clusters was limited to a defined region, which enables a reliable assignment of peaks and their integration. Chenomx Profiler then used the reference data of Library Manager for integration and quantification.(6)

Automatisation of the presented approach was achieved by using a direct quantification from two-dimensional spectral data. Hereby, processed 2D JRES experiments were imported into MestReNova 11.0 and integral regions were selected in order to determine concentrations corresponding to carbohydrate/creatinine. Absolute concentrations were determined by using integrals of external standards with known concentrations (determined in MestReNova 11.0).(6)

Relaxation-enhancement experiments

In order to determine the suitability of paramagnetic relaxation enhancer (PRE) agents, standard samples of 100 µM sucrose, mannitol, lactulose and TSP were mixed with increasing gadolinium-chelate (Omniscan) or NiDo2A solutions. T1 determination experiments were performed with a modified version of the zggpw5 pulse sequence preceding a saturation recovery block (delays 0.01, 0.22, 0.54, 1.05, 1.84, 3.08, 5.01 (duplicated), 8.01, 12.69, 20 s) before the first 90° pulse and using water suppression with the w5 sequence (Bruker, size of fid 73728/11 F2/F1, 11904.76/5882.353 Hz spectral width in F2/F1, 128 scans, 0.1 s relaxation delay).

Results – Findings Part I

Axin-1^{DIX} domain harbors BSs within the Axin-1^{IDR}

Axin-1 mutations in human cancer patients comprise predominantly missense mutations and are found throughout the sequence of the gene.(141, 142) Findings of the Maurice lab indicated that Axin-1 constructs harboring cancer mutations within the Axin-1^{DIX} domain, but not in the oligomerization interface of the Axin^{DIX} (e.g. E816G), in contrast to the Axin-1 wildtype protein, lose the ability to form *puncta* when overexpressed in HeLa cells.(Fig. 7 A) In line with this finding, the mutant variant of Axin-1 shows in ß-catenin dependent luciferase assays an activation of the Wnt signaling pathway.(Fig. 7 B) Furthermore, *in vitro* NMR experiments of recombinant Axin-1^{DIX} indicate reduced oligomerization properties of Axin-1^{DIXE816G} compared to the wildtype version. (Fig. 10, Suppl. Fig. 1 A, B).

Since phase separation has already been reported to create microenvironments enabling distinct functions of the proteins, we speculate that this also holds true for Axin-1. Hereby, functional wildtype Axin-1 protein is capable of liquid demixing and subsequently forms cytoplasmic *puncta*. Due to high local Axin-1 concentrations, those *puncta* are highly efficient in downregulation of ß-catenin and, in line with this, Wnt signaling pathway is suppressed. Since the cancer variant deficient in *puncta* formation does not efficiently suppress the pathway, we hypothesize that this could be a general concept for phase separation in cancer: Phase separation might be essential for the proper function of protein complexes, which, in presence of a cancer mutation, will be disrupted and therefore results in non-functional protein complexes. In case of Axin-1, a non-functional complex will translate into high cytoplasmic and high nuclear levels of the transcriptional coactivator ß-catenin, finally leading to high transcriptional activity and cellular proliferation.

Based on these preliminary observations of our collaboration group at the UMC Utrecht, I aimed at deciphering the intramolecular interactions within Axin-1, which, in

combination with the Axin-1^{DIX}-Axin-1^{DIX} homo-oligomerization, might play a crucial role for Axin-1 regulation and phase separation.

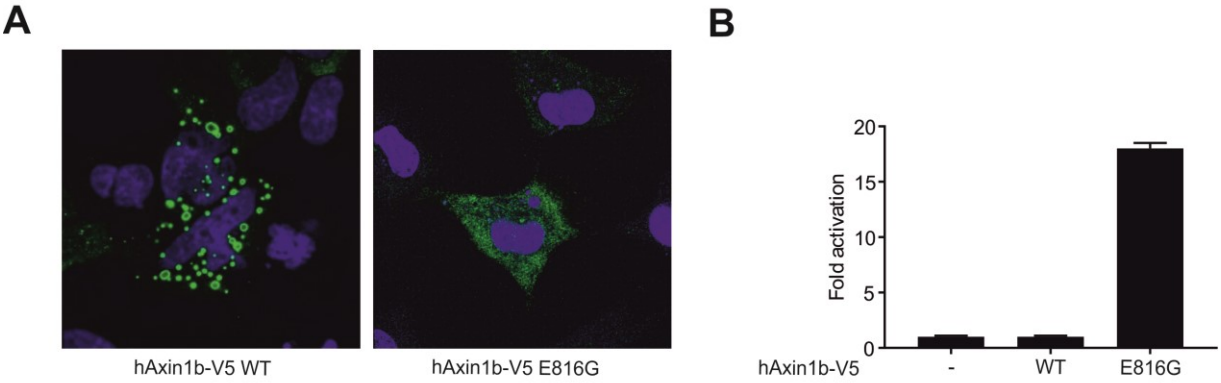

Figure 7: Axin-1^{DIX} cancer mutants lose the ability to form *puncta*. A. Immunofluorescence confocal microscopy in HeLa cells of hAxin-1b-V5. B. ß-catenin-dependent luciferase reporter assay of different Axin-1 variants. Data are represented as mean ± SD of 3 independent experiments.

In order to investigate this hypothesis, I studied fragments of recombinant protein Axin-1 *in vitro*. Therefore, Axin-1 constructs in a modified pET-M11 vector were transformed in *E.coli* BL21 DE3 and, after protein expression, recombinant proteins were purified using affinity chromatography and size exclusion chromatography steps. (see example purification in Figure 8)

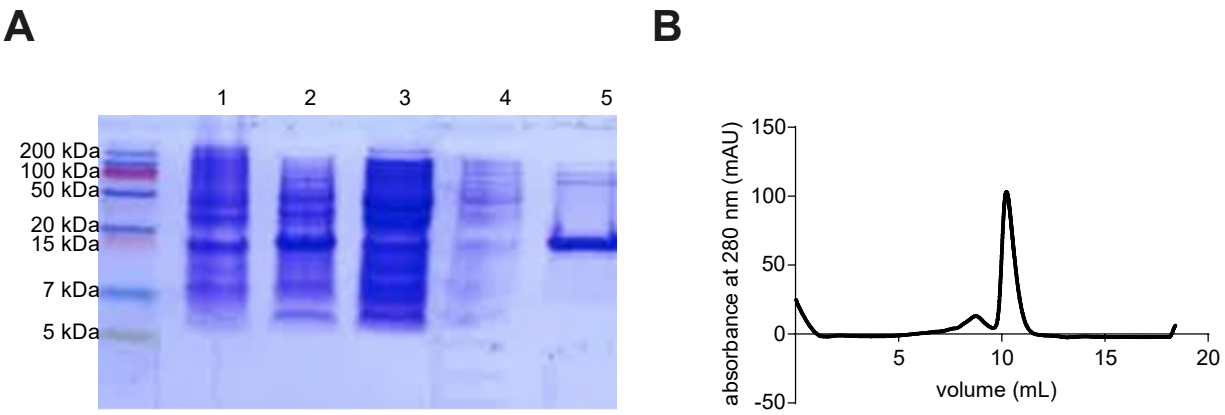

Figure 8: Protein purification from *E.coli* BL21 DE3. A. SDS gel for Axin-1^{DIX} purification with protein marker (prestained, dual color, BioRad). Lane 1: culture before induction, lane 2: culture after induction, lane 3: flow-through fraction on Ni-NTA column, lane 4: wash fraction on Ni-NTA column, lane 5: elution from Ni-NTA column. B. Size exclusion chromatography run of Axin-1^{DIX} on a Superdex 200 pg 300/10 Increase (GE Healthcare) on an Äkta pure purifier (GE Healthcare) in NMR buffer.

Recombinant protein fragments of Axin-1 were used for *in vitro* interaction studies. Since Axin-1^{DIX} is known to be an important feature for homo-oligomerization of Axin-1, we wonder whether the oligomerization property of the protein is largely affected in Axin-1^{DIXE816G} although the mutation is not located in the oligomerization interface (Fig. 9) and therefore *puncta* formation is disturbed in cell biology experiments.

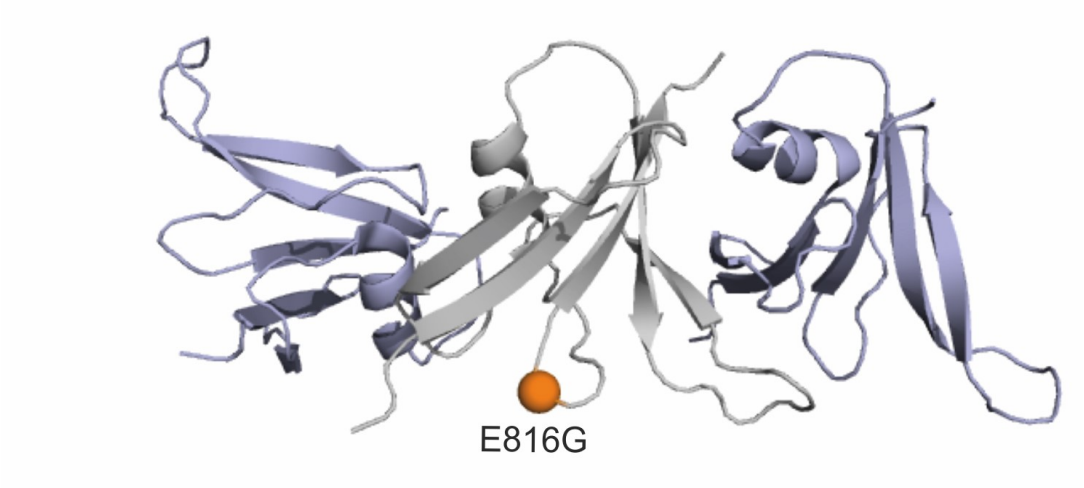

Figure 9: Structure of Axin-1^{DIX} with E816G mutation (orange). RCSB PDB: 1WSP

Hence, recombinant Axin-1^{DIX} and Axin-1^{DIXE816G} proteins were used for one-dimensional ^{1}H NMR experiments. Hereby the presence of methyl group signals in the spectral data was investigated. (Suppl. Fig. 1) In disordered proteins but also in highly oligomeric proteins, methyl group signals disappear in the spectrum due to the high flexibility or slow relaxation properties, respectively. At higher concentrations of Axin-1^{DIX} (> 20 µM), signals for methyl groups are lost due to the oligomeric state of the protein. (Suppl. Fig. 1, Fig. 10) Similar observation was made for Axin-1^{DIXE816G}, which goes in line with the fact that the cancer mutation is not located in the oligomerization interface of Axin-1.(Fig. 9) However, the intensity of Axin-1^{DIXE816G} methyl groups is at similar concentrations higher compared to Axin-1^{DIX}, which indicates that there is a slightly reduced oligomerization.

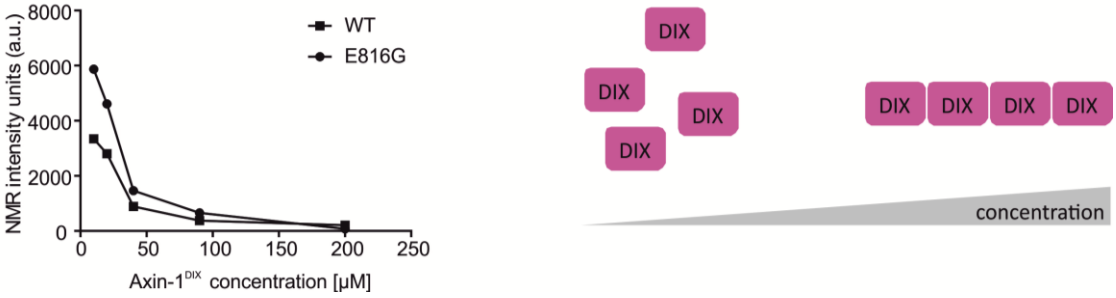

Figure 10: NMR intensity plot of methyl groups in Axin-1^{DIX} and Axin-1^{DIXE816G}. Intensities were extracted from ^{1}H 1D zggpw5 experiments of Axin-1^{DIX} and Axin-1^{DIXE816G} at different concentrations.

Based on current knowledge in literature, where the Xie He lab proposed a back-folding mechanism of the Axin-1^{DIX} domain to the Axin-1^{IDR} (63), we aimed at screening the Axin-1^{IDR} for interaction sites with the Axin-1^{DIX}. Out of various biophysical methods for studying protein-protein interactions, 2D ^{1}H, ^{15}N correlation NMR spectroscopy is perfectly suited in order to determine binding events in disordered proteins with amino acid resolution. Hereby, culturing medium of *E.coli* DE3 cells was supplemented with ^{15}N-enriched NH_4Cl and therefore incorporated in the protein produced by the bacteria. When recording a 2D ^{1}H, ^{15}N correlation experiment of the recombinant protein, with a few exceptions, each peak of the NMR spectrum corresponds to the amide backbone group of one given amino acid in the molecule. Due to an altered chemical environment upon binding, peaks tend to shift or disappear. (for schemes of used constructs see Fig. 11 A). By titrating non labelled Axin-1^{DIX} domain to a ^{15}N labelled Axin1^{IDR} construct (Axin-1$^{212-779}$), the interaction of Axin-1^{IDR} and Axin-1^{DIX} was confirmed. In this experiment, disappearance of signals of ^{15}N Axin-1$^{212-779}$ after addition of unlabelled Axin-1^{DIX} domain was observed for several residues. (Fig. 11 B) In contrast, the reverse experiment was not possible due to the highly oligomeric Axin-1^{DIX} domain. Hereby a severe loss of signal due to extensive line broadening of the oligomeric protein was observed. (Fig. 11 C)

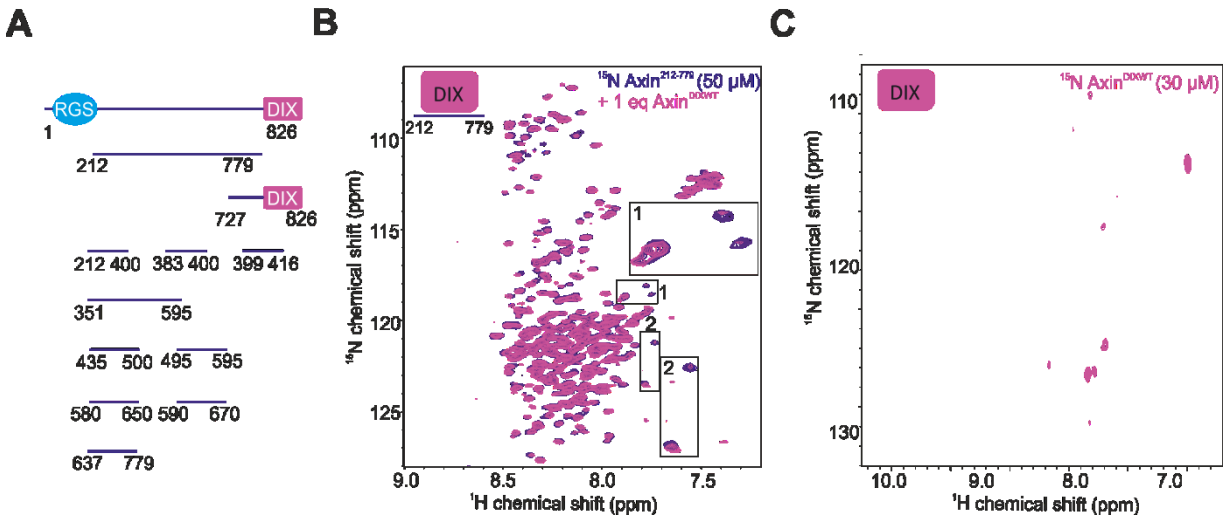

Figure 11: Interaction studies of Axin-1^{IDR} with Axin-1^{DIX}. A. Scheme of constructs used for *in vitro* experiments. B. 2D ^{1}H, ^{15}N HSQC NMR spectra of ^{15}N Axin-1^{IDR} in absence (blue) or presence (magenta) of non-labelled Axin-1^{DIX} domain. C. 2D ^{1}H, ^{15}N HSQC NMR spectrum of ^{15}N Axin-1^{DIX}.

Since wildtype Axin-1^{DIX} domain of the protein Axin-1 is not accessible to NMR-based studies (Fig. 11 C), we used for our studies an oligomerization deficient variants of the protein.(129). Hereby, amino acid exchanges of V801A and F802A lead to decreased oligomerization properties of the protein for Axin-1^{DIXM2}, whereas Axin-1^{DIXM3} harbors mutations in I758A and R761D. Therefore both proteins were visible in our ^{1}H, ^{15}N correlation experiments (Fig. 12, Fig. 13), in contrast to Axin-1^{DIX} (Fig. 11 C).

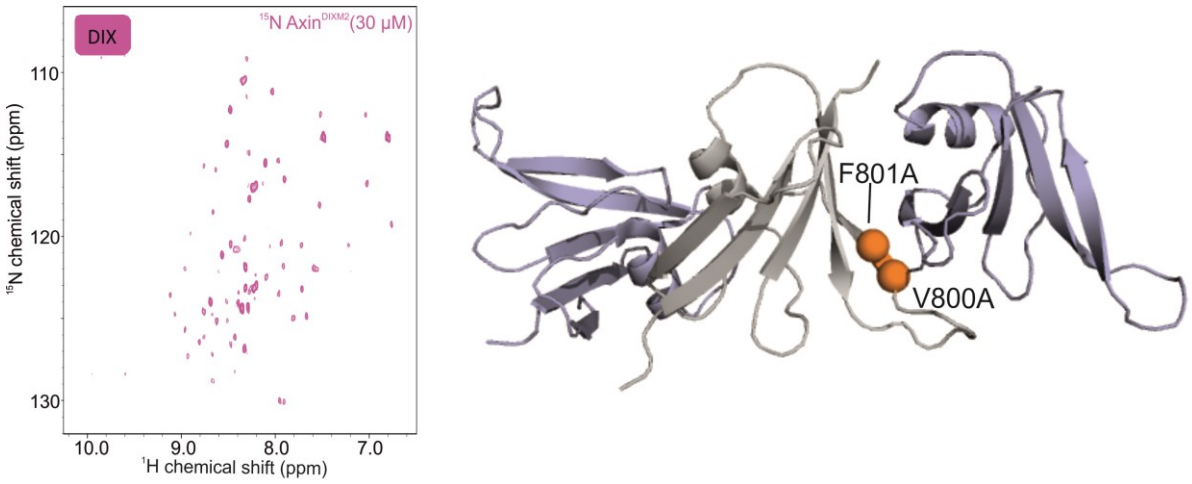

Figure 12: Axin-1^{DIX} with M2 mutations. 2D ^{1}H, ^{15}N HSQC NMR spectrum of ^{15}N Axin-1^{DIXM2} (V801A and F802A). RCSB PDB: 1WSP. Structure of Axin-1^{DIXM2} (mutations in orange).

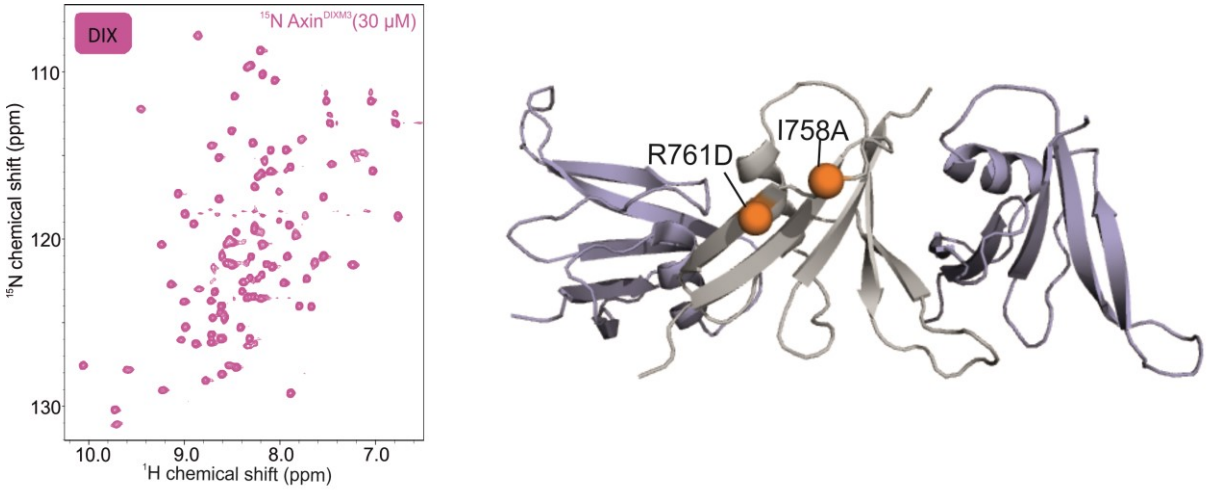

Figure 13: Axin-1^{DIX} with M3 mutations. 2D ^{1}H, ^{15}N HSQC NMR spectrum of ^{15}N Axin-1^{DIXM3} (I758A and R761D). RCSB PDB: 1WSP. Structure of Axin-1^{DIXM3} (mutations in orange).

Due to the overlapping signals in the approx. 500 amino acid long construct Axin-$1^{212-779}$ (Fig. 11 B), the exact assignment of the affected regions in the protein remained difficult. Therefore, we aimed at narrowing potential binding sites down using smaller Axin-1^{IDR} constructs. We covered the entire intrinsically disordered region in Axin-1 using Axin-$1^{212-400}$, Axin-$1^{351-595}$, Axin-$1^{590-670}$ and Axin-$1^{637-779}$, and by titrating those constructs with either Axin-1^{DIXM2} or Axin-1^{DIXM3}. (Suppl. Fig. 2, Suppl. Fig. 3) Those experiments revealed that Axin-1^{DIXM3} does not interact with Axin-1^{IDR}. We hypothesized that this is due to a localization of the Axin-1^{DIXM3} mutations close to or within the Axin-1^{IDR} binding interface.

For Axin-1^{DIXM2}, in contrast to current knowledge in literature (59, 63), we could localize three distinct binding events in the Axin-1^{IDR}. Based on those results, we continued with our experiments using Axin-1^{DIXM2} and we determined three different constructs to further study and narrow down the binding events (Axin-$1^{435-500}$, Axin-$1^{495-595}$ and Axin-$1^{580-650}$). In order to perform detailed interaction studies of Axin-1^{IDR} fragments and Axin-1^{DIXM2}, isolated spectra of the selected Axin-1^{IDR} fragments were recorded.(Fig. 14 A-C) For extensive studies of interacting amino acids in Axin-1^{IDR} with Axin-1^{DIXM2}, it is inevitable to assign the signals in the NMR spectrum to given amino acids in the spectrum. Therefore triple resonance experiments were recorded of Axin-1 constructs enriched in ^{13}C and ^{15}N nuclei. Those experiments which use scalar and dipolar couplings between nuclei in order to determine their connectivity (e.g. (H)N(CA)NH). For sequential assignments, correlated nuclei (^{1}H, ^{15}N) are connected in a third carbon dimension with one or more additional nuclei (e.g. $^{13}C\alpha$ or $^{13}C\beta$). Neighboring residues in ^{15}N backbone are identified, if corresponding frequencies in NMR spectra match. Those experiments enable to create chains of sequentially connected residues, which might be interrupted by missing NMR signals (e.g. prolines). Typically, data about connectivity of residues is complemented using backbone assignment experiments (e.g. HNCACB, HN(CO)CACB). In the HNCACB experiment, magnetization from a given ^{1}H group is transferred to the $^{13}C\alpha$ and $^{13}C\beta$ nuclei of the side chain of itself and of the preceding residue, and back to $^{1}H^{N}$ group for detection. In those spectra, four signal are observed for $^{13}C\alpha$ and $^{13}C\beta$ nuclei of residue i and $^{13}C\alpha$ and $^{13}C\beta$ nuclei of residue i-1 (with the exception of glycine which harbors only $^{13}C\alpha$). In contrast,

HN(CO)CACB transfers the magnetization only to the preceding residue, thereby results only in two signals ($^{13}C_{\alpha}$ and $^{13}C_{ß}$ nuclei of residue i-1). Using those experiments, chemical shift of $^{13}C_{\alpha}$ and $^{13}C_{ß}$ enable the identification of the amino acid.

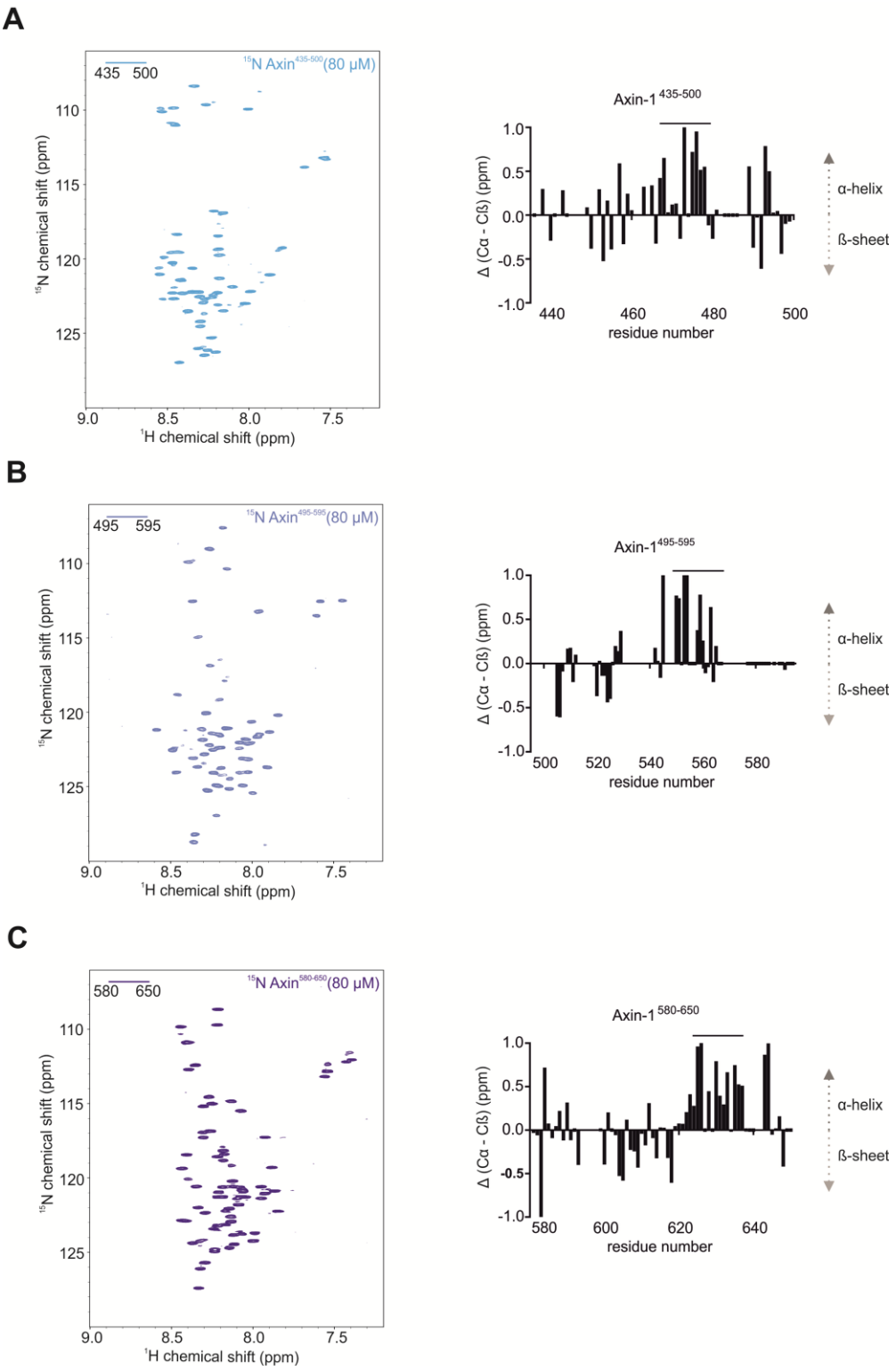

Figure 14: Axin-1^{IDR} fragments for Axin-1^{DIXM2} interaction studies. 2D ^{1}H, ^{15}N HSQC NMR spectra of A. ^{15}N Axin-1$^{435-500}$, B. ^{15}N Axin-1$^{495-595}$ and C. ^{15}N Axin-1$^{580-650}$ with corresponding secondary chemical shifts.

Chemical shifts of protein backbones are sensitive to local backbone geometry, thereby providing information about secondary structural elements. The used fragments in the experiments are intrinsically disordered, however, they can adopt transient secondary structures which might indicate favored sites for protein-protein interactions. Therefore data about chemical shifts of $^{13}C_{\alpha}$ and $^{13}C_{ß}$ nuclei were used in order to determine deviations from random coil chemical shifts. Hereby, positive $^{13}C_{\alpha} - ^{13}C_{\beta}$ values indicate a tendency to form alpha-helical structures and negative $^{13}C_{\alpha} - ^{13}C_{\beta}$ values indicate a tendency to form ß-stranded structures. For Axin-$1^{435-500}$, Axin-$1^{495-595}$ and Axin-$1^{580-650}$ we found stretches of positive $^{13}C_{\alpha} - ^{13}C_{\beta}$ values in each disordered fragment indicated with a line (around residue 480, 560 and 630), indicating that those regions are likely to form alpha helical structures and might be interesting protein-protein interaction sites.(Fig. 14) In addition, relaxation experiments are a useful tool for the determination of flexibility of protein regions. Secondary structure elements are more rigid, therefore HetNOE values are positive, whereas highly flexible disordered regions have largely negative values. HetNOE experiments recorded from Axin-$1^{435-500}$ and Axin-$1^{580-650}$ confirmed a rigidity of the constructs around residue 480 and 630, fitting to the secondary chemical shift data. Additional relaxation experiments of Axin-$1^{495-595}$ might provide another confirmation for the alpha helical propensity of the region around residue 560.(Suppl. Fig. 4)

In order to confirm that Axin-1^{DIXM2} interacts with those Axin-1^{IDR} constructs, unlabeled Axin-1^{DIXM2} was added to ^{15}N enriched Axin-1^{IDR}. All the different binding events affected approximatively 10-15 amino acids. With $^{1}H^{N}$ and $^{15}N^{H}$ chemical shift information, the $^{1}H/^{15}N$ normalized chemical shift perturbation for each residue can be calculated to identify residues affected by the binding event. With this setup I was able to determine three different BSs of the Axin-1^{DIXM2} within the flexible linker region from 438-455 (BS 1), 559-571 (BS 2) and 628-640 (BS 3).(Fig. 15)

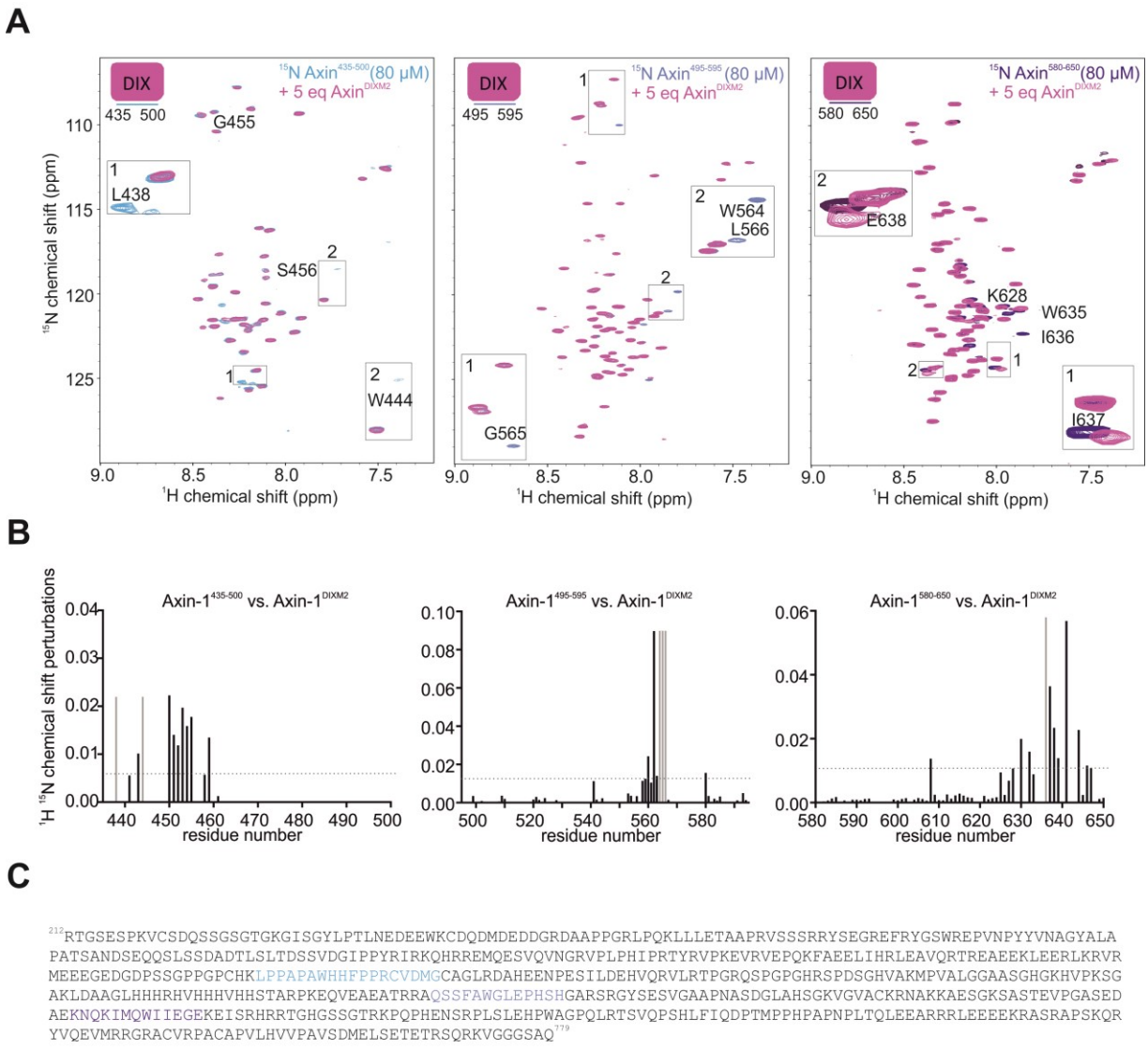

Figure 15: *In vitro* binding studies of Axin-1^{DIXM2} to Axin-1^{IDR} A. 2D ^{1}H, ^{15}N HSQC NMR spectra of ^{15}N Axin-1^{IDR} in absence (blue) or presence (magenta) of non-labelled Axin-1^{DIXM2} domain. Affected peaks within the binding region are indicated. B. Corresponding CSP plots of titration experiments are shown. C. Sequence with mapped binding sites of Axin-1^{DIXM2}.

Since the mapped regions with alpha helical propensities are favored protein-protein interaction sites, we determined whether or not those sites overlap with the mapped Axin-1^{DIXM2} binding sites. Interestingly, BS 2 and BS 3 are located within the structured region, but BS 1 is not.(Fig. 16)

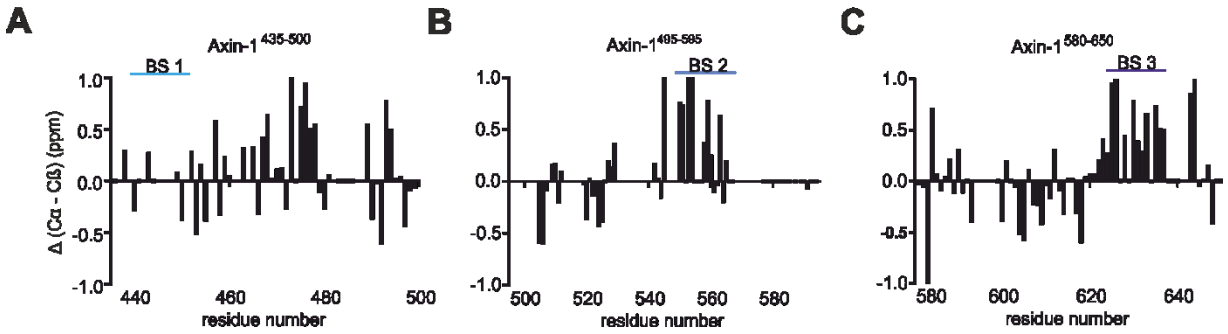

Figure 16: Axin-1^{IDR} fragments for Axin-1^{DIXM2} interaction studies. Secondary chemical shift plots and indication of Axin-1^{DIXM2} binding sites.

Axin-1 auto-inhibition does not interfere with oligomerization

Due to the lack of high oligomeric assemblies of the Axin-1^{DIXM2} (129), line broadening in NMR experiments is reduced and therefore the protein is visible in 2D ^{1}H, ^{15}N HSQC NMR spectra. Based on the binding studies of Axin-1^{IDR} constructs to the Axin-1^{DIX} domain (Fig. 15), these three constructs were used for binding studies to the ^{15}N labelled Axin-1^{DIXM2} domain. On the one hand those NMR experiments enabled detection of the binding interface on the Axin-1^{DIX} and on the other hand to tackle the question whether this intra-molecular binding of Axin-1 interferes with the Axin-1^{DIX}-dependent oligomerization of the protein by binding to the oligomerization interface determined by crystallography.(143) By titrating unlabelled Axin1$^{435-500}$, Axin-1$^{495-595}$ or Axin-1$^{580-650}$ to a ^{15}N labelled Axin-1^{DIXM2} construct, two different regions in the sequence involved in the binding event were identified (748-753, 815-826). (Fig. 17 A-C)

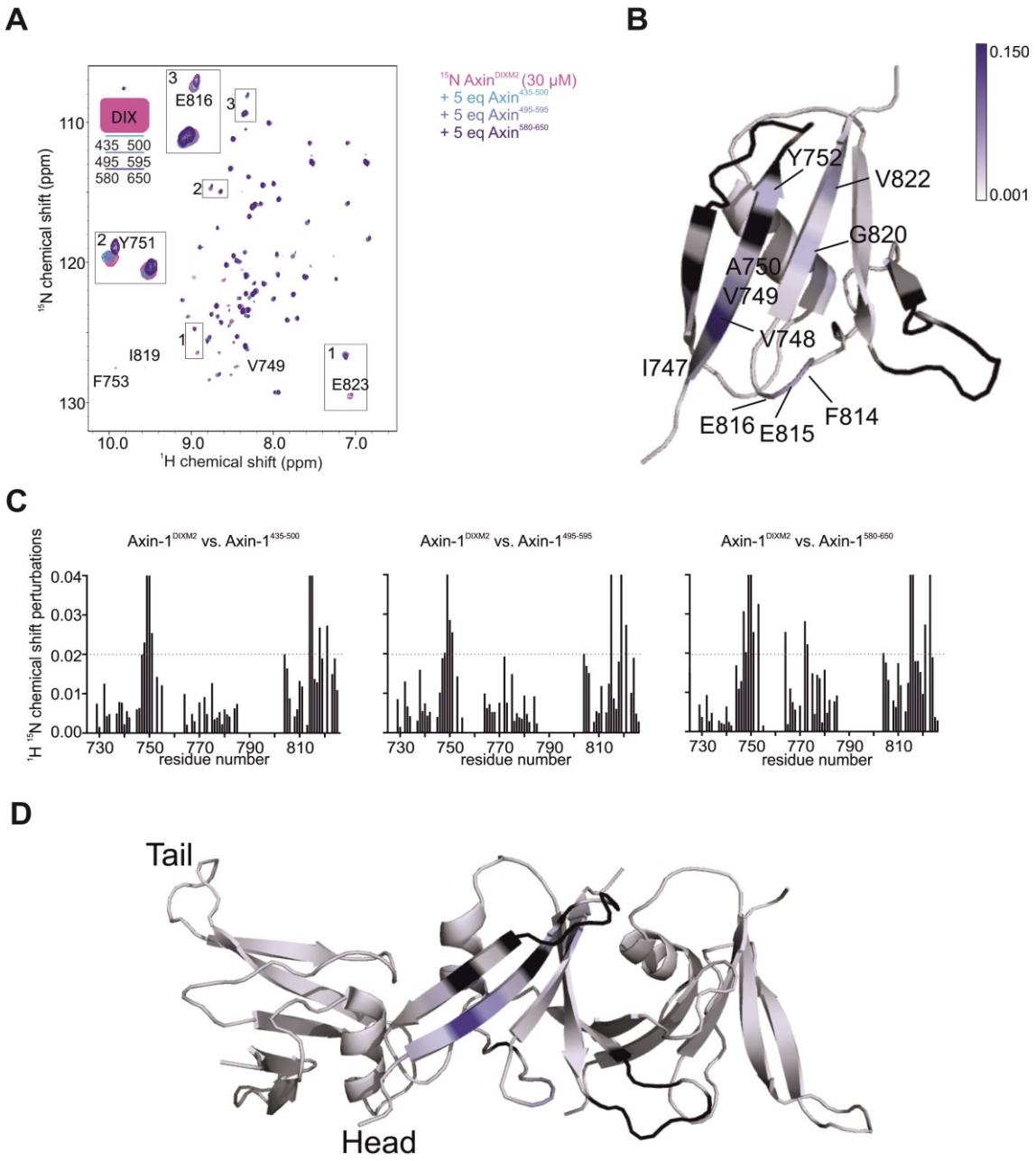

Figure 17: *In vitro* binding studies of Axin-1^{IDR} to Axin-1^{DIXM2} A. 2D ^{1}H, ^{15}N HSQC NMR spectra of ^{15}N Axin-1^{DIXM2} in absence (magenta) or presence (blue) of non-labelled Axin-1^{IDR}. Affected peaks within the binding region are indicated. B. Binding sites of Axin-1^{IDR} to Axin-1^{DIXM2} colored by CSP values in structure of Axin-1^{DIX}. RCSB PDB: 1WSP. C. Corresponding CSP plots of titration experiments are shown. D. Binding sites of Axin-1^{IDR} to Axin-1^{DIXM2} colored by CSP values in the oligomer structure. RCSB PDB: 1WSP.

Those two sequence regions are located in adjacent ß-sheets in the structure, providing a binding interface for the flexible part. (Fig. 17 B) (143) These experiments show, that only one binding interface within the Axin-1^{DIX} is responsible for the binding event of three different Axin-1^{IDR} fragments. This feature fits well to the expected multivalency in phase separation. Finally, those two ß-sheets are not located in the region involved in head-to-tail oligomer formation (Fig. 17 D). In addition, the interaction interface is very close to the Axin-1^{DIXM3} mutations, therefore the interaction might be affected in this construct.

Axin-1^{DIX} binding does not interfere with ß-catenin binding

The Xie Helab proposed an Axin-1^{DIX}-dependent displacement of ß-catenin from Axin-1 in the non-phosphorylated state.(63) The displacement of ß-catenin or the competition of ß-catenin and the Axin-1^{DIX} domain point to a reduced ß-catenin destruction and therefore activation of the Wnt pathway.(Fig. 18) When using CHIR99021, a GSK3ß inhibitor, in HEK293T cells transfected with Axin-1 or empty vector, the GSK3ß mediated phosphorylation is reduced. This results in a high activation of the Wnt signaling pathway in ß-catenin dependent luciferase assays. This can be due to a reduction in phosphorylated Axin-1 or due to a reduction in ß-catenin phosphorylation. (Fig. 18)

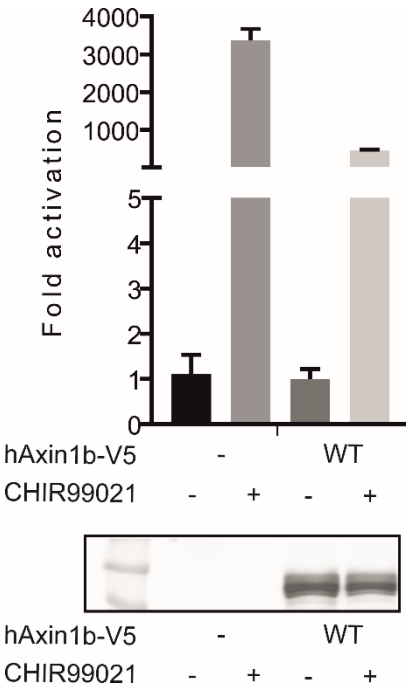

Figure 18: Wnt pathway activation in absence of post-translational phosphorylation. ß-catenin dependent luciferase reporter assay of empty vector and Axin-1 in presence and absence of GSK3ß-mediated phosphorylation using CHIR99021 (GSK3ß inhibitor). Data are represented as mean ± SD of 3 independent experiments.

The ß-catenin interaction site on Axin-1 has already been mapped around residue 475.(144) In addition, recent data of the Madl lab revealed a novel BS of ß-catenin within the disordered region of Axin-1 around residue 390 (data not shown). Since the investigated BS 1 does not overlap with the mapped ß-catenin binding sites around residue 400, the displacement of ß-catenin from Axin-1 due to steric inhibition by Axin-1^{DIX} binding event was disconfirmed. The region in Axin-1 close to the more C-terminal Axin-1^{DIX} BS has not yet been screened for ß-catenin binding. Therefore, it was important to prove that ß-catenin displacement is also not happening at the region of BS 2 or BS 3. In order to do that, non-labelled ß-catenin was titrated to the ^{15}N labelled Axin-1 constructs Axin-$1^{495-595}$ or Axin-$1^{580-650}$. Due to the absence of any shifting/disappearing peaks, we concluded that there are no additional ß-catenin binding events happening in those regions. This indicates that there is no direct interference of Axin-1^{DIX} binding to ß-catenin binding. (Fig. 19)

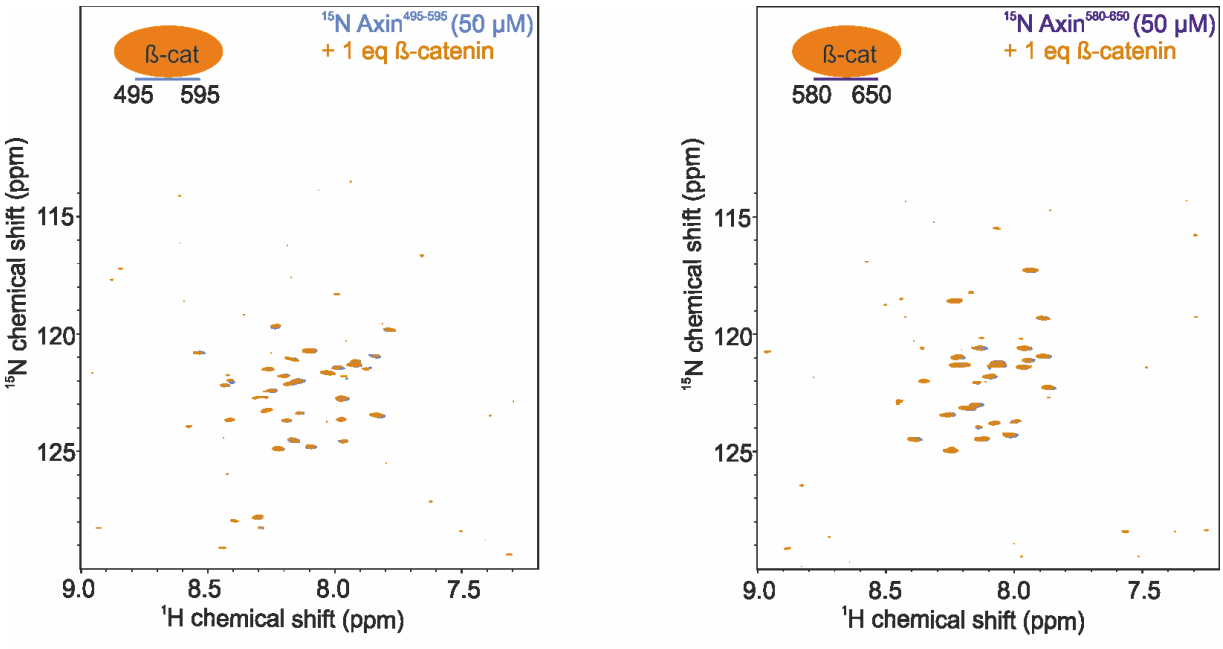

Figure 19: Screening for ß-catenin binding events on Axin-1^{IDR}. A.2D ^{1}H, ^{15}N HSQC NMR spectra of ^{15}N Axin-1$^{495-595}$ in absence (blue) or presence (magenta) of ß-catenin. B. 2D ^{1}H, ^{15}N HSQC NMR spectra of ^{15}N Axin-1$^{580-650}$ in absence (blue) or presence (magenta) of ß-catenin.

Dephosphorylation does not dissolve *puncta*

Since the study of the Xie Helab (28) suggests an important role of phosphorylation, we speculated whether phosphorylation might also influence *puncta* formation. Their study suggested that the active protein is phosphorylated, whereas the non-phosphorylated protein is inactive. We therefore started with the investigation of the interaction of one of the key kinases in the ß-catenin destruction complex, GSK3ß, with Axin-1 *in vitro*. At first, we confirmed the interaction using 2D ^{1}H, ^{15}N HSQC NMR spectra of Axin-$1^{351-500}$ in presence and absence of GSK3ß. As already reported in literature, the interaction of Axin-1 with GSK3ß affects residues around amino acid 400 in Axin-1.(115) In our experiments, residues from 380-430 are affected. (Fig 20 A, B) When investigating the affinity of the interaction using isothermal titration calorimetry (ITC), the k_D of the interaction of GSK3ß and Axin-1 is in the low nanomolar range (31 ± 4.6 nM).(Fig. 20 C) In addition, recombinant GSK3ß was able to phosphorylate residues in Axin-$1^{351-500}$ in presence of ATP and $MgCl_2$. This phosphorylation event can be seen as newly appearing signals in the spectrum at higher chemical shifts (Fig 21 A). When monitoring kinetics of the three phosphorylated residues, (Fig. 20 B), all of them were phosphorylated at the same time, which leads to the assumption that there is no GSK3ß-mediated priming phosphorylation using this time resolution. The GSK3ß binding site on Axin-1 has been mapped from residue 383-401, however since we see also peaks above residue 400 affected in NMR experiments, we used two different fragments (Axin-$1^{383-400}$, Axin-$1^{399-416}$) for further ITC experiments. Hereby, we could show that only the fragment of Axin-$1^{383-400}$ is capable of GSK3ß binding, however, the affinity is weaker than for Axin-$1^{351-500}$ (31 ± 4.6 nM vs. 163 ± 13 nM). SAXS data of the Axin-1/GSK3ß complex indicate that two GSK3ß molecules are present on one Axin-$1^{351-500}$ fragment. (Fig. 21 A-C) Therefore it can be speculated, that the binding events are sequential and that one GSK3ß has to be bound to the first binding site (Axin-$1^{383-400}$) and then enabling the binding of the second GSK3ß molecule (Axin-$1^{399-416}$).

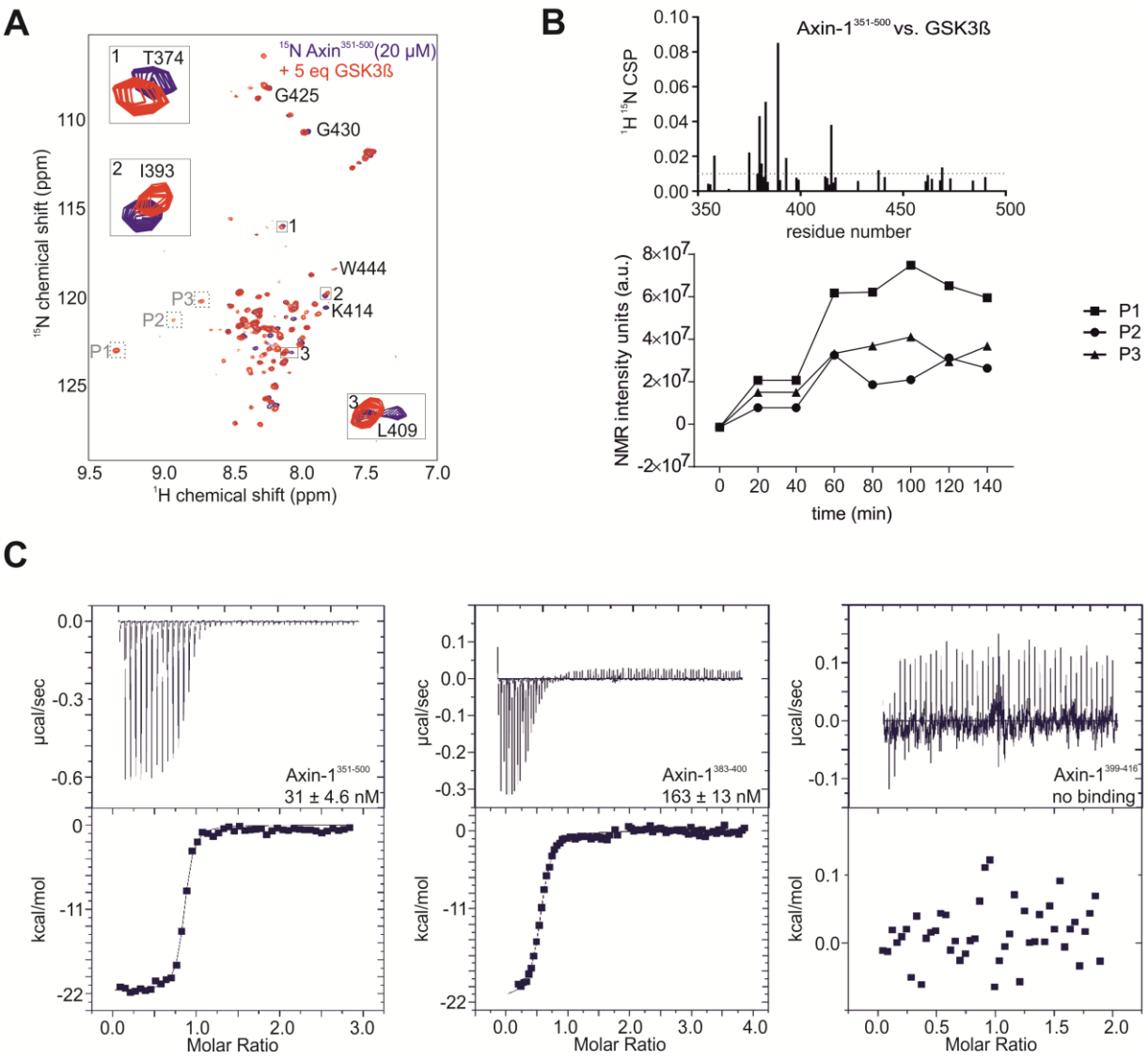

Figure 20: *In vitro* characterization of Axin-1/GSK3ß interaction. A.2D ^{1}H, ^{15}N HSQC NMR spectra of ^{15}N Axin-1$^{351-500}$ in absence (blue) or presence (red) of GSK3ß. Additional peaks appeared due to phosphorylation events in presence of ATP and $MgCl_2$. B. Phosphorylation kinetic of phosphorylated residues in 2D ^{1}H, ^{15}N HSQC NMR spectra of ^{15}N Axin-1$^{351-500}$. B. Corresponding CSP plot for the interaction. C. ITC binding curves for GSK3ß binding to Axin-1$^{351-500}$($\Delta H = -1.97*10^4 \pm 1.78*10^2$ and $\Delta S = -31.6$; n = 3), Axin-1$^{383.400}$ ($\Delta H = -2.15*10^4 \pm 2.47*10^2$ and $\Delta S = -41.1$, n =1) and Axin-1$^{399-416}$ (no binding, n = 1).

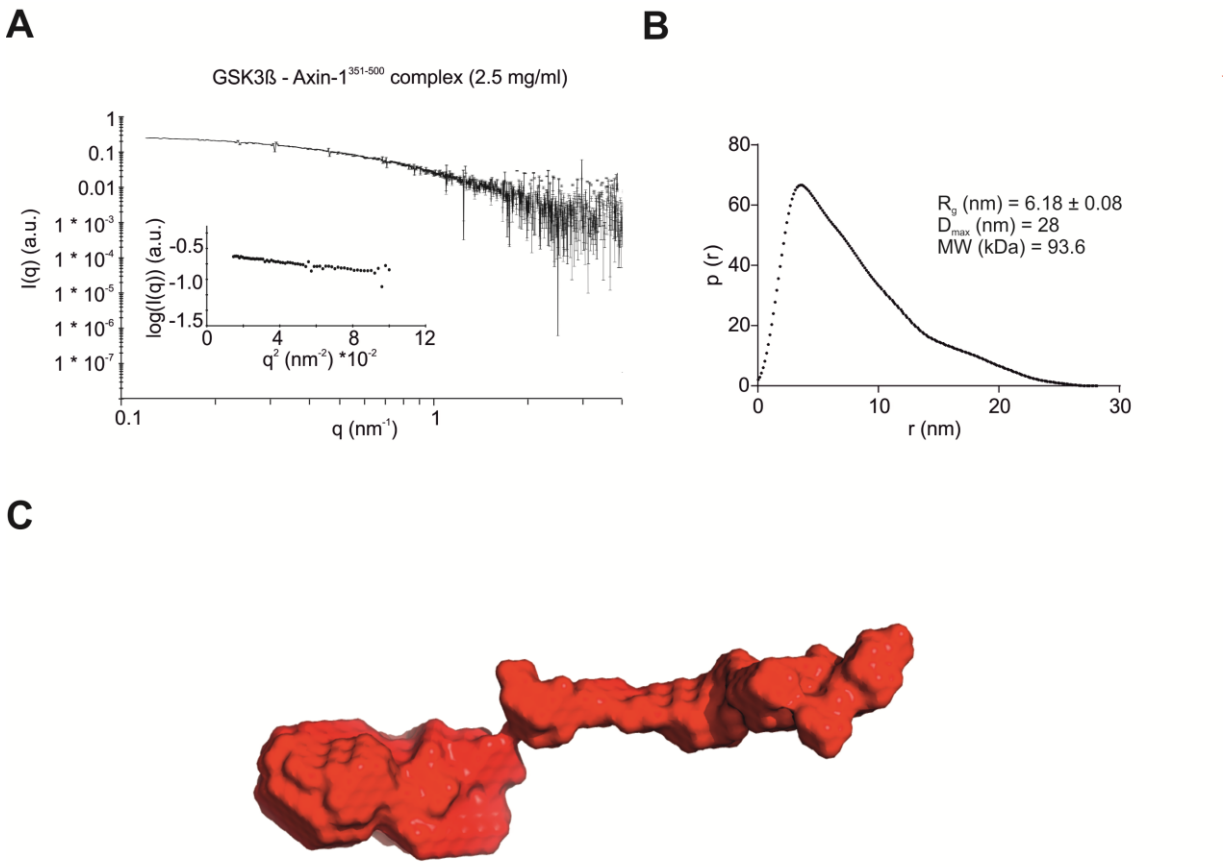

Figure 21: *In vitro* characterization of Axin-1/GSK3ß interaction. A. SAXS raw data for Axin-1$^{351-500}$/GSK3ß complex and corresponding Guinier plot. B. SAXS data showing the experimental radial density distribution p(r) of Axin-1 in complex with GSK3ß. C. Surface/low resolution SAXS model for Axin-1$^{351-500}$/GSK3ß complex based on SAXS curve data.

In cells, we tested the importance of phosphorylation and therefore tested whether we can dissolve *puncta* through removal of phosphorylation by using CHIR99021, overexpression of phosphatases or deletion of the GSK3ß binding site. In all conditions we did not observe any differences in *puncta* formation in absence of phosphorylation (CHIR99021, phosphatases or deletion of GSK3ß BS). (Fig. 22 A) However, Axin-1 activity in presence of GSK3ß inhibitor CHIR9901 was tested, which revealed Wnt pathway activation in absence of phosphorylation in ß-catenin dependent luciferase

assays. (Fig. 22 B) With this experiments it was confirmed that dephosphorylation does regulate Axin-1 activity (shown for CHIR99021), but is not sufficient to dissolve *puncta*.(Fig. 22 A, B) However, CHIR99021 or phosphatase treatment, but also deletion of the GSK3ß binding site on Axin-1, does not only affect phosphorylation status of Axin-1, but also of APC or ß-catenin. Therefore, an increased pathway activation in those conditions does not contradict the investigated correlation between *puncta* and active Axin-1.

A

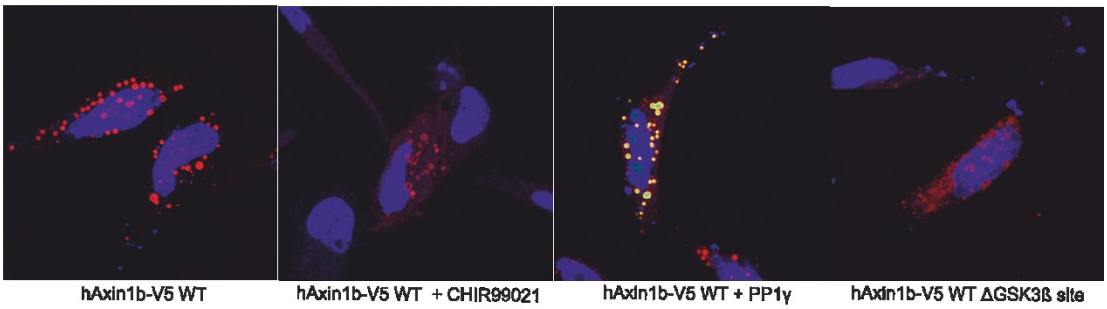

B

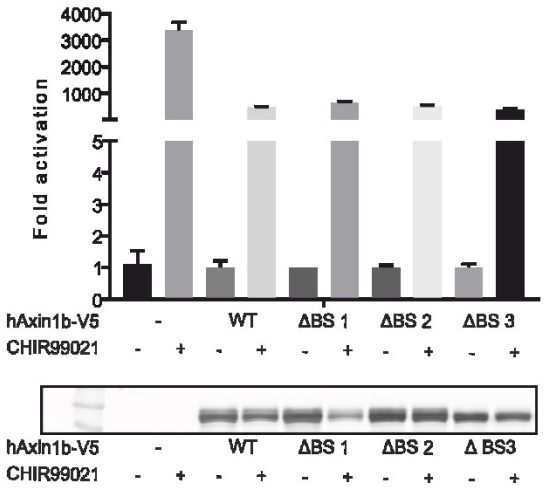

Figure 22: Phosphorylation does not disrupt *puncta* formation. A. Immunofluorescence confocal microscopy in HeLa cells of hAxin-1b-V5. B. ß-catenin dependent luciferase reporter assay of different Axin-1 variants in presence of GSK3ß inhibitor CHIR99021. Data are represented as mean ± SD of 3 independent experiments.

A

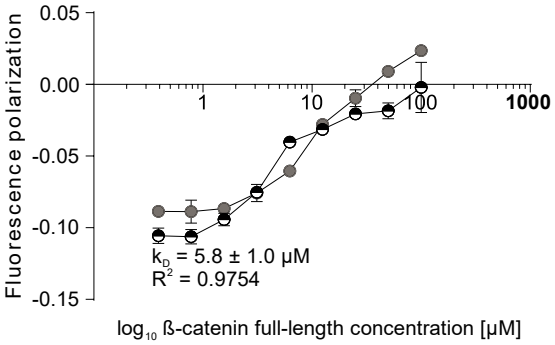

B

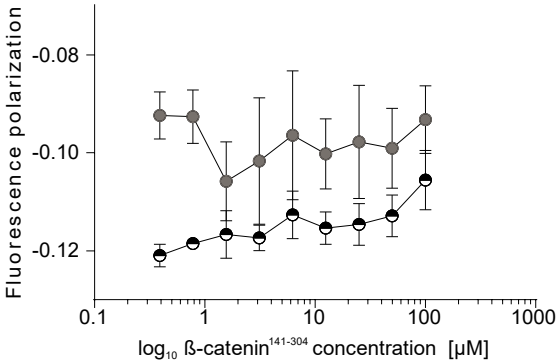

C

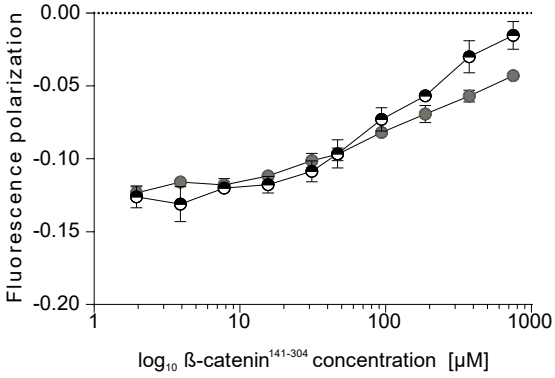

Fig. 23: Fluorescence polarization data for FITC-tagged Axin-1 peptides in absence and presence of phosphorylation. Binding data for Axin-1$^{459-496}$ to ß-catenin with or without phosphorylated key residues. B. Binding data for Axin-1$^{459-496}$ to an N-terminal ß-catenin construct (ß-catenin$^{141-304}$) with or without phosphorylated key residues. C. Binding data for Axin-1$^{459-496}$ to an N-terminal ß-catenin construct (ß-catenin$^{141-304}$) with or without phosphorylated key residues at high concentration.

Data are represented as mean ± SD of 3 independent experiments.

Four key phosphorylated residues of Axin-1 have been described so far to be crucial for ß-catenin binding by the Xie Helab.(63) Therefore, we tested FITC-tagged Axin-1 peptides for ß-catenin binding in presence and absence of phosphorylation using fluorescence anisotropy experiments. In presence of full-length ß-catenin, the non-phosphorylated peptide showed a reduced binding compared to the phosphorylated peptide ((Fig. 23 A) low µM range). When using the construct harboring only the N-terminal Arm repeats 1-4 (ß-catenin$^{141-304}$), the binding was not detectable at similar concentrations to full-length ß-catenin. (Fig. 23 B) By increasing the concentration of ß-catenin$^{141-304}$ there was a binding event detectable in the high µM range. (Fig. 23 C) However, in this construct, there was no clear difference between the phosphorylated and non-phosphorylated peptide observed. This might be explained by the fact that ß-catenin$^{141-304}$ only contains those residues that interact with the mapped ß-catenin binding domain of Axin-1 in the available crystal structure of Axin-1 in complex with ß-catenin. The binding region of the phosphorylated residues on ß-catenin is not determined yet, and might not be present in ß-catenin$^{141-304}$.(145)

Deletion of single BSs is not sufficient to dissolve *puncta*

Based on previous experiments, it was discovered, that Axin-1 has different intra-molecular interaction sites between Axin-1^{DIX} and Axin-1^{IDR}. In addition, those BSs in the Axin-1^{IDR} do not interfere with ß-catenin binding to Axin-1. Therefore, the importance of the distinct BSs was still elusive. In order to study the function of the BSs, Bs were deleted in wildtype Axin-1 and the different constructs were expressed in HeLa cells. In ß-catenin dependent luciferase assay experiments no change in pathway activation was observed, and in line with this, *puncta* formation was not disrupted as seen by immunofluorescence microscopy. (Fig.24 A, B) Those data support the correlation between *puncta* formation and their ability to suppress the Wnt pathway. However, the deletion of single BSs did not alter protein function, which suggests that the BSs can compensate for each other.

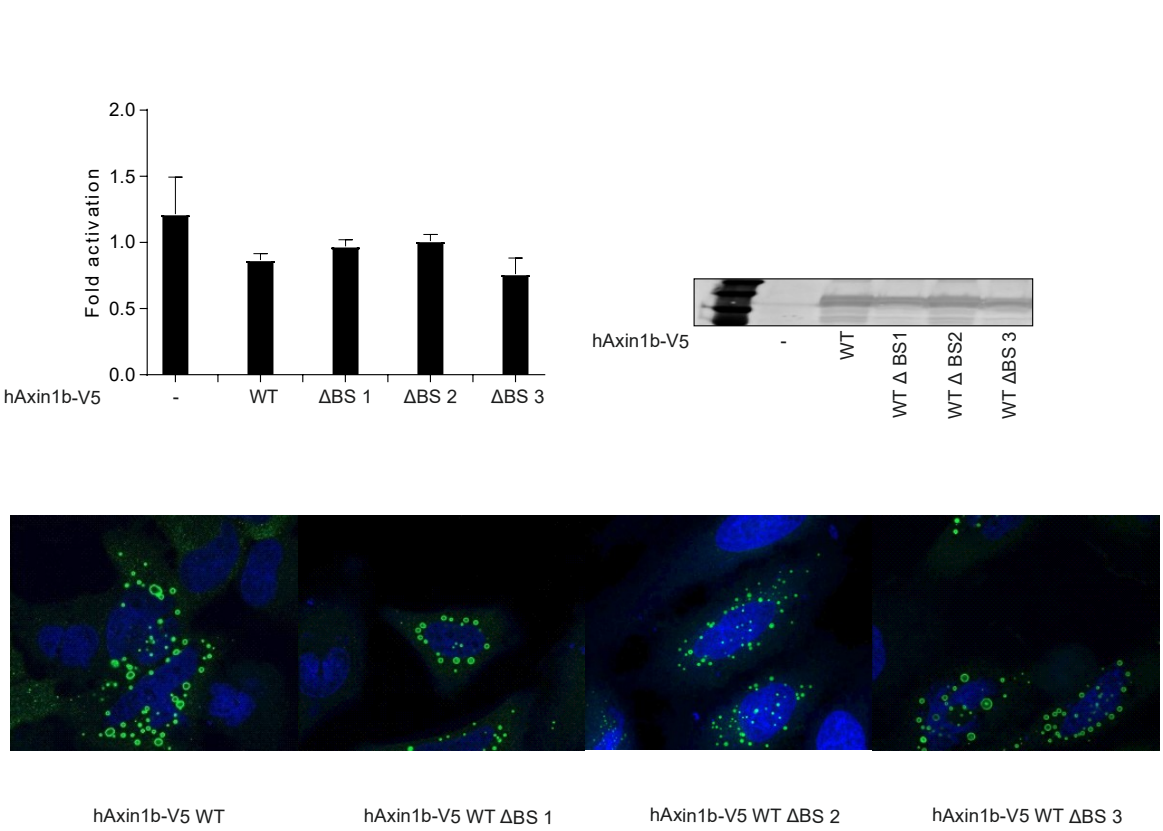

Figure 24: Deletions of BSs in Axin-1 WT. A.ß-catenin dependent luciferase reporter assay of different Axin-1 variants. Data are represented as mean ± SD of 3 independent experiments. B. Immunofluorescence confocal microscopy in HeLa cells of hAxin-1b-V5.

BS deletions restore *puncta* formation in presence of a cancer mutation

Since we could not read out the function of the distinct BSs in the wildtype protein, we used a pathway activating cancer mutant of the Axin-1^{DIX} domain incapable of phase separation in the cytoplasm as a sensitized model system. In addition, this cancer mutation was chosen, because the amino acid exchange in E816G is located within the mapped binding interface in the Axin-1^{DIX} domain. Therefore, it is a highly sensible system in order to reveal differences in the function of the mapped BS.

In context of the cancer variant E816G, we deleted the distinct BSs and screened those proteins for Wnt pathway activation as well as for *puncta* formation. Interestingly, all three deletions of BS in Axin-1 E816G restored the disrupted *puncta* formation in the

cancer mutant, which also correlated with Wnt pathway suppression to wildtype level. (Fig. 25 A, B; data for E816GΔ1 of collaboration partner not shown) Those results indicate that those binding sites are a potential target for therapies.

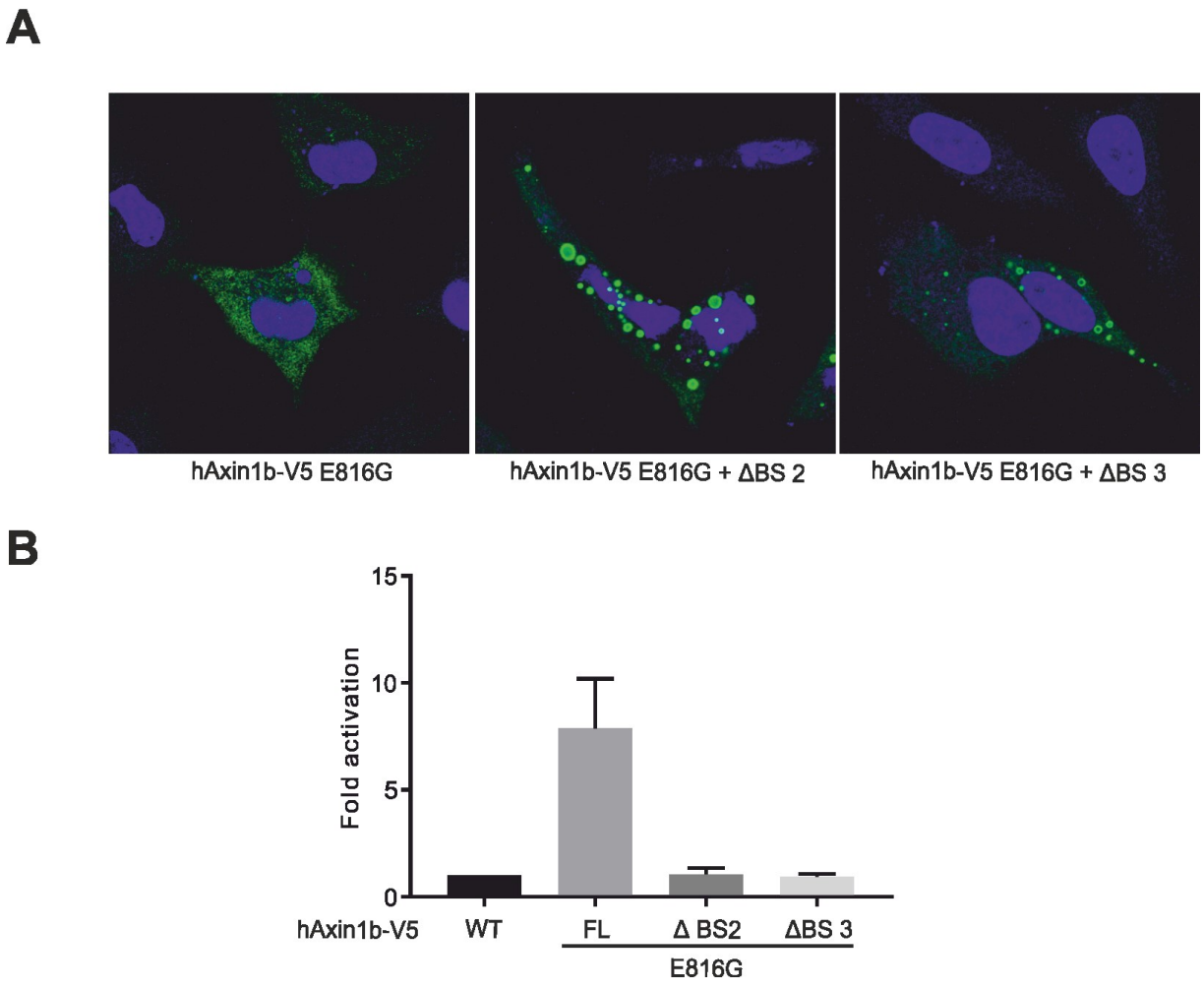

Figure 25: Deletion of BS restores *puncta* formation in E816G. A.Immunofluorescence confocal microscopy in HeLa cells of hAxin-1b-V5. B. ß-catenin dependent luciferase reporter assay of different Axin-1 variants. Data are represented as mean ± SD of 3 independent experiments.

In addition, we repeated our NMR-based experiment with the Axin-1^{DIX} mutant variant (E816G). In order to do this, we used the oligomerization deficient mutant variant Axin-1^{DIXM2} in context of the cancer mutation E816G.(Fig. 26)

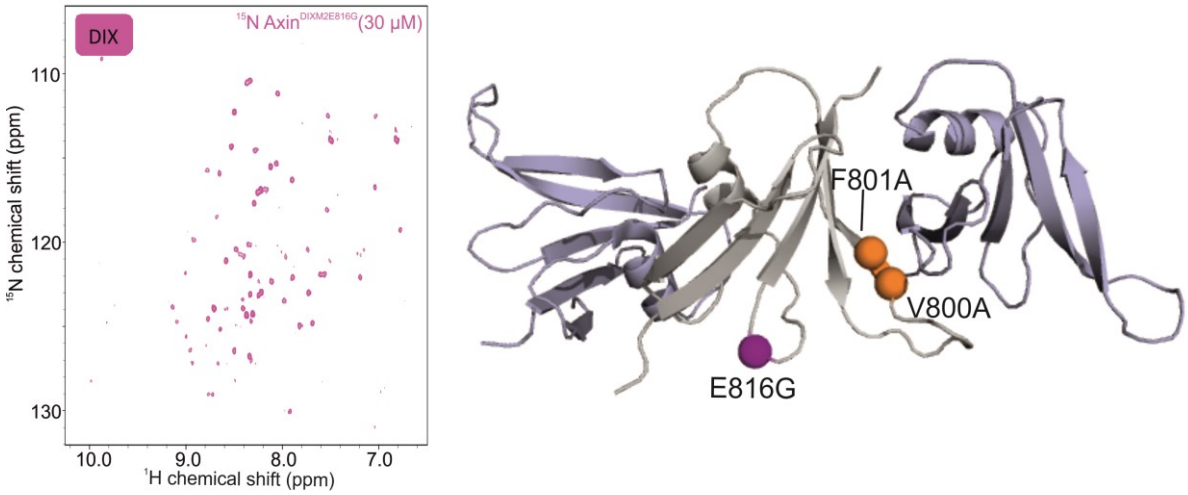

Figure 26: Axin-1^{DIXM2} with cancer mutation. 2D ^{1}H, ^{15}N HSQC NMR spectrum of ^{15}N Axin-1^{DIXM2} (V801A and F802A) with addition cancer mutation (E816G). RCSB PDB: 1WSP. Structure of Axin-1^{DIXM2E816G} (M2 mutations in orange and E816G mutation in magenta).

We titrated the Axin-1^{DIXM2E816G} to ^{15}N labelled Axin-1^{IDR} fragments and vice versa. In these experiments we confirmed that the interaction with the BSs still takes place in the cancer situation. (Fig. 27, 28).

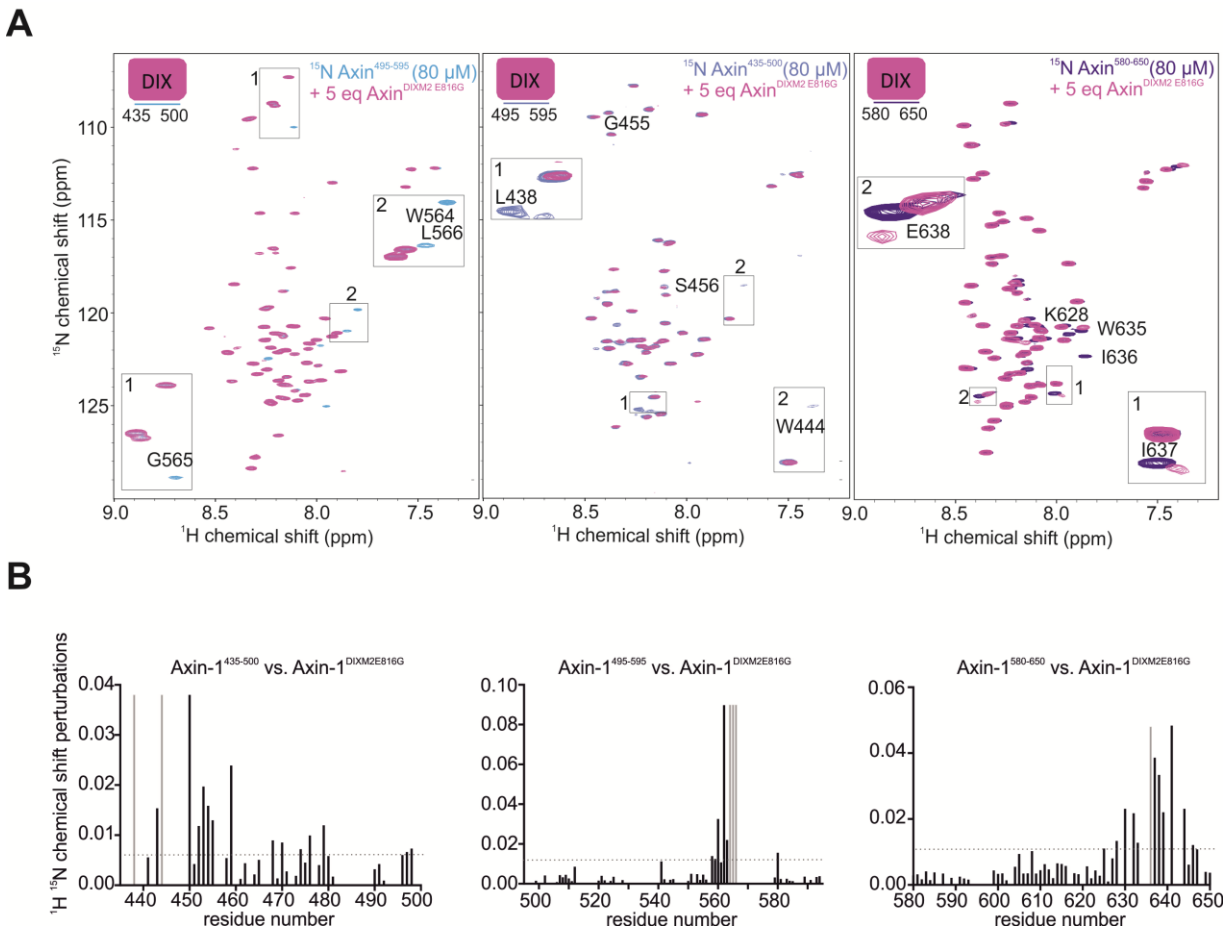

Figure 27: Axin-1^{DIXM2E816G} interaction with Axin-1^{IDR}. A. 2D ^{1}H, ^{15}N HSQC NMR spectra of ^{15}N Axin-1^{DIXM2} in absence (blue) or presence of non-labelled Axin-1^{DIXM2E816G} (magenta). Affected peaks within the binding region are indicated. B. Corresponding CSP plots of titration experiments are shown.

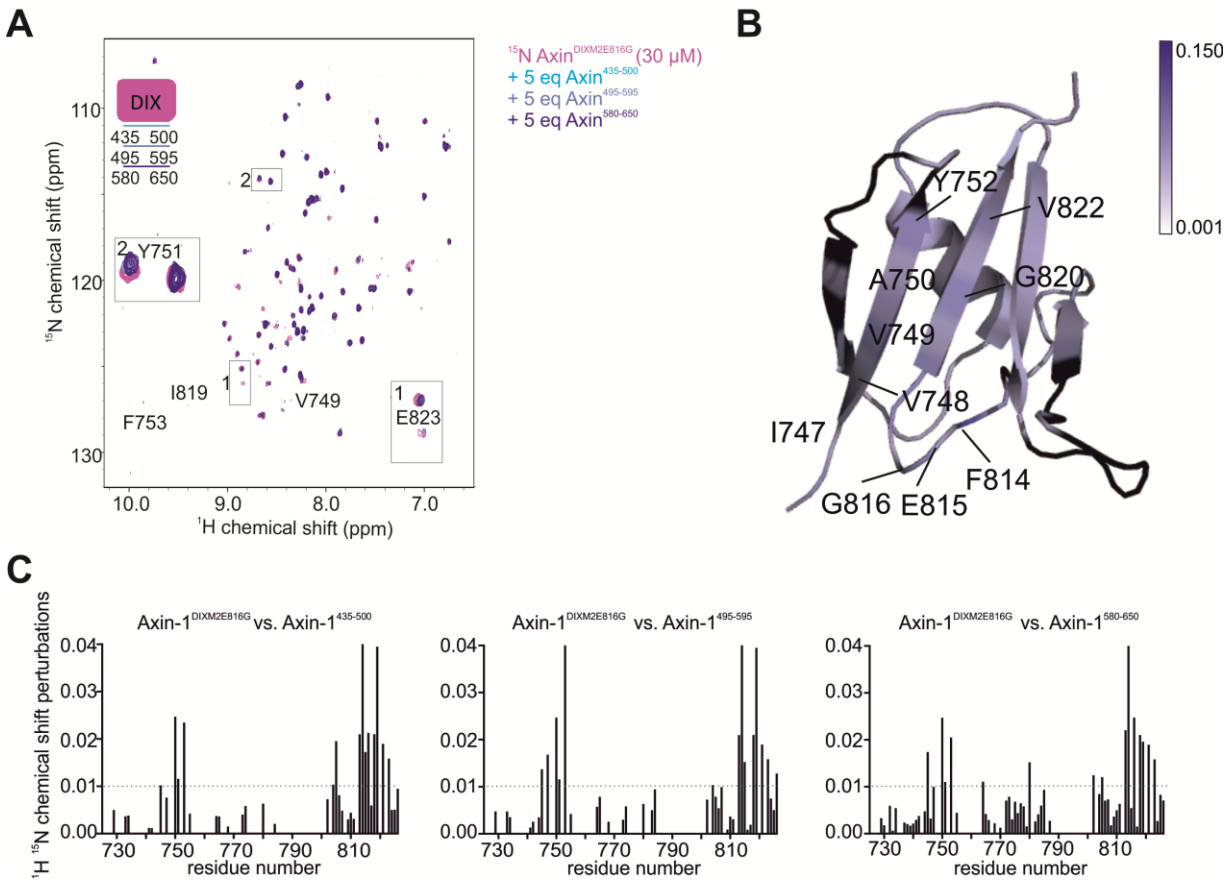

Figure 28: *In vitro* binding studies of Axin-1^{IDR} to Axin-1^{DIXM2E816G} A. 2D ^{1}H, ^{15}N HSQC NMR spectra of ^{15}N Axin-1^{DIXM2E816G} in absence (magenta) or presence (blue) of non-labelled Axin-1^{IDR}. Affected peaks within the binding region are indicated. B. Binding sites of Axin-1^{IDR} to Axin-1^{DIXM2E816G} colored by CSP values in structure of Axin-1^{DIX}. RCSB PDB: 1WSP. C. Corresponding CSP plots of titration experiments are shown.

In order to investigate, whether the interaction of the Axin-1^{DIX} cancer variant with Axin-1^{IDR} detected via NMR spectroscopy is in the same affinity range as in the wildtype situation, we used using fluorescence anisotropy. With this technique we aimed at detecting differences of the interactions of the cancer variant compared to the wildtype protein. Hereby Axin-1 synthetic peptides harboring the sequence of the BSs with a FITC label were titrated with a dilution series of Axin-1^{DIXM2} or Axin-1^{DIXM2E816G}. Interestingly, all three peptides indicated a similar affinity to Axin-1^{DIXM2}, but not to Axin-1^{DIXM2E816G}. Peptides harboring BS 1 and 3 revealed decreased affinities to the cancer mutant, whereas BS2 binds with comparable affinity to Axin-1^{DIXM2} and Axin-1^{DIXM2E816G}. (Fig. 29)

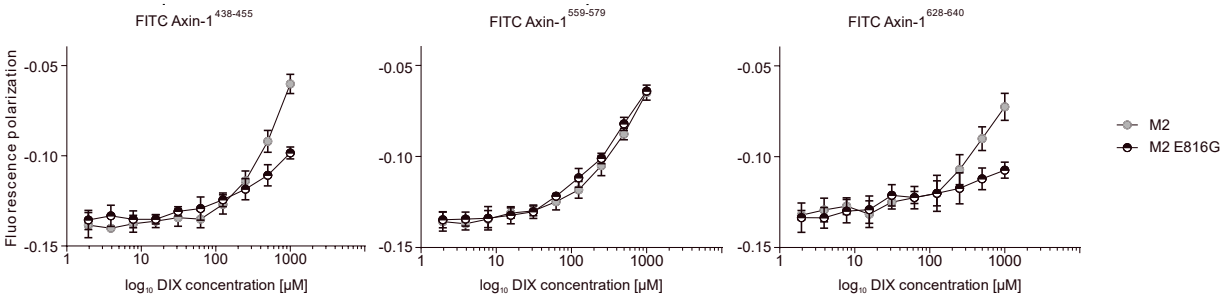

Figure 29: Fluorescence polarization for FITC-tagged Axin-1 peptides of the BS. Binding data for Axin-1$^{438-455}$, Axin-1$^{559-471}$ and Axin-1$^{628-640}$ to increasing concentrations of Axin-1^{DIXM2}/Axin-1^{DIXM2E816G}. Data are represented as mean ± SD of 6 independent experiments.

Axin-1 performs phase separation

Since phase separation is a very prominent topic in biology, it is important to confirm that Axin-1 *puncta* are a manifestation of liquid demixing, according to its defined criteria. With FRAP experiments it was already clear that the Axin-1 *puncta* are highly dynamic and exchange with the environment.(35) In addition to this knowledge in literature, we used electron microscopy as a clean system to see that Axin-1 alone is able to perform phase separation *in vitro*. Indeed, recombinant wildtype Axin-1 full length formed demixed biocondensates as seen by TEM. (Fig. 30). When using the Axin-1^{E816G} cancer variant, we could still observe formation of a few *puncta*, however, most of the protein was seen more as a flat aggregate on the grids. (Fig. 30) The restored *puncta* constructs from cell based assays were also used for TEM, where we observed a restoration of Axin-1 *puncta* formation.(Fig. 30)

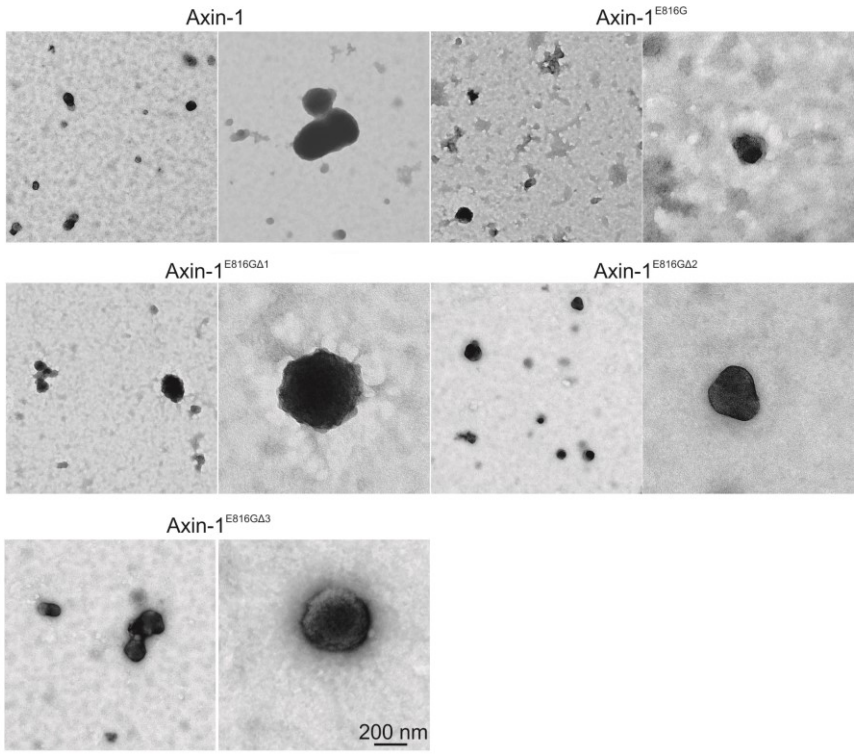

Figure 30: Electron microscopy of Axin-1 variants. TEM images were recorded using a JEOL JEM 1400-plus electron microscope of recombinant Axin-1 after negative staining.

In addition to that, differential interference contrast (DIC) microscopy was an alternative approach in order to observe phase separation *in vitro*. The main advantage of this technique is, that the recombinant protein remains in solution. Therefore it is a better suited method in order to detect liquid demixing than TEM, where the recombinant protein is dried on a grid. Hence, we used it as an approach to investigate differences in phase separation of Axin-1 variants. Hereby, we observed phase separation in Axin-1 and the absence of phase separated protein assemblies in Axin-1^{E816}, which goes in line with the cell biology data. (Fig. 31, Fig. 25) When deleting BS in Axin-1^{E816G}, phase separation was also restored *in vitro*. (Fig. 31)

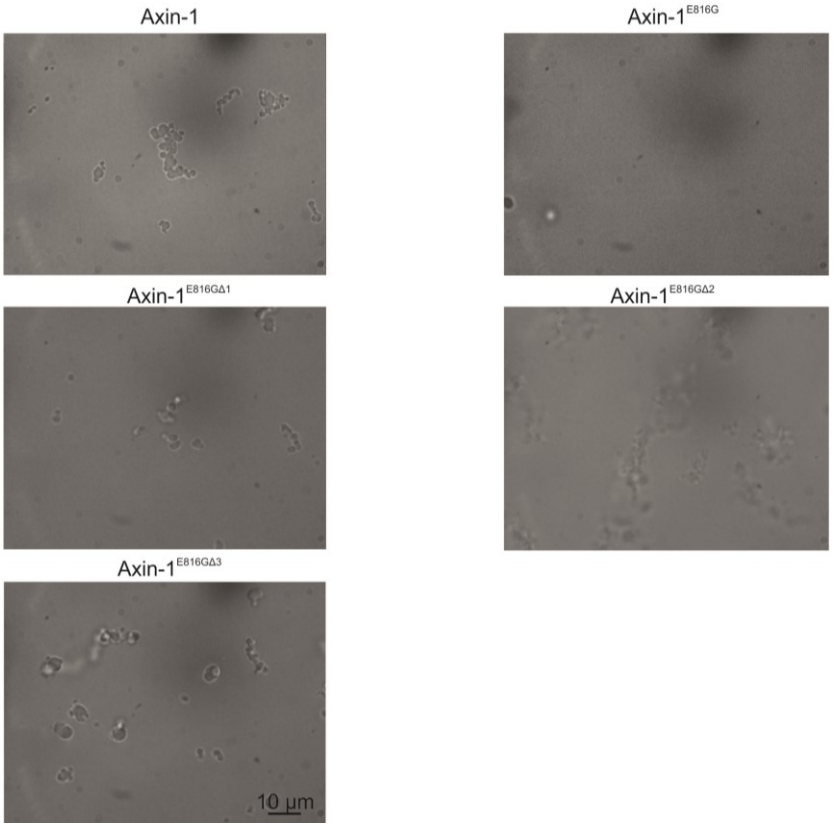

Figure 31: DIC microscopy of Axin-1. DIC images were recorded using an Observer D1 microscope for recombinant Axin-1 constructs.

Finally, we performed turbidity analysis where the optical density of the protein solution of recombinant Axin-1 ($OD_{620\ nm}$) is used as a measure of phase separation. The turbidity of a protein solution containing increasing concentration (1-80 µM) of recombinant Axin-1 full length was used as a method in order to confirm that Axin-1 is able to phase separate *in vitro* in a concentration dependent manner. (Fig. 32 A) Hereby, an increase in absorbance at 620 nm was observed at higher protein concentrations, indicating that Axin-1 separates from the surrounding buffer milieu. When using Axin-1^{E816G} for those experiments, a slight increase in turbidity was observed at high concentrations (~ 80 µM), but highly decreased compared to Axin-1 wildtype protein. Those data support the cell biology data that indicate that Axin-1^{E816G} shows a reduced phase separation in cells. (Fig. 7)

OD_{600} measurements of recombinant Axin-1 full-length were also used in order to test whether Axin-1 performs phase separation without need of a co-factor. Therefore Axin-1 was used at a concentration of 75 µM, with increasing concentrations of ß-catenin$^{141-304}$. In the condition with 0 µM ß-catenin$^{141-304}$, there is a clear difference in absorbance of buffer and Axin-1, which proves that Axin-1 is at this concentration phase separated. When increasing the ß-catenin concentrations in buffer or in the Axin-1 solution, slight variations due to the low absorbance level are detected, however, there is always a higher absorbance in Axin-1, which does not significantly increase or decrease, not even with three fold molar excess of ß-catenin$^{141-304}$. (Fig. 32 B)

Finally, turbidity experiments were also used to test if *puncta* restoration in cells (Fig. 25) can also be observed *in vitro*. When comparing the absorbance at 620 nm of Axin-1^{E816G} and Axin-$1^{E816G\Delta1}$, Axin-$1^{E816G\Delta2}$ and Axin-$1^{E816G\Delta3}$, there is a clear increase in turbidity of Axin-$1^{E816G\Delta1}$ observed, which proves restoration of phase separation when deleting this BS. For Axin-$1^{E816G\Delta1}$ and Axin-$1^{E816G\Delta2}$ the difference in phase separation was not as clear, however, when focusing on lower protein concentrations (0-20 µM), the increase in turbidity is much higher than for Axin-1^{E816G}. (Fig. 32 C) Assuming that protein concentrations in cells will be more likely in the nanomolar to low micromolar range, those differences in initiation of phase separation might be enough in order to restore *puncta* formation in cells.

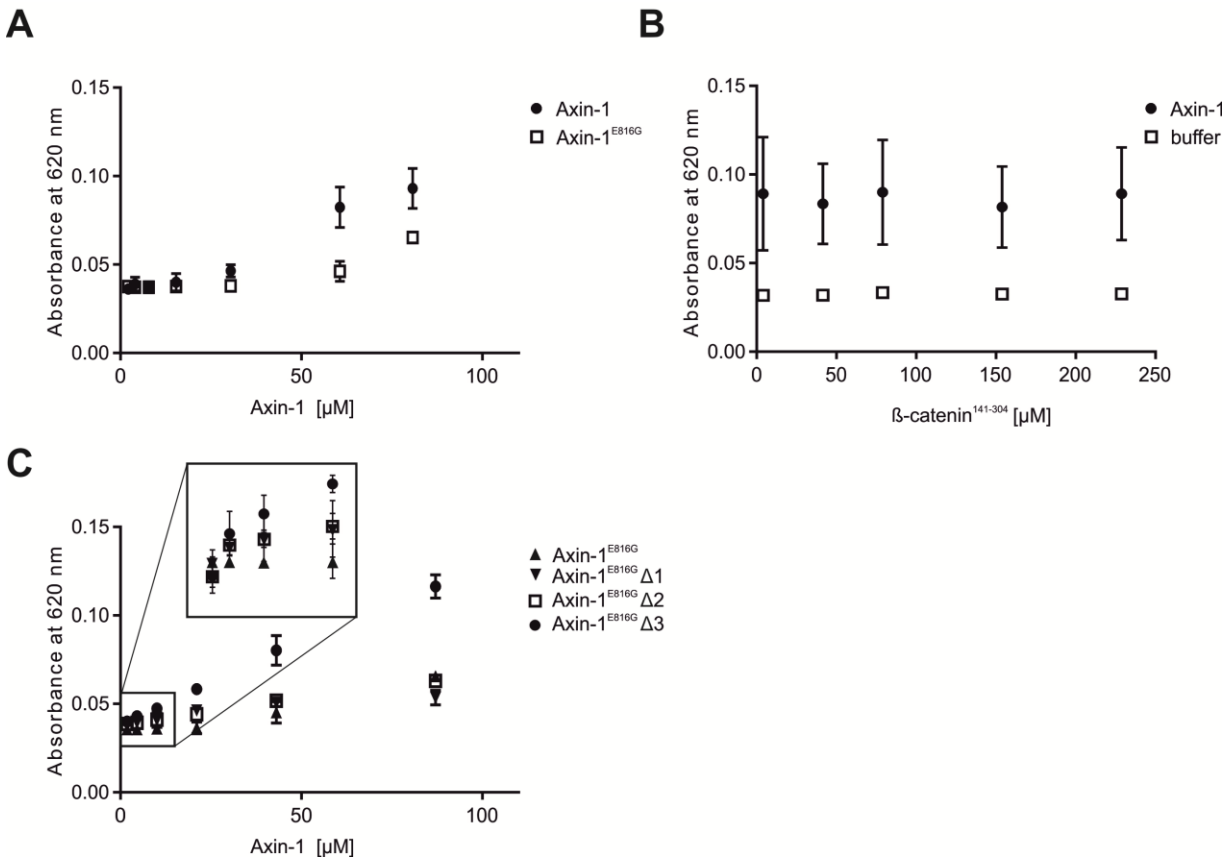

Figure 32: Turbidity assay. A. Determination of absorbance at 620 nm of the recombinant Axin-1 protein. Experiment was performed in triplicates and data are represented as mean ± SD. B. Determination of absorbance at 620 nm of the recombinant Axin-1 protein (75 µM) in presence of increasing ß-catenin$^{141-304}$ concentrations. Experiment was performed in triplicates and data are represented as mean ± SD. C. Determination of absorbance at 620 nm of the recombinant Axin-1 protein variants. Experiment was performed in triplicates and data are represented as mean ± SD.

A

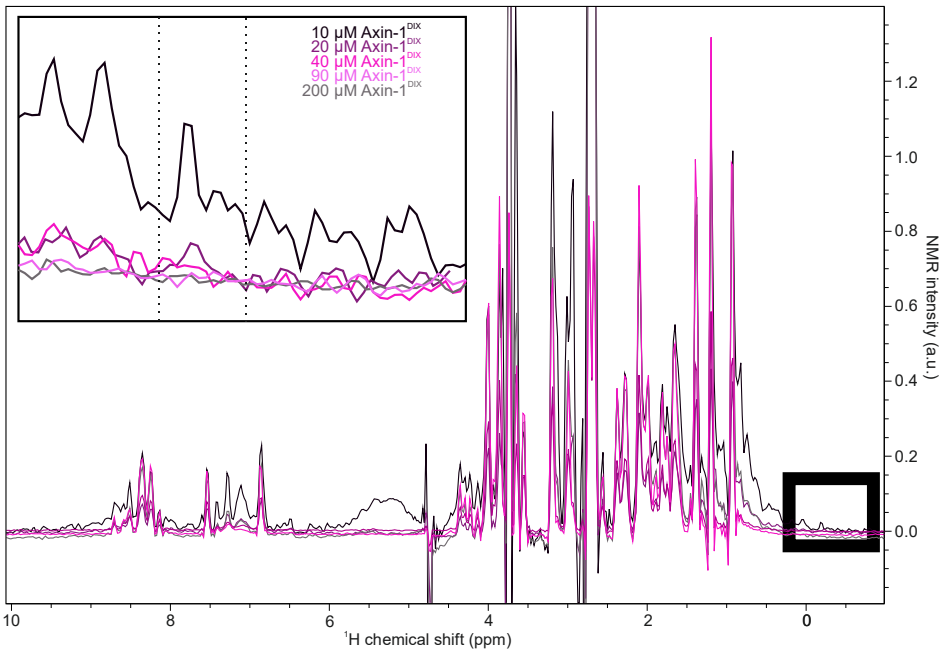

B

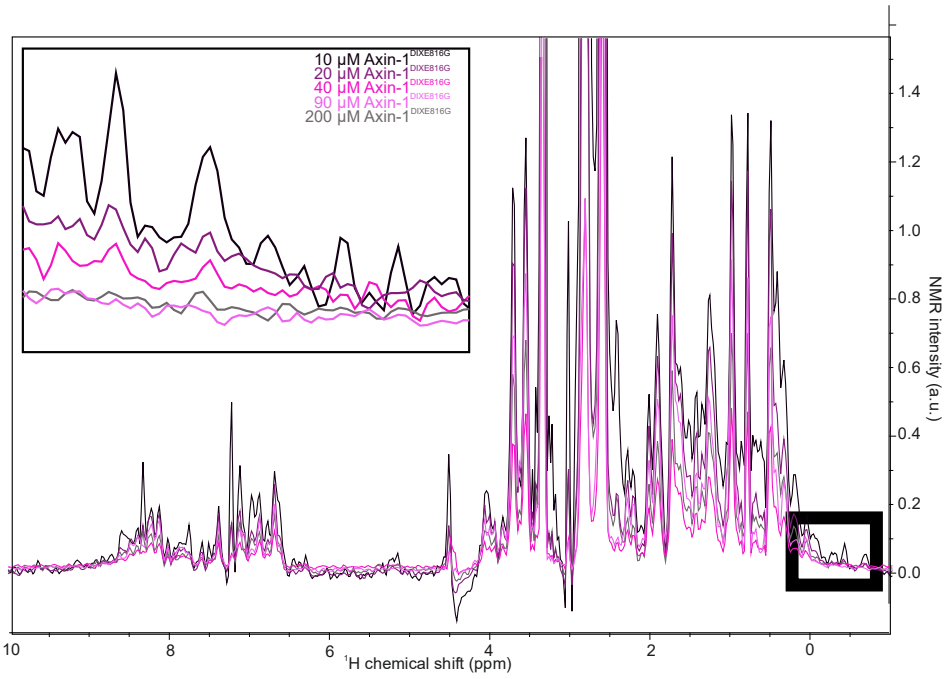

Supplementary figure 1: Axin-1^{DIX} dilution series. A. Overlay of ^{1}H 1D zggpw5 experiments of Axin-1^{DIX} at different concentrations. Zoom-in for methyl groups around 0 ppm is shown. B. Overlay of ^{1}H 1D zggpw5 experiments of Axin-1^{DIXE816G} at different concentrations. Zoom-in for methyl groups around 0 ppm is shown.

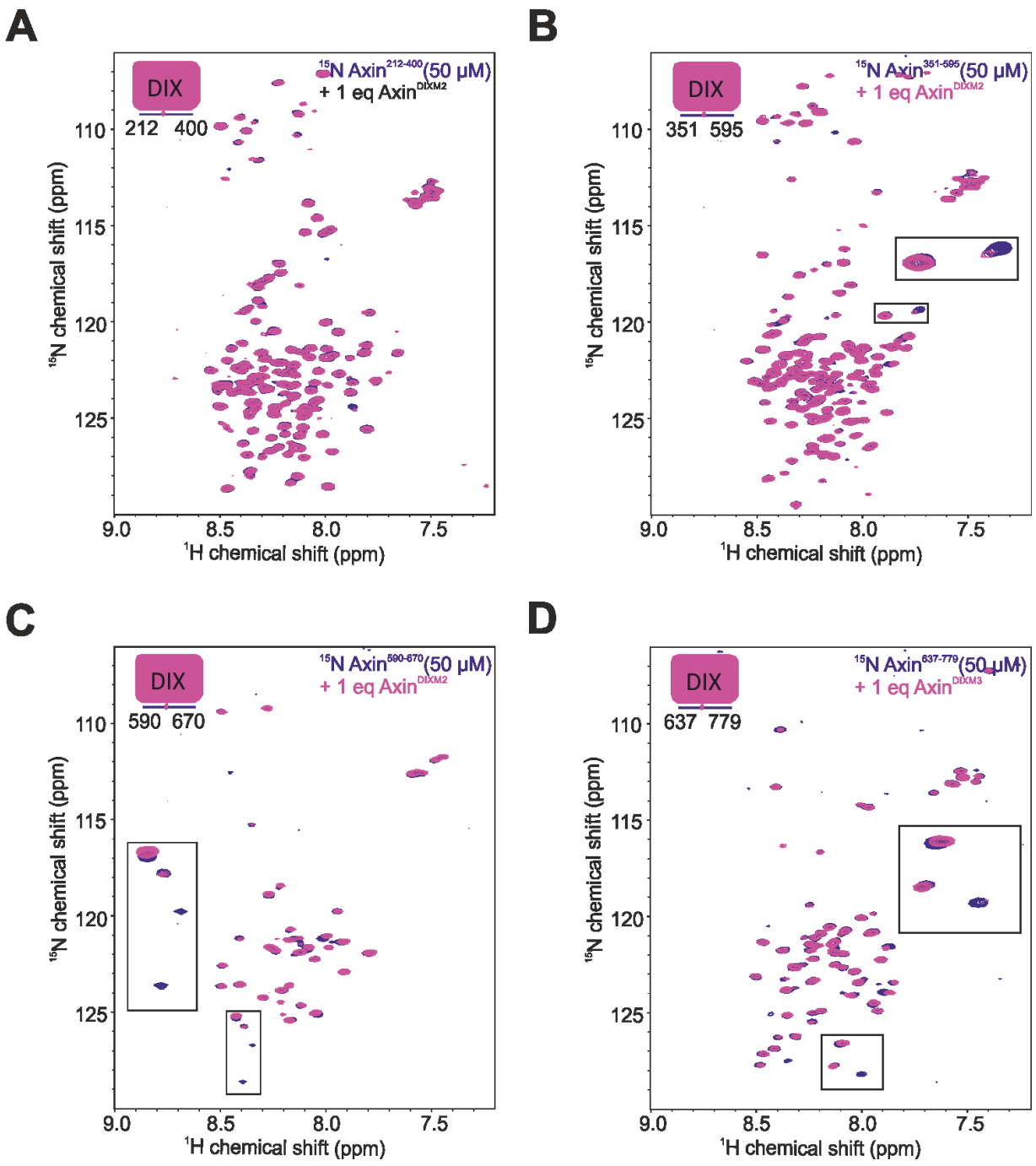

Supplementary figure 2: Screening for Axin-1^{DIXM2} binding events on Axin-1^{IDR}. 2D ^{1}H, ^{15}N HSQC NMR spectra of A. ^{15}N Axin-1$^{212-400}$, B. ^{15}N Axin-1$^{351-595}$, C. ^{15}N Axin-1$^{590-670}$ and D. ^{15}N Axin-1$^{637-779}$ in absence (blue) or presence (magenta) of Axin-1^{DIXM2}.

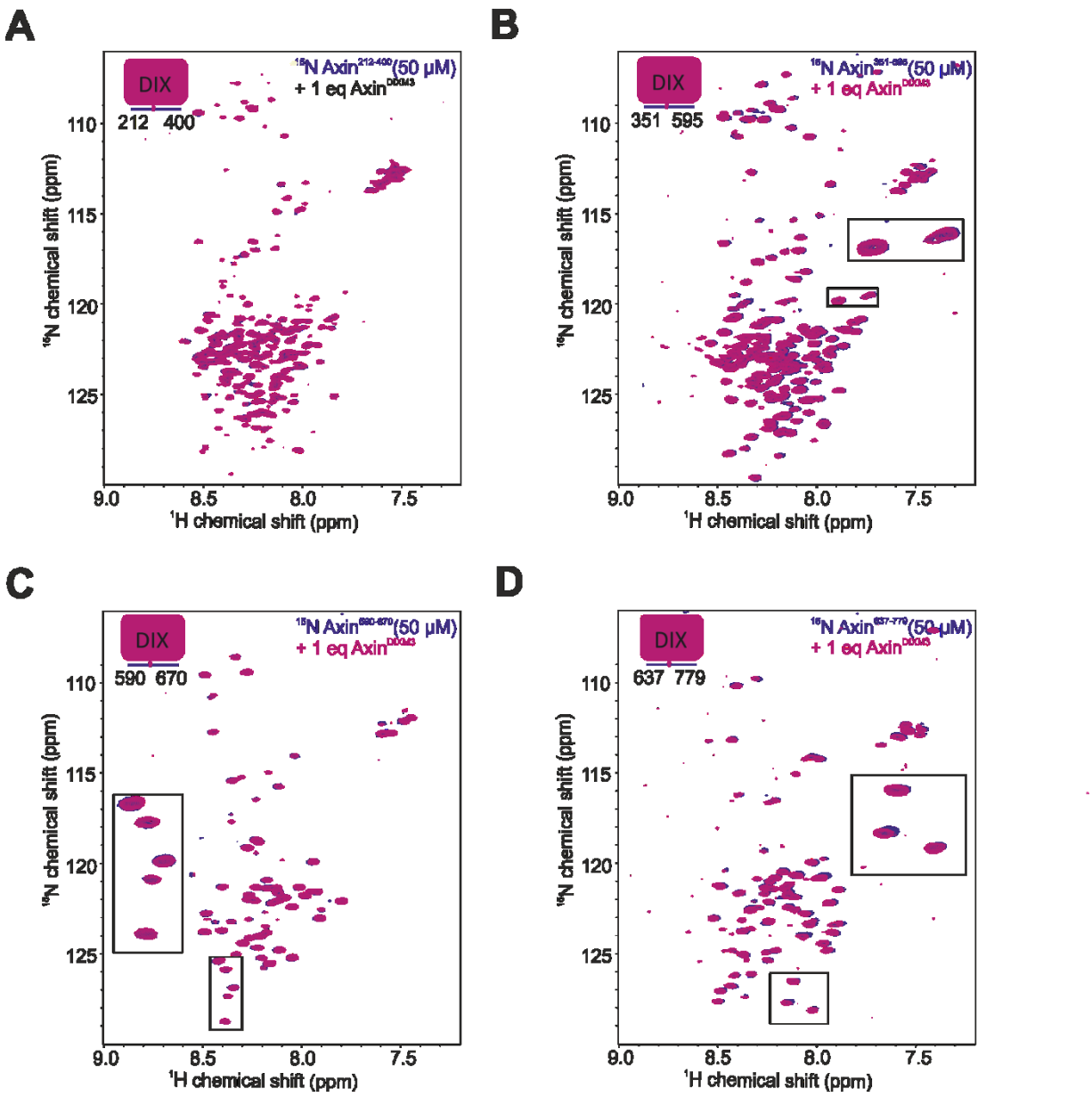

Supplementary figure 3: Screening for Axin-1^{DIXM3} binding events on Axin-1^{IDR}. 2D ^{1}H, ^{15}N HSQC NMR spectra of A. ^{15}N Axin-1$^{212-400}$, B. ^{15}N Axin-1$^{351-595}$, C. ^{15}N Axin-1$^{590-670}$ and D. ^{15}N Axin-1$^{637-779}$ in absence (blue) or presence (magenta) of Axin-1^{DIXM3}.

A

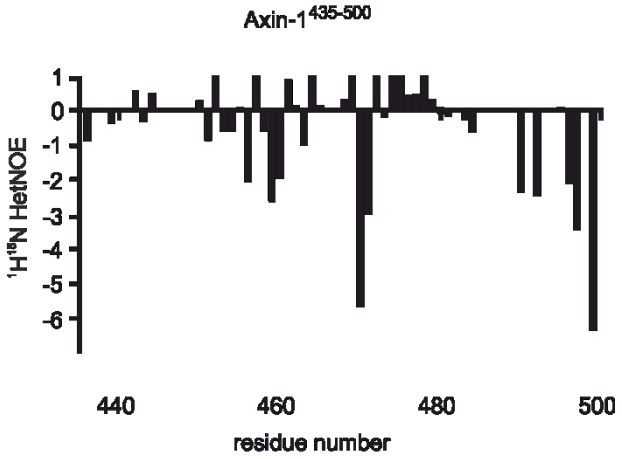

B

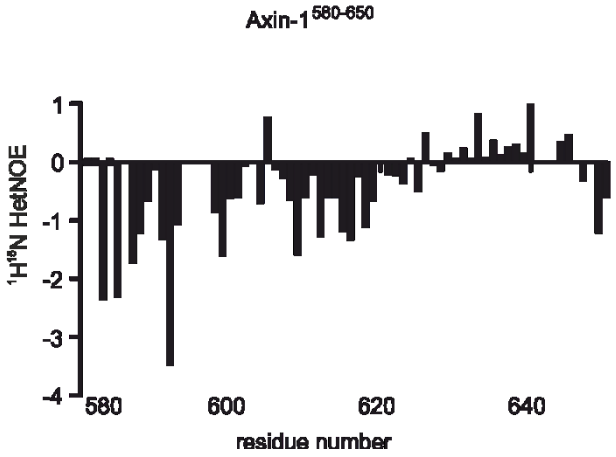

Supplementary Figure 4: Relaxation data

HetNOE data for Axin-1$^{435-500}$ and Axin-1$^{580-650}$.

Results – Findings Part II

JRES as homo-nuclear decoupling experiment

Standard 1D ^{1}H NMR experiments used for metabolomics research include Carr-Purcell-Meiboom-Gill sequences (CPMG) or nuclear overhauser enhancement spectroscopy (noesy). In those experiments, each non-exchangeable proton gives rise to one signal in the spectrum. Therefore, a typical urine sample harboring hundreds of different metabolites, gives rise to one or several peaks/multiplets for each metabolite. Therefore it is obvious, that there is a severe signal overlap observed in such spectral data.(Fig. 33, grey spectrum) By using JRES experiments, a second dimension is introduced, which separates the chemical shift in the first dimension from the scalar coupling in the second dimension. This is a method to highly reduce spectral complexity. In order to prove whether JRES experiments enable the reduction of this signal overlap which is commonly observed in ^{1}H CPMG experiments, spectral data of those two experiment types were compared (Fig. 33). By comparing the experiments, it is obvious that the signatures of the urine spectrum are highly simplified in the JRES experiment (black), which makes identification and quantification of compounds in the complex matrix more reliable.

With those experiments we could show, that JRES experiments are a useful tool in order to simplify spectral information, which is an essential step for the analysis of complex matrices such as urine.(6)

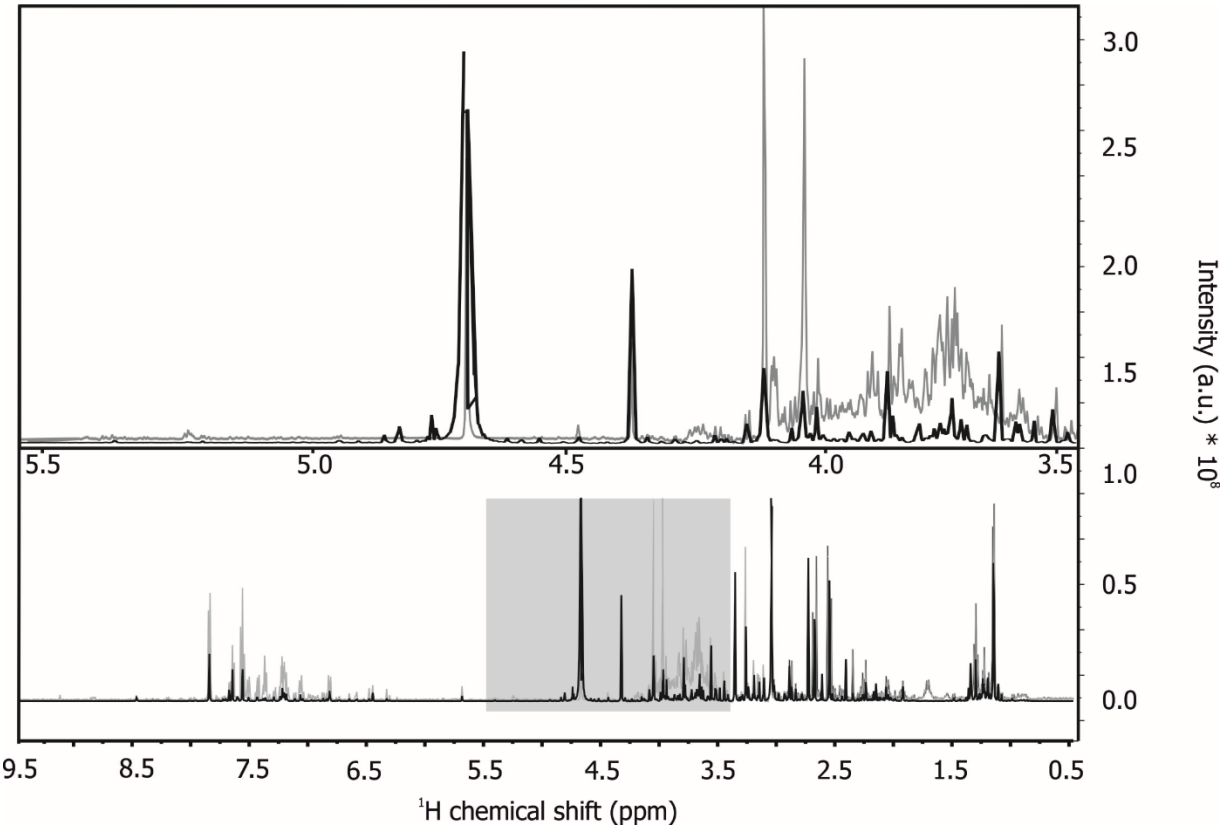

Figure 33: Comparison of CPMG and JRES. Spectral comparison of a ^{1}H 1D CPMG experiment (in grey) overlaid on the projection of a JRES experiment (in black) of a human biofluid sample (urine) after sugar intake. JRES as well as CPMG experiments show proton signals of all compounds harboring non-exchangeable protons. By resolving the J-coupling in the indirect dimension, and by acquiring a positive projection, spectral signatures can be simplified. Data are reprinted from publication (6) in Scientific Reports.

The next important step was to determine the spectral signatures of lactulose, mannitol and sucrose, since those metabolites of interest have to be identified in the complex urine matrix. Therefore, standard samples of carbohydrates in NMR metabolomics buffer were prepared and CPMG, noesy and JRES experiments were recorded. Each sugar provided a unique spectral signature in NMR experiments.(Suppl. Fig. 5) (6)

Apart from JRES experiments, there are also other homo-nuclear decoupling experiments available, which simplify one-dimensional NMR experiments. Examples include broadband homo-nuclear decoupled experiments/^{1}H pure shift experiments. Those experiments provide also clearly reduced complexity in spectral data, however, they suffer from low sensitivity and therefore long measurement times are needed (Fig. 34). Hereby, four hours of measurement time were needed, in order to clearly detect signals of a 1 mM sucrose sample. Since we were looking for a technique that is useful for clinical applications and for screening of many samples, the measurement time is crucial. Therefore, JRES experiments are the preferred method for homo-nuclear decoupling of spectral signatures urine samples.(6)

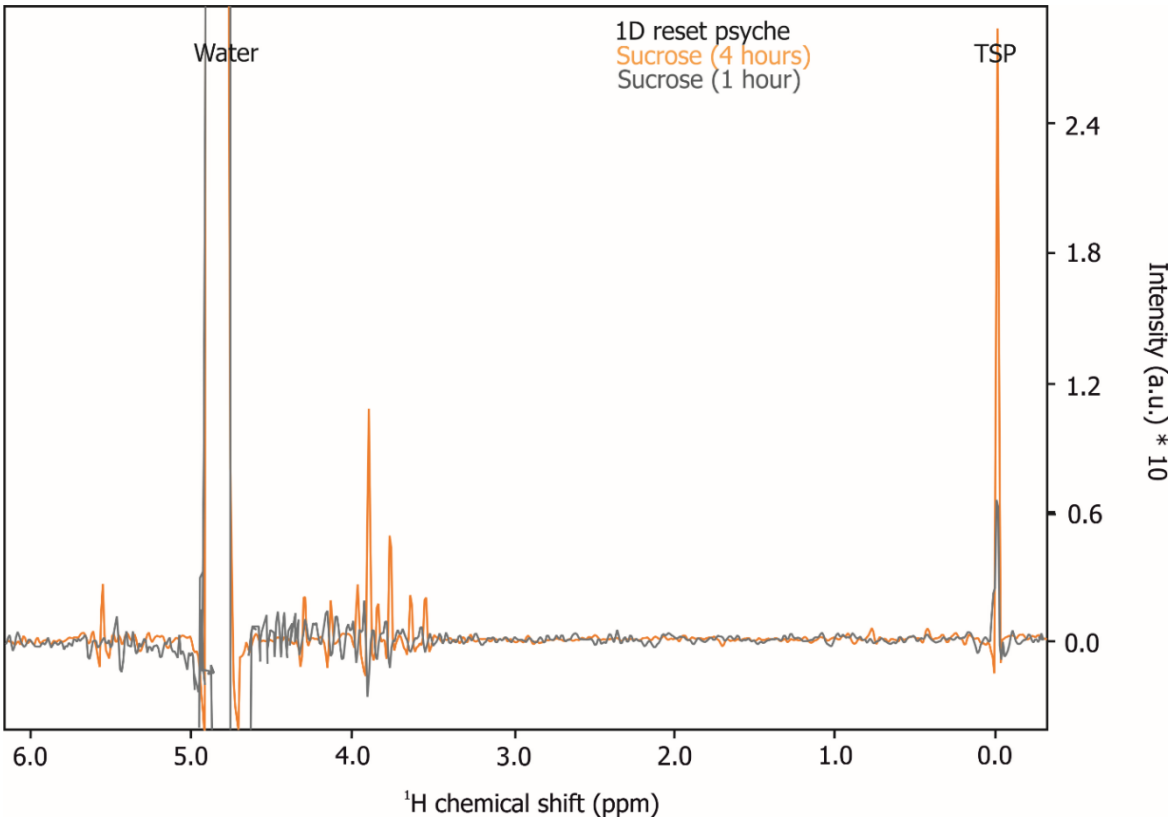

Figure 34: Psyche experiment for decoupling. Representation of two homo-nuclear decoupled psyche experiment with either one (grey) or four hours (orange) of measurement time for a 1 mM sucrose standard. Data are reprinted from publication (6) in Scientific Reports.

Identification of reference compounds in a urine sample

In 1D ^{1}H NMR experiments, most metabolites comprise several signals due to several chemically different protons. In urine samples, there are hundreds of different metabolites present, which give rise to even more different signals in the NMR spectrum. Therefore, it is essential that the assignment of peaks in the spectrum is accurate in order to enable reliable detection of metabolites and their quantifications. We made use of 2D ^{1}H DIPSI experiments, which correlate nuclei due to their scalar coupling. Those experiments provide information about correlation within a spin system, which enables the identification of discrete building blocks in a molecule. For a urine sample after carbohydrate intake 2D ^{1}H DIPSI experiments were recorded and overlaid with 2D ^{1}H DIPSI experiments for reference carbohydrate substances. Due to presence of spin systems of lactulose, mannitol and sucrose, we could confirm the presence of all the carbohydrates in the urine sample.(Fig. 35 A-C)(6)

However, 2D ^{1}H DIPSI experiments require long measurement times and are therefore not preferable for a high-throughput application, we also confirmed the sugar identification in JRES experiments using a spike-in approach. Those experiments were very important, since we aimed at direct quantification of carbohydrates from JRES experiments, therefore, it is necessary, that the identification of sugar peaks in the one dimensional projects of JRES experiments is highly reliable. Hereby, defined concentrations of carbohydrates (50 µM) were added to the urine sample and the sample was re-measured. When comparing the two spectral data before and after addition of carbohydrates, identification of the additional peaks due to the spike-in was feasible and indicated the exact position of the sugar signals in a complex matrix like urine in JRES projections (Fig.36).(6)

Those experiments proved that NMR spectroscopy is a reliable analytical tool, which, due to unique spectral signatures for each metabolite, enables robust and reliable identification of metabolites of interest.(6)

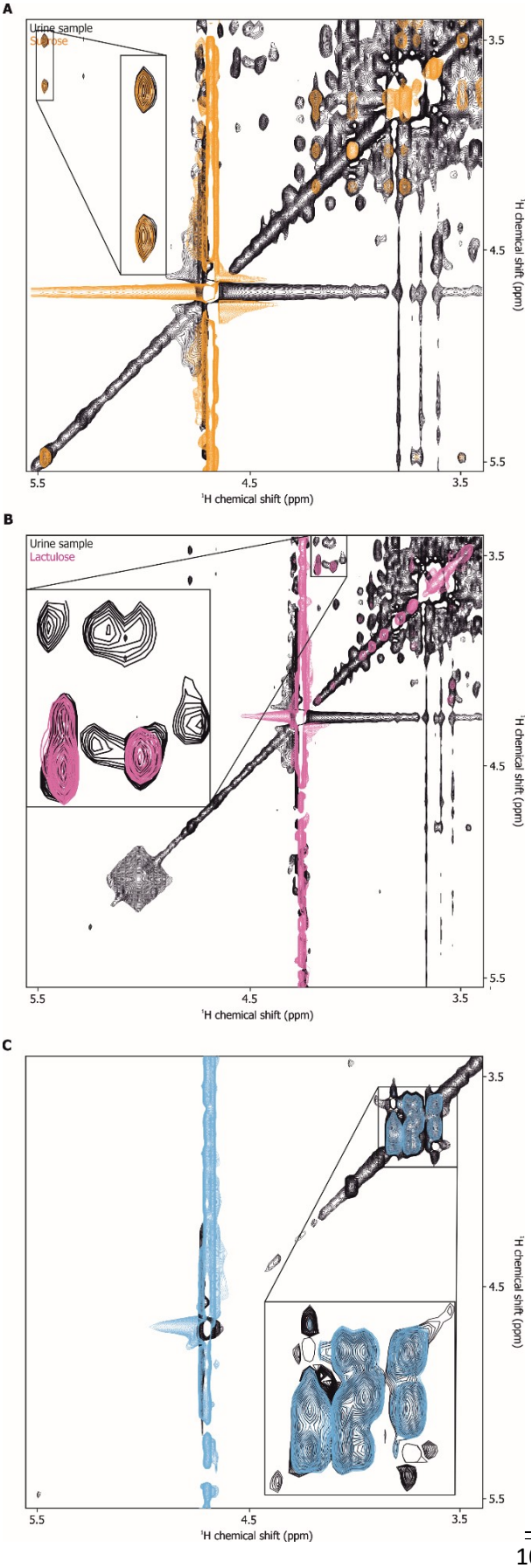

Figure 35: DIPSI experiments for carbohydrate identification. A. Comparison of 2D ^{1}H DIPSI experiments from a human biofluid (urine) sample (black) and a sucrose standard (orange). B. Comparison of 2D ^{1}H DIPSI experiments from a human biofluid (urine) sample (black) and a lactulose standard (magenta). C. Comparison of 2D ^{1}H DIPSI experiments from a human biofluid (urine) sample (black) and a mannitol standard (light blue). Data are reprinted from publication (6) in Scientific Reports.

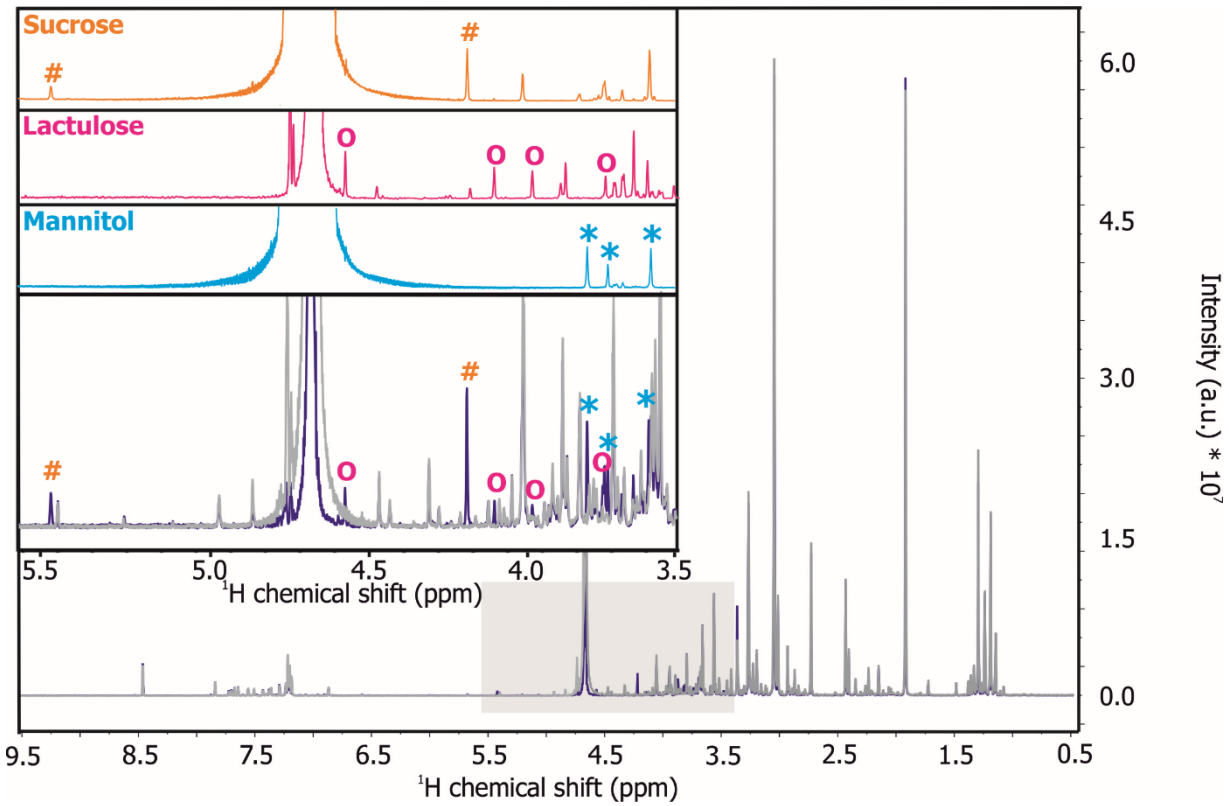

Figure 36: Sugar spike-in experiments in human urine samples. Positive adsorptive projections of ^{1}H J-resolved 2D experiments of 100 µM reference compounds sucrose (orange), lactulose (magenta), and mannitol (light blue). Corresponding resonances of these carbohydrates in a human urine sample before (grey) and after 50 µM sugar spike-in (marine blue) are indicated with orange hash (sucrose), magenta circle (lactulose) or light blue asterisks (mannitol). Data are reprinted from publication (6) in Scientific Reports.

Quantification of carbohydrates in urine

With those experiments, the setup for determination of sugar concentrations in patient's samples was established. We were able to identify signals for carbohydrates in urine in a reproducible manner. Therefore, we started to apply this experimental setup on patient's samples obtained from the group of Vanessa Stadlbauer-Köllner. Hereby, carbohydrate solutions were administered to patients and urine samples were collected after sugar intake. We used these samples without any extraction steps, mixed them with NMR metabolomics buffer for JRES experiments and analyzed the spectral data for quantification.(6)

Firstly, we used an untargeted approach in order to see whether we can distinguish between high and low sugar samples using a PCA. (Fig. 37). Hereby, spectral data was imported into Matlab® vR2014a and multivariate statistical analysis was performed. This analysis indicated only a clustering of samples harboring high concentrations of mannitol. This indicates, that high mannitol concentrations mask differences in other metabolites/carbohydrates. However, extremely high concentrations of mannitol are expected in samples from patients suffering from increased gastric and intestinal permeability.(6)

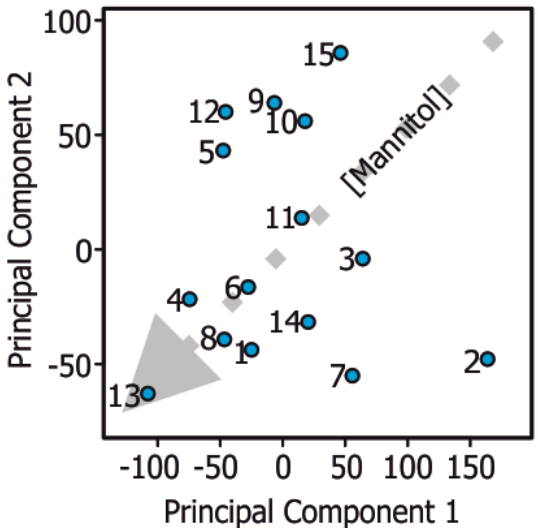

Figure 37: PCA of urine samples. Clustering of urine samples after sugar intake is monitored using PCA. Data are reprinted from publication (6) in Scientific Reports.

Spectral data from the same patients' samples have then been used in order to quantify carbohydrates in the samples. Hereby, an approach using Chenomx NMR Suite Professional 8.2 was used, where single spectra were used for quantification in the software (Fig. 38 A). We also tested a batch processing approach using MestreNova 11.0, which revealed similar concentrations and suggest the applicability for high-throughput data analysis. (Fig. 38 B)(6)

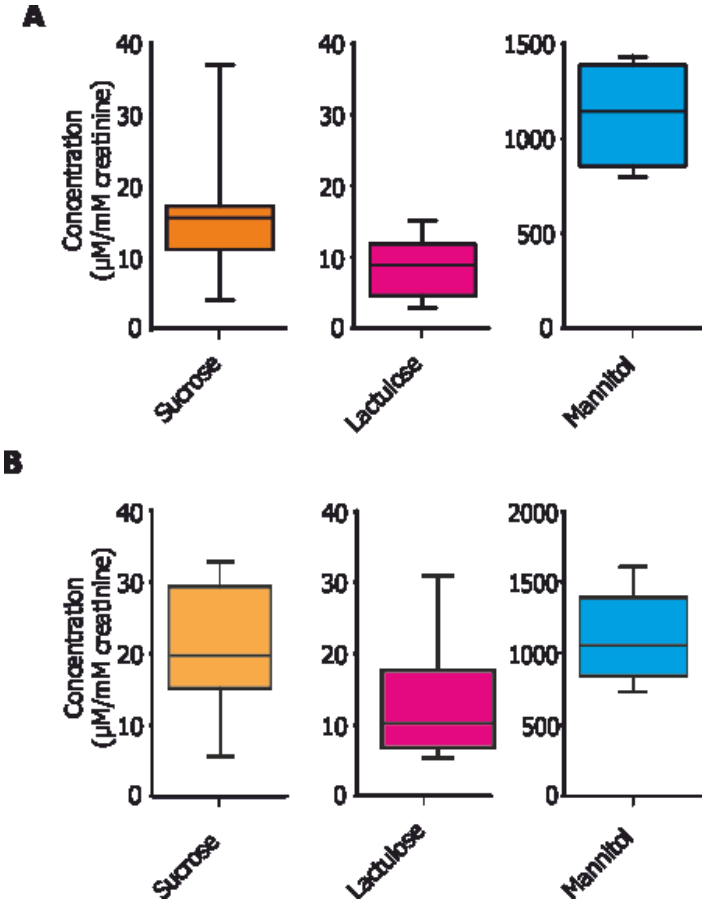

Figure 38: Quantifications of sugar solutions in urine. A. Carbohydrate absolute quantification in human urine using Chenomx NMR Suite Professional 8.2 software tool. B. Carbohydrate absolute quantification using batch processing approach in MestreNova 11.0 software tool. Data are reprinted from publication (6) in Scientific Reports.

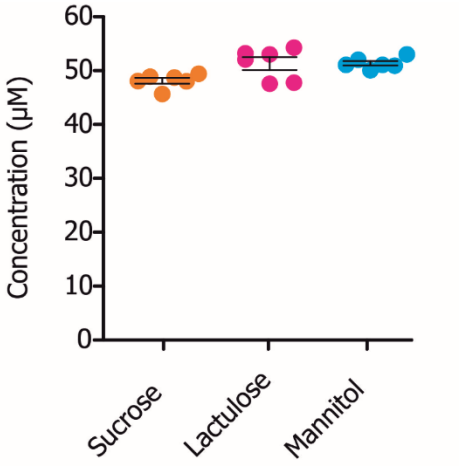

Figure 39: Accuracy of NMR experiments. Data are represented as mean ± SD of 5 independent experiments. Spike-in of carbohydrates (sucrose, lactulose, and mannitol) in human urine and subsequent quantification. Data are reprinted from publication (6) in Scientific Reports.

Since urine is a very complex matrix, and despite the simplification of spectral data using JRES experiments, there is still signal overlap observable. Therefore, it is important that the accuracy of quantifications is analyzed. In order to do that, spike-in experiments have been performed. Hereby, urine samples were spiked with 50 µM of sucrose, lactulose or mannitol, and increase of sugar concentration was determined.(Fig. 39) Those data suggest, that NMR-based quantification of carbohydrates is highly reproducible and therefore suitable for clinical applications.(6)

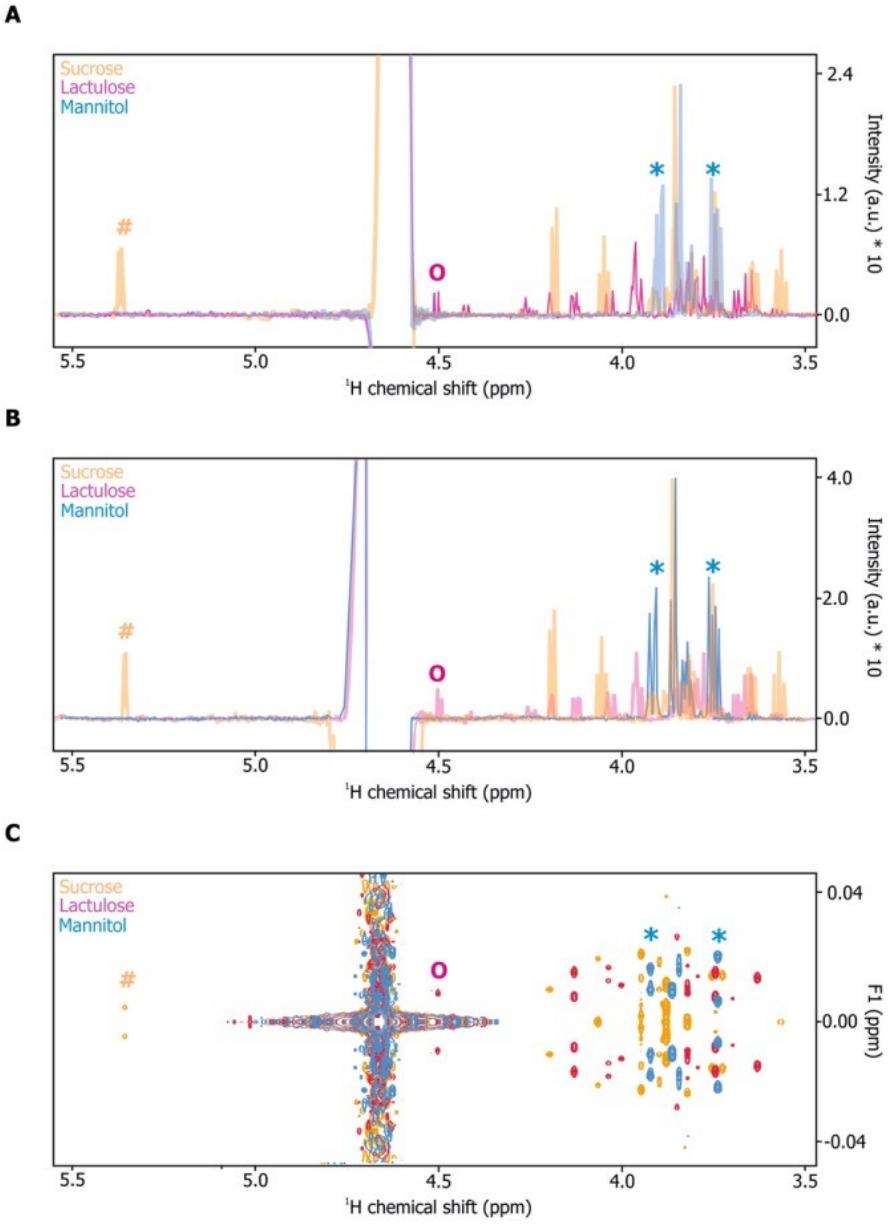

Supplementary figure 5: NMR experiments of reference sugar standard samples. A. Comparison of ^{1}H 1D CPMG experiments of 100 µM solutions of sucrose (orange), lactulose (magenta) and mannitol (light blue). B. Comparison of ^{1}H 1D NOESY experiments of 100 µM solutions of sucrose (orange), lactulose (magenta) and mannitol (light blue). C. Comparison of ^{1}H 2D J-resolved experiments of 100 µM solutions of sucrose (orange), lactulose (magenta) and mannitol (light blue). Characteristic signals of the different standards are indicated by orange hash (sucrose), magenta circle (lactulose) or light blue asterisks (mannitol). Data are reprinted from publication (6) in Scientific Reports.

Discussion Part I

Axin-1 and cancer

The importance of Wnt signaling in cancer has already been described for many components of the pathway. Those components involve mainly Axin-1, APC and ß-catenin. In APC cancer mutations include mainly truncations in the multiple cluster region, thus resulting in an inactive ß-catenin destruction complex due to the loss of Axin-1 binding sites in APC.(146) In contrast, Axin-1 is mainly associated with missense mutations throughout the sequence leading to the exchange of one single amino acid.(142)

In our study, we focused on one mutation within Axin-1^{DIX}, E816G, which has already been detected in colorectal cancer patients.(141, 142) This cancer mutation showed, upon overexpression in HeLa cells, a disrupted phase separation, as well as pathway activation compared to the wildtype protein (Fig. 7). We hypothesize that this is a general concept for LLPS in cancer: phase separated protein assemblies are important complexes, which perform essential functions for cellular functions. Within cells, Axin-1 will use a combination of inter-molecular interactions via Axin-1^{DIX}/Axin-1^{DIX} oligomerization but also Axin-1^{IDR}/Axin-1^{DIX} interaction, but also a combination of intra-molecular interactions of Axin-1^{DIX}/Axin-1^{IDR}. All those interactions will result in macromolecular protein assemblies, seen as Axin-1 *puncta* or phase separated condensates in cells. (Fig. 40)

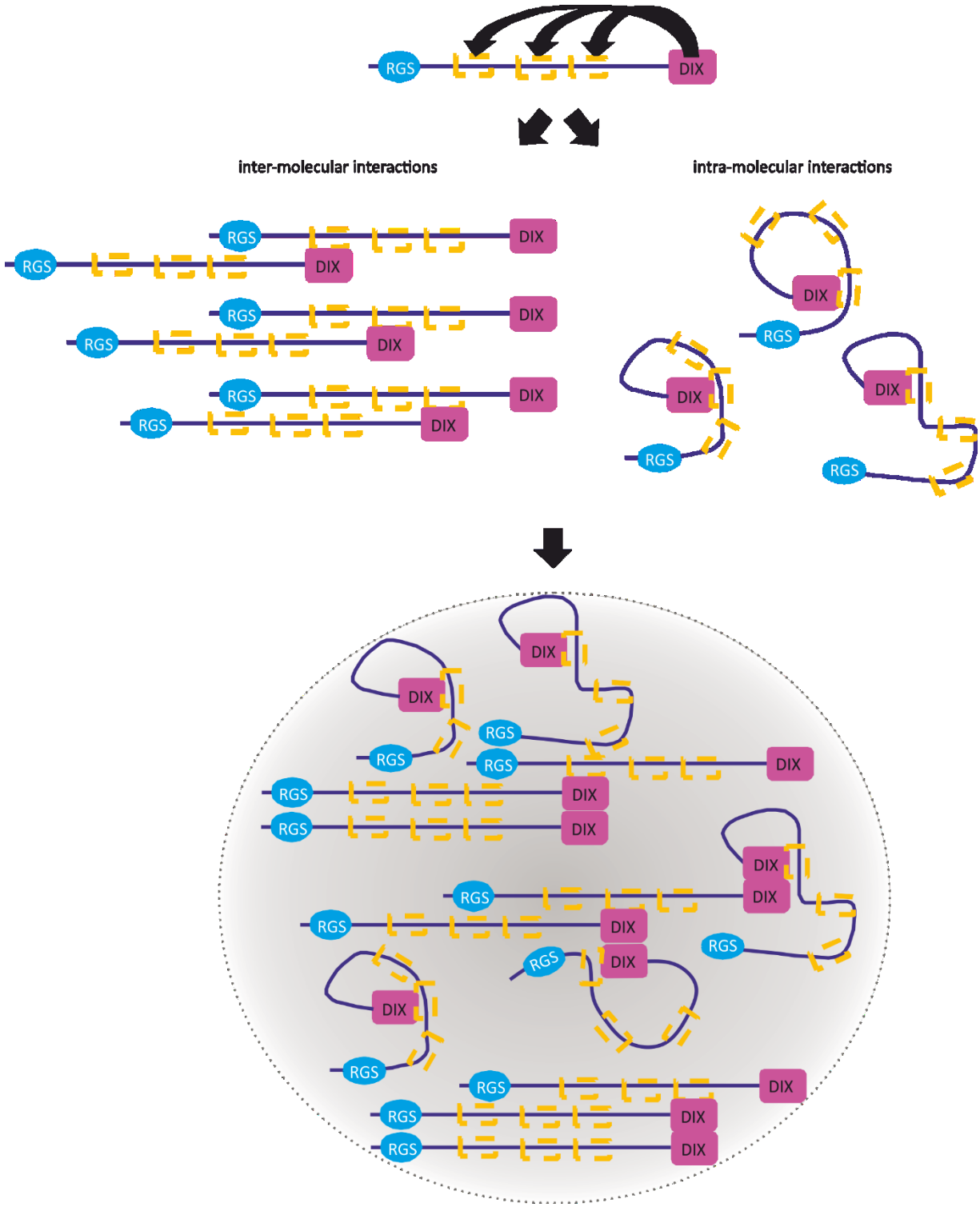

Figure 40: Model for Axin-1 auto-regulation

In case of disrupted phase separation, the functionality of the protein assemblies is disturbed and therefore a proliferative/neoplastic disease can develop. Since the mutated residue 816 in our model system is located within our mapped binding interface of Axin-1^{DIX} to Axin-1^{IDR}, but not the Axin-1^{DIX} Axin-1^{DIX} homo-oligomerization interface, it is conceivable that those interactions are essential for proper phase separation. In cell biology experiments, deletions of BS 1-3 in the cancer variant of Axin-1 were able to restore *puncta* formation. In addition in those protein constructs, Wnt pathway activation was suppressed comparable to wildtype level. (Fig. 25 A, B) Those results suggest an important role of the BS in phase separation. However, the exact mechanism how E816 mutation disrupts *puncta* formation, and why BS deletions restore it, is still elusive. It can be speculated, that the interplay of inter- and intra-molecular interactions is the key. Hereby, reduced affinity of Axin-1^{DIX} with E816G mutation disturbs mainly weak trans-interactions, whereas stronger cis-interactions are still feasible. Therefore, intra-molecular interactions within single Axin-1 molecules are favored, thereby reducing the amount of cross-linked Axin-1 molecules. This leads to a severe loss of *puncta* formation. When deleting Axin-1^{IDR} BSs in Axin-1^{E816G}, the equilibrium of inter- and intra-molecular interactions is shifted back due to the reduced affinity within one Axin-1 molecule. Therefore inter- and intra-molecular interactions are again in balance and *puncta* formation is restored.(Fig. 41) This model now extends the already available model by the Xie He lab(63) by further investigation and characterization of the binding sites within the Axin-1^{IDR}. However, we hypothesize that phosphorylation does not actively interfere with the binding of Axin-1^{IDR}, mainly because the phosphorylation sites are not located within BS 1-3, but phosphorylation does enhance ß-catenin binding. (Fig. 42)

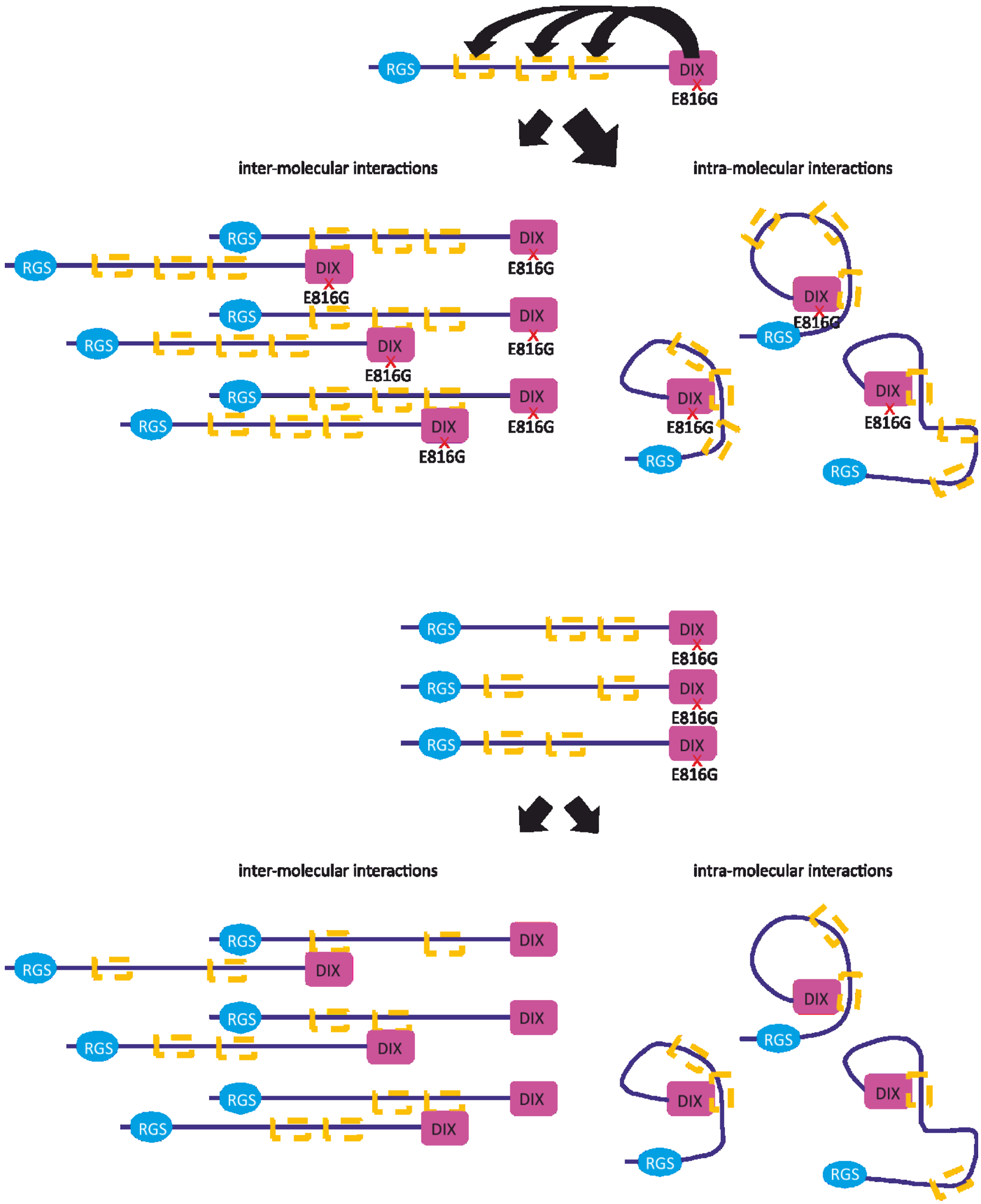

Figure 41: Model for Axin-1 auto-regulation in cancer constructs

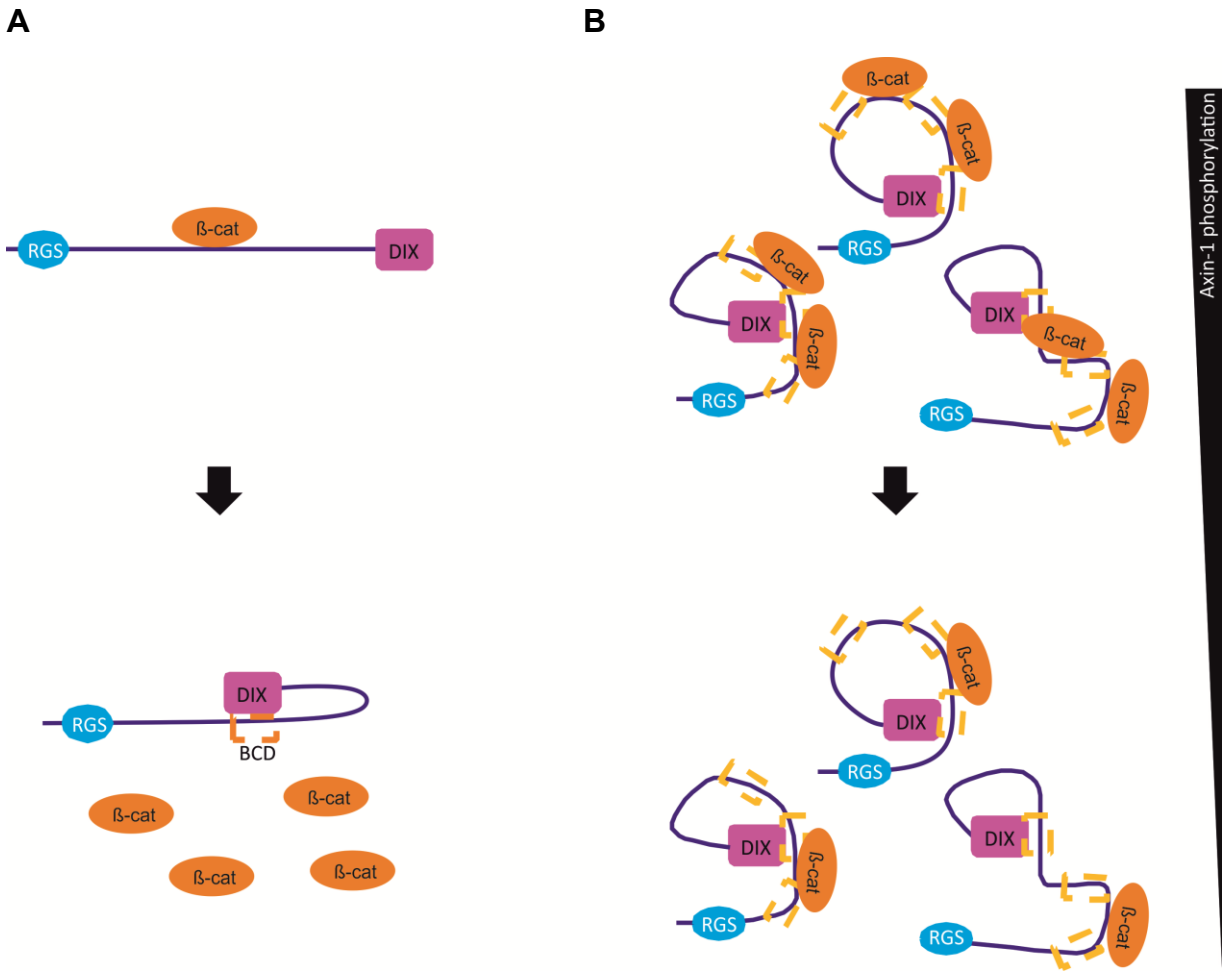

Figure 42: Current models for Axin-1 auto-regulation

A. Model for Axin-1 regulation by the Xie He lab proposing an open conformation of Axin-1 in the phosphorylated state, and a closed conformation in absence of phosphorylation. The closed conformation leads to a ß-catenin displacement from Axin-1^{IDR} by Axin-1^{DIX}.(63) B. New model based on our experimental findings. There are different intra-molecular binding events of Axin-1^{DIX} to Axin-1^{IDR}, which do not interfere with ß-catenin binding. We propose, that phosphorylation might regulate Axin-1 activity, i.e. by increasing affinity to ß-catenin (based on fluorescence anisotropy results, however, we do not think that the intra-molecular interactions are prevented in the phosphorylated state.

Differences in terms of affinity in fluorescence anisotropy experiments suggest similar roles of BS 1 and 3 in the cancer context, whereas BS 2 does not show an altered affinity in presence of E816G mutation in the Axin-1^{DIX}. However, in cell-based assays, all Axin-1^{IDR} BSs restore *puncta* formation in combination with E816G mutation. Those differences between the *in vitro* fluorescence anisotropy data and the *in situ* cell data/*in vitro* data of the full-length protein can be explained by a distance model. Fluorescence anisotropy *in vitro* experiments, all interactions are measured in trans, in contrast to the cis-interactions in cell-based assays/interactions in TEM/DIC or turbidity experiments. Therefore only sequence related differences will be read out in fluorescence anisotropy, whereas cell-based assays also take the distance within the molecule into account.

Phase separation in Wnt signaling

The Mittag group was the first who introduced a role for phase separation in cancer diseases by investigating the protein SPOP and cancer mutations thereof.(29) In their studies they found a disrupted phase separation as a phenotype for non-functional protein complexes and therefore the development of cancer/neoplastic disorders.(Fig. 1)

Axin-1 also shows disrupted *puncta* formation in cancer variants, as described in literature (72) and in this thesis. Therefore it might be a general concept in protein complexes involved in proliferative processes, that phase separation is a necessary feature in order to provide proper regulation of processes. We show in this work, that *puncta* formation is a phase-separation process, and, at the same time, the group of Mark Peifer published a recent review (36) about the role of biomolecular condensates in Wnt signaling. They assume, that there are parallels of ß-catenin destruction complex assembly and phase separation. Our data about Axin-1 phase separation, in combination with the knowledge in literature that proteins in Wnt signaling, such as Dsh and APC, share common features with proteins involved in phase separation (e.g. multivalency, structured and disordered domains), provide an important proof that this is an legitimate assumption and that extensive studies are needed.

Perspective/open questions

In order to prove and characterize distinct functions of the binding sites in *puncta* formation of Axin-1, we are aiming at further characterizing the BSs by investigating the involvement in phase separation. In order to do this, we established a FRAP setup to study Axin-1-GFP *puncta* and their dynamics. We determined a highly dynamic assembly of Axin-1, which exchanges fast with the environment. (Fig. 43) These experiments, as also already reported in literature (35, 71), provide an important proof that Axin-1 *puncta* have similar properties to other phase separated condensates. For our project it will be of great importance to investigate Axin-1 GFP with deletions of BSs, as well as Axin-1 GFP with five amplifications of the distinct BSs using FRAP. Those experiments will reveal the importance of the distinct BSs for the dynamics of Axin-1 assemblies and will provide the ultimate proof that our mapped interactions are essential for proper phase separation. In addition, if the BS are important for intermolecular interactions, we assume that an Axin-1 construct with five amplifications of BSs will build very rigid and compact phase separated condensates compared to Axin-1 wildtype, due to the increased number of interactions. Those constructs are supposed to show a reduced dynamic exchanges with the environment.

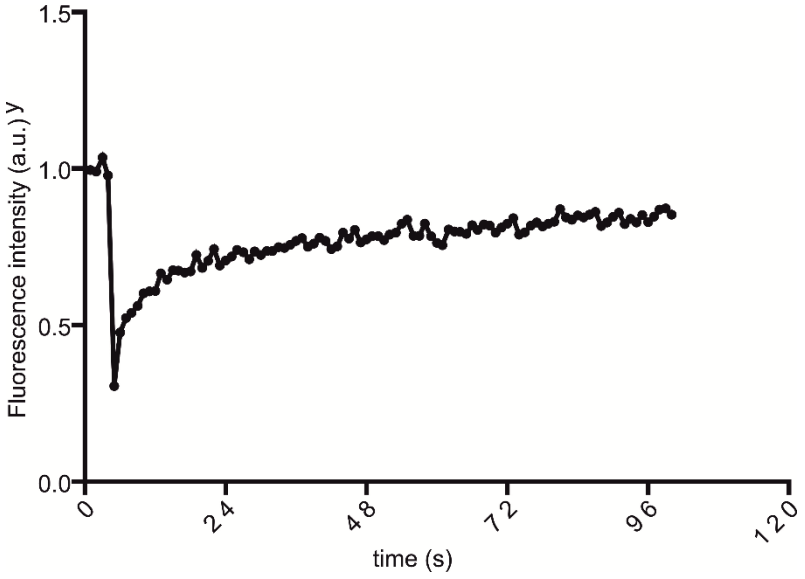

Figure 43: FRAP experiments.
Fluorescence recovery after photobleaching for Axin-1. WT-GFP. 80.5 % recovery, $T_{1/2}$ = 6 s

In addition, in our experiments, deletions of the single BSs did not disturb *puncta* formation. (Fig. 24) Since all three Axin-1^{IDR} fragments bind to the same interface on the Axin-1^{DIX} domain, we assume that in absence of one distinct BS, the other two will compensate for the lack. Therefore, the investigation of a construct lacking all three BSs will provide data on the importance of these sites for phase separation. Assuming that our hypothesis holds true, Axin-1 protein lacking all three binding sites will show loss or at least disturbed phase separation, due to residual Axin-1^{DIX}-Axin-1^{DIX} interactions.

Another approach for further characterization of Axin-1 *puncta* using cell biology experiments will be structured illumination microscopy (SIM, Fig. 44) This super-resolution technique will enable an in-depth characterization of the Axin-1 *puncta* and will help to monitor changes due to alterations in the BSs. Hereby, we hypothesize that the increased number of binding sites will increase the compactness of the network observed in Axin-1. (Fig. 44)

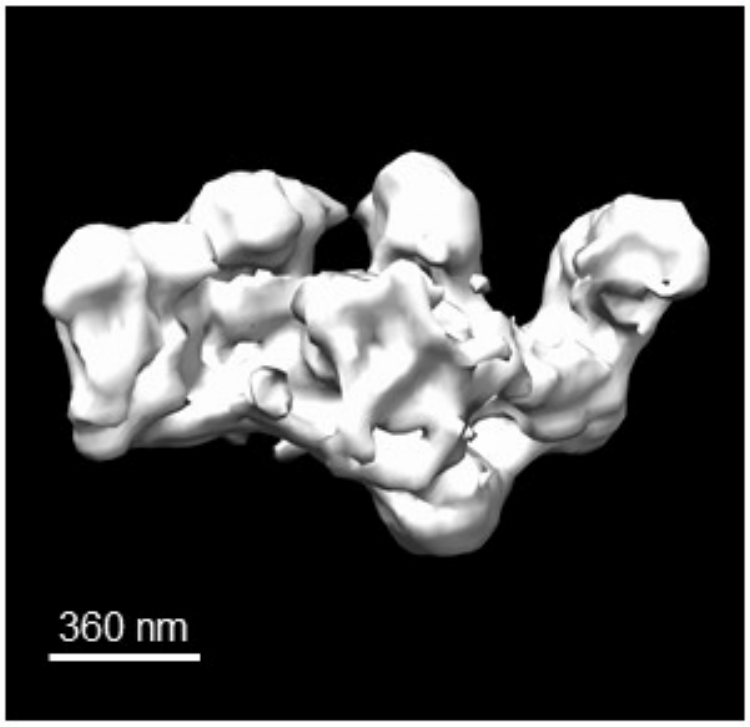

Figure 44: SIM experiments. Axin-1 GFP *puncta* in HeLa cells. 3D - SIM stack has been imaged on a Nikon–Structured Illumination Microscopy (N-SIM®) System.

Restoration of puncta formation as a drug target

Interestingly, the BS in the Axin-1^{DIX} domain is not located within the head-to-tail oligomerization interface. This implicates that in the auto-inhibited state, the oligomerization is still feasible. Our variant of the Axin-1^{DIX} domain with a colorectal cancer mutation (E816G) is located in the Axin-1^{DIX}-Axin-1^{IDR} interface, which entails an altered affinity in presence of the mutation. In line with this, removal of this BS in the E816G variant restores puncta formation. This provides a potent target in order to restore puncta, which is correlating with pathway suppression and therefore a non-proliferating phenotype. Cell-based assays, where a minimal DIX construct harboring the Axin-1^{IDR} interface is administered to cells, will be an important experiment in order to test whether puncta formation can be restored using a drug. Hereby, an excess of a protein harboring the aforementioned sequences will, by increasing local Axin-1 concentrations via Axin-1^{DIX}/Axin-1^{DIX} interactions, enable trans-interactions of Axin-1^{IDR} BS with Axin-1^{DIX}. This approach might mimic the situation of E816G with deletion of Axin-1^{IDR} BSs and restore puncta formation.

Role of the Hrr in Axin-1

Published work of the Xie He lab proposed an open conformation of the tumor suppressor protein Axin-1 in a phosphorylated state, whereas the protein adopts a ‘closed’ conformation in absence of post-translational phosphorylation. Using cell-based assays, the binding event was localized close to the Hrr around residue 540.(63) With a biophysical characterization of the binding events, the BS of the Axin-1^{DIX} within the flexible linker region were mapped and vice versa with amino acid resolution. Based on those experiments, I determined three different BSs in the Axin-1 intrinsically disordered linker region around residue 440, residue 560 and around residue 630, which indicates that not the Hrr, but the adjacent parts (residue 560-570) are directly involved in the binding event. In addition, the Xie He lab revealed the phosphorylation-dependency of this interaction. They found a weakened interaction of the Axin-1^{DIX}-Axin-1^{IDR} in presence of post-translational phosphorylation. We therefore hypothesize,

that the weakening of interaction in absence of the Hrr observed by the Xie He lab is due to a phosphorylation event in the cell-based assays. Histidine residues are positively charged and therefore prone to interact with negatively charged phosphate groups. Therefore, intramolecular long-range interactions within the Axin-1 molecule, where the Hrr interacts with phosphorylated amino acids in Axin-1, could indirectly affect intramolecular interactions. Those effects can be easily picked up in a physiological cell-based assay, but with the amino acid resolution NMR spectroscopy study BS were exactly mapped.

Usually, specific sequence motifs, such as Hrr, have a certain function in cells. However, based on the data in this thesis, the role of the Hrr still remains elusive. Apart from speculations about the phosphate group binding, the stretch of positively charged amino acids can have another cellular function: RNA binding. Different proteins have already been described to bind to RNA via a positively charged stretch, e.g. Hrr.(147) In addition, many proteins that perform phase separation build up assemblies of proteins with RNA.(11-13, 25) Finally, since APC, a member of the ß-catenin destruction complex, which is in close contact with Axin-1, has already been described to be a RNA-binding protein, there could be a cooperative role of Axin-1 for the RNA-binding function.(107)

RNA binding studies of Axin-1 will help to unravel the role of the Hrr in the protein. Hereby a RNA staining (e.g. SYTO™ RNA select green fluorescent cell stain, Invitrogen) will allow to determine the presence of RNA in Axin-1 puncta. In case RNA is detected in the puncta, different RNA sequences can be tested in NMR titrations in order to see which consensus sequence Axin-1 binds, or, if the binding event is a non-specific interaction between the positively charged histidine residues with the negatively charged phosphate backbone of the RNA molecules.

Relevance of overexpression model

All the cell-based experiments in the study have been performed using transient transfection and overexpression of the protein. Upon overexpression, phase separation of Axin-1 becomes visible. One might argue, that we only observe correlations due to overexpression, which is not physiologically relevant. However, endogenous phase separation of Axin-1 has already been observed in combination with inhibited tankyrase.(32, 74) We therefore hypothesize that this model of phase separation is relevant, because until now we are only lacking the resolution to see phase separation of the protein on endogenous level, but also without overexpression, puncta formation can be observed in distinct cases.

Evolutionary conservation of Axin-1

Co-evolution analysis is a method in order to identify residues within protein sequences, which co-adapt. This means that changes in one of the residues is compensated by changes in the other residue during evolution. Since Axin-1^{DIX}, but also Axin-1 Hrr and Axin-1 BS3 are highly conserved (Suppl. Fig. 5), there might be a co-evolutionary coupling of Axin-1^{DIX} with Axin-1 BS 3. When screening Axin-1 sequence by BIS2Analyzer, evolutionary coupling was investigated and residues that co-evolve are colored in the same color. (Fig. 45). Residues in Axin-1^{DIX} are highly conserved, but do only co-evolve with a few residues in Axin-1^{IDR}.(Fig. 45) There were a few residues in Axin-1^{IDR} C-terminal from residue 700, which co-evolved with Axin-1^{DIX}, and one residue in the H-rich region, which co-evolves with a residue on the very N-terminal part of Axin-1^{DIX}. However, there is no clear co-evolution pattern of Axin-1^{DIX} and Axin-1^{IDR} BS.

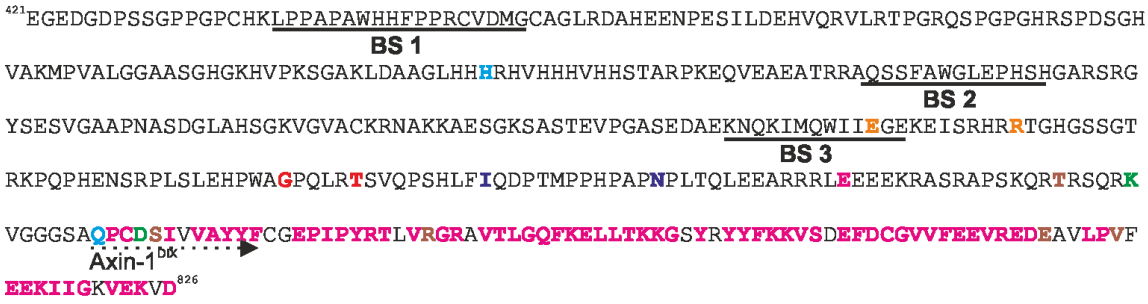

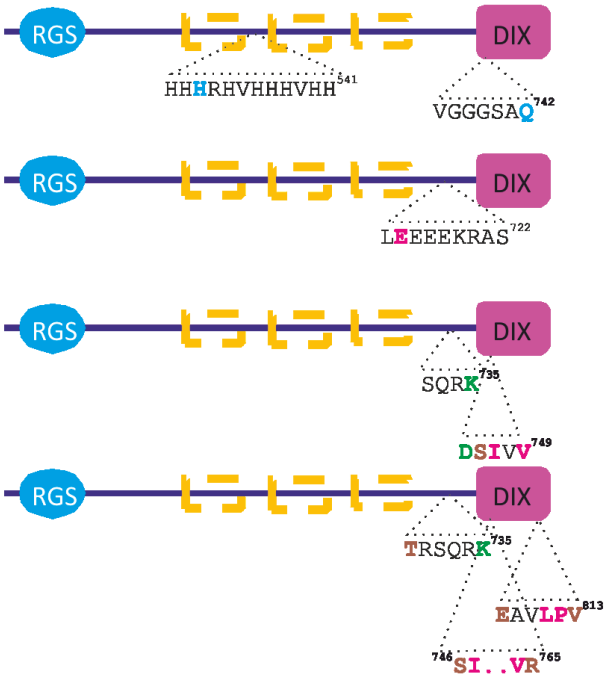

Figure 45: Evolutionary coupling analysis of Axin-1 sequence

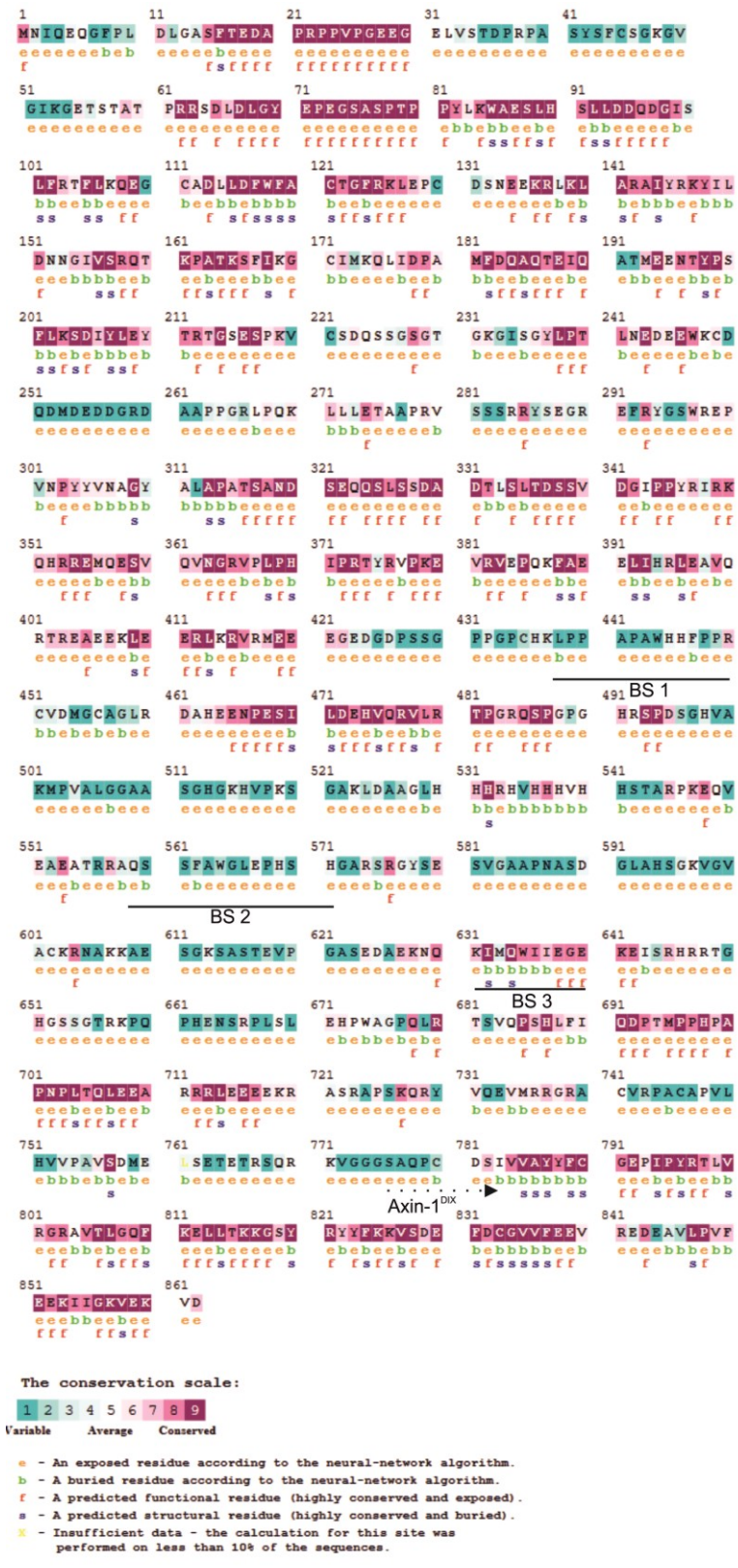

Supplementary figure 5: Evolutionary conservation of Axin-1.

Discussion Part II

NMR spectroscopy as a diagnostic tool

With our study we proved that NMR spectroscopy is a useful tool for the triple-sugar test in urine and that it makes rapid and robust quantification of lactulose, mannitol and sucrose down to low micro-molar concentrations possible (Fig. 38). Clinical relevant concentrations of carbohydrates depend on the lactulose/mannitol ratio, which is >0.07 in a pathological condition.(126, 148) Based on the patient data, that we collected until now, the mannitol concentration in a urine sample is in average around 1000 µM. Taken into account the pathologically increased permeability index, an increased permeability would include a lactulose concentration of at least 70 µM within the same sample. The limit of detection in our setup (38 min) is about 5 µM, which means that a reduction of the measurement time by decreasing the number of scans about factor of 4, we decrease experimental time to <10 minutes and signal-to-noise ratio about a factor of 2, which means that we still detect low concentrated carbohydrates (~ 10 µM). This confirms that our presented protocol is suitable for clinical applications.(6)

Summarizing, this approach does enable the detection of upper digestive tract or intestinal permeability as a hallmark for liver cirrhosis patients, but also for patients suffering from Crohn's disease, celiac disease, Crohn's disease or type 1 diabetes and food allergies.(1, 6) In addition to that, NMR spectroscopy is already important for clinical diagnostics (2-5), and, based on the high reproducibility and analytical robustness of the technique, will gain more and more importance.(99)

PRE agents

The process of spin lattice-relaxation (T_1) is crucial in order to produce quantitative data in NMR spectroscopy.(114) The value for T1 is metabolite –specific and can be determined using zggpw5 pulse sequence preceding a saturation recovery block. In avoidance of false quantitative data due to differences in T_1 relaxation of compounds in a sample, the appropriate magnetization recovery time (D1) between scans needs to be set carefully (d1 ≥ 5*T1) when using a 90° excitation pulse. Therefore, T_1 times are the limiting factor regarding measurement times; but it is also a parameter that can be used to optimize the setup of our method. The compounds of interest (carbohydrates, TSP and creatinine) in our study have quite different T_1 times (Fig. 46), therefore the d1 was set to 16 s in order to ensure a proper quantification.
However, addition of PRE agents can be a useful tool in order to reduce T_1 times of the compound. We tested gadolinium chelate and NiDo2A and both of them show promising results by reducing T_1 or enhancing R_1 ($R_1 = 1/T_1$). (Fig. 47). Those data suggest, that the addition of PRE agents is a promising tool to shorten measurement times and therefore to make our setup even faster which is an important property for clinical usage.

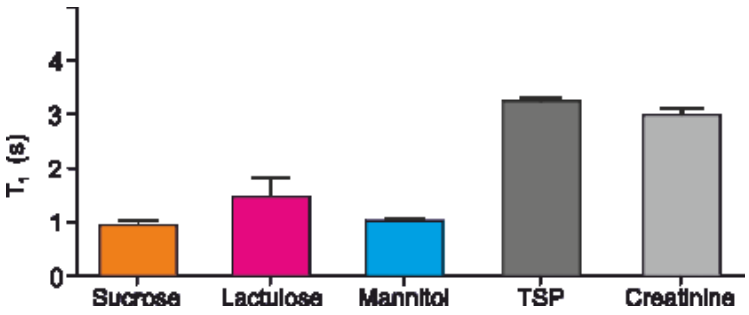

Figure 46: Determined T_1 relaxation times for carbohydrates, internal standard and creatinine. Bar diagram indicating mean T_1 times for carbohydrates, internal standard and creatinine. Data are reprinted from the publication.(6)

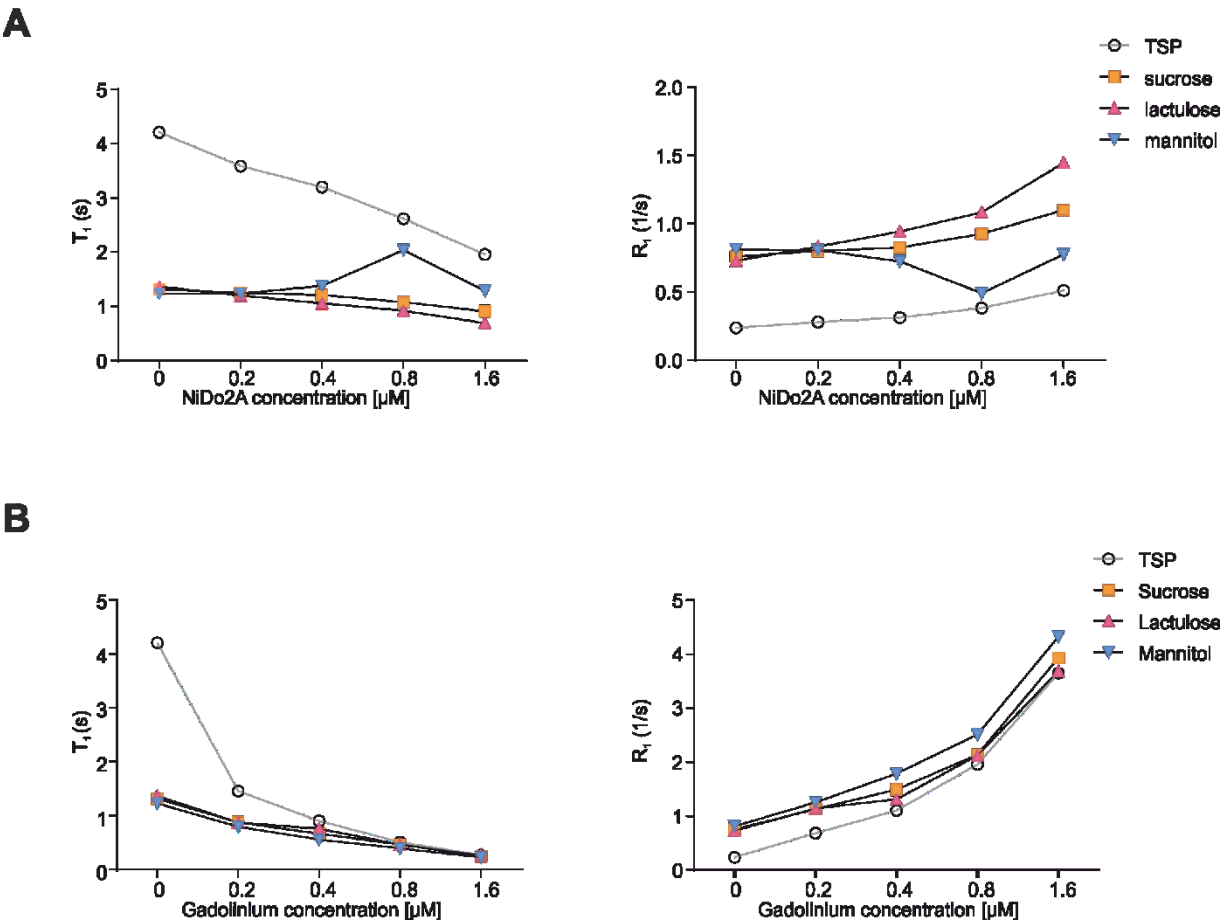

Figure 47: T_1 relaxation times in presence of paramagnetic relaxation enhancers. T_1 times for carbohydrates and TSP in presence of gadolinium chelate and NiDo2A.

Another future implementation might be the ERETIC method (Electronic REference To access *In vivo* Concentrations).(144, 149) This NMR method enables the determination of absolute concentrations by using a reference signal created by an electronic device.(6, 121)

Bibliography

1. Mishra A, Makharia GK. Techniques of functional and motility test: how to perform and interpret intestinal permeability. Journal of neurogastroenterology and motility. 2012;18(4):443-7. PubMed PMID: 23106006. Epub 10/09.
2. Sliz. Screening of Metabolic Disorders using NMR Metabolomics and Whole Genome Sequencing. BioRxiv. 2018.
3. Tolstikov V, Akmaev VR, Sarangarajan R, Narain NR, Kiebish MA. Clinical metabolomics: a pivotal tool for companion diagnostic development and precision medicine. Expert Review of Molecular Diagnostics. 2017 2017/05/04;17(5):411-3.
4. Aru V, Lam C, Khakimov B, Hoefsloot HCJ, Zwanenburg G, Lind MV, et al. Quantification of lipoprotein profiles by nuclear magnetic resonance spectroscopy and multivariate data analysis. TrAC Trends in Analytical Chemistry. 2017 2017/09/01/;94:210-9.
5. Aygen S, Dürr U, Hegele P, Kunig J, Spraul M, Schäfer H, et al. NMR-Based Screening for Inborn Errors of Metabolism: Initial Results from a Study on Turkish Neonates. JIMD reports. 2014;16:101-11. PubMed PMID: 25012580. Pubmed Central PMCID: PMC4221306. Epub 2014/07/12. eng.
6. Stryeck S, Horvath A, Leber B, Stadlbauer V, Madl T. NMR spectroscopy enables simultaneous quantification of carbohydrates for diagnosis of intestinal and gastric permeability. Scientific Reports. 2018 2018/10/02;8(1):14650.
7. Lodish H BA, Zipursky SL, et al. Organelles of the Eukaryotic Cell. In: Freeman NYWH, editor. Molecular Cell Biology2000.
8. Mitrea DM, Kriwacki RW. Phase separation in biology; functional organization of a higher order. Cell communication and signaling : CCS. 2016 Jan 5;14:1. PubMed PMID: 26727894. Pubmed Central PMCID: PMC4700675. Epub 2016/01/06. eng.
9. Uversky VN. Intrinsically disordered proteins in overcrowded milieu: Membrane-less organelles, phase separation, and intrinsic disorder. Current opinion in structural biology. 2017 Jun;44:18-30. PubMed PMID: 27838525. Epub 2016/11/14. eng.
10. Alberts B. Cell Biology: The Endless Frontier. Molecular Biology of the Cell. 2010;21(22):3785-. PubMed PMID: 21079009.

11. Hofweber M, Hutten S, Bourgeois B, Spreitzer E, Niedner-Boblenz A, Schifferer M, et al. Phase Separation of FUS Is Suppressed by Its Nuclear Import Receptor and Arginine Methylation. Cell. 2018 Apr 19;173(3):706-19 e13. PubMed PMID: 29677514. Epub 2018/04/21. eng.

12. Murakami T, Qamar S, Lin JQ, Schierle GS, Rees E, Miyashita A, et al. ALS/FTD Mutation-Induced Phase Transition of FUS Liquid Droplets and Reversible Hydrogels into Irreversible Hydrogels Impairs RNP Granule Function. Neuron. 2015 Nov 18;88(4):678-90. PubMed PMID: 26526393. Pubmed Central PMCID: PMC4660210. Epub 2015/11/04. eng.

13. Patel A, Lee HO, Jawerth L, Maharana S, Jahnel M, Hein MY, et al. A Liquid-to-Solid Phase Transition of the ALS Protein FUS Accelerated by Disease Mutation. Cell. 2015 Aug 27;162(5):1066-77. PubMed PMID: 26317470. Epub 2015/09/01. eng.

14. West JA, Mito M, Kurosaka S, Takumi T, Tanegashima C, Chujo T, et al. Structural, super-resolution microscopy analysis of paraspeckle nuclear body organization. The Journal of cell biology. 2016 Sep 26;214(7):817-30. PubMed PMID: 27646274. Pubmed Central PMCID: PMC5037409. Epub 2016/09/21. eng.

15. McGurk L, Gomes E, Guo L, Mojsilovic-Petrovic J, Tran V, Kalb RG, et al. Poly(ADP-Ribose) Prevents Pathological Phase Separation of TDP-43 by Promoting Liquid Demixing and Stress Granule Localization. Molecular Cell. 2018;71(5):703-17.e9.

16. Feric M, Vaidya N, Harmon TS, Mitrea DM, Zhu L, Richardson TM, et al. Coexisting Liquid Phases Underlie Nucleolar Subcompartments. Cell. 2016 2016/06/16/;165(7):1686-97.

17. Riback JA, Katanski CD, Kear-Scott JL, Pilipenko EV, Rojek AE, Sosnick TR, et al. Stress-Triggered Phase Separation Is an Adaptive, Evolutionarily Tuned Response. Cell. 2017;168(6):1028-40.e19.

18. Protter DSW, Rao BS, Van Treeck B, Lin Y, Mizoue L, Rosen MK, et al. Intrinsically Disordered Regions Can Contribute Promiscuous Interactions to RNP Granule Assembly. Cell Reports. 2018;22(6):1401-12.

19. Han Tina W, Kato M, Xie S, Wu Leeju C, Mirzaei H, Pei J, et al. Cell-free Formation of RNA Granules: Bound RNAs Identify Features and Components of Cellular Assemblies. Cell. 2012 2012/05/11/;149(4):768-79.
20. Li P, Banjade S, Cheng H-C, Kim S, Chen B, Guo L, et al. Phase transitions in the assembly of multivalent signalling proteins. Nature. 2012 03/07/online;483:336.
21. Holehouse AS, Pappu RV. Functional Implications of Intracellular Phase Transitions. Biochemistry. 2018 2018/05/01;57(17):2415-23.
22. Bolognesi B, Lorenzo Gotor N, Dhar R, Cirillo D, Baldrighi M, Tartaglia GG, et al. A Concentration-Dependent Liquid Phase Separation Can Cause Toxicity upon Increased Protein Expression. Cell Reports. 2016 2016/06/28/;16(1):222-31.
23. Brangwynne CP, Eckmann CR, Courson DS, Rybarska A, Hoege C, Gharakhani J, et al. Germline P granules are liquid droplets that localize by controlled dissolution/condensation. Science (New York, NY). 2009 Jun 26;324(5935):1729-32. PubMed PMID: 19460965. Epub 2009/05/23. eng.
24. Fei J, Jadaliha M, Harmon TS, Li ITS, Hua B, Hao Q, et al. Quantitative analysis of multilayer organization of proteins and RNA in nuclear speckles at super resolution. Journal of cell science. 2017 Dec 15;130(24):4180-92. PubMed PMID: 29133588. Pubmed Central PMCID: PMC5769577. Epub 2017/11/15. eng.
25. Brady JP, Farber PJ, Sekhar A, Lin YH, Huang R, Bah A, et al. Structural and hydrodynamic properties of an intrinsically disordered region of a germ cell-specific protein on phase separation. Proceedings of the National Academy of Sciences of the United States of America. 2017 Sep 26;114(39):E8194-E203. PubMed PMID: 28894006. Pubmed Central PMCID: PMC5625912. Epub 2017/09/13. eng.
26. Monterroso B, Zorrilla S, Sobrinos-Sanguino M, Keating CD, Rivas G. Microenvironments created by liquid-liquid phase transition control the dynamic distribution of bacterial division FtsZ protein. Scientific Reports. 2016 10/11/online;6:35140.
27. Molliex A, Temirov J, Lee J, Coughlin M, Kanagaraj AP, Kim HJ, et al. Phase separation by low complexity domains promotes stress granule assembly and drives pathological fibrillization. Cell. 2015 Sep 24;163(1):123-33. PubMed PMID: 26406374. Pubmed Central PMCID: PMC5149108. Epub 2015/09/26. eng.

28. Poulard C, Corbo L, Le Romancer M. Protein arginine methylation/demethylation and cancer. Oncotarget. 2016 Oct 11;7(41):67532-50. PubMed PMID: 27556302. Pubmed Central PMCID: PMC5341895. Epub 2016/08/25. eng.

29. Bouchard JJ, Otero JH, Scott DC, Szulc E, Martin EW, Sabri N, et al. Cancer Mutations of the Tumor Suppressor SPOP Disrupt the Formation of Active, Phase-Separated Compartments. Mol Cell. 2018 Oct 4;72(1):19-36 e8. PubMed PMID: 30244836. Pubmed Central PMCID: PMC6179159. Epub 2018/09/25. eng.

30. Schaefer KN, Bonello TT, Zhang S, Williams CE, Roberts DM, McKay DJ, et al. Supramolecular assembly of the beta-catenin destruction complex and the effect of Wnt signaling on its localization, molecular size, and activity in vivo. PLOS Genetics. 2018;14(4):e1007339.

31. Pronobis MI, Rusan NM, Peifer M. A novel GSK3-regulated APC:Axin interaction regulates Wnt signaling by driving a catalytic cycle of efficient betacatenin destruction. eLife. 2015 Sep 22;4:e08022. PubMed PMID: 26393419. Pubmed Central PMCID: PMC4568445. Epub 2015/09/24. eng.

32. Martino-Echarri E, Brocardo MG, Mills KM, Henderson BR. Tankyrase Inhibitors Stimulate the Ability of Tankyrases to Bind Axin and Drive Assembly of β-Catenin Degradation-Competent Axin Puncta. PLOS ONE. 2016;11(3):e0150484.

33. Sear RP. Phase separation of equilibrium polymers of proteins in living cells. Faraday discussions. 2008;139:21-34; discussion 105-28, 419-20. PubMed PMID: 19048988. Epub 2008/12/04. eng.

34. Sear RP. Dishevelled: a protein that functions in living cells by phase separating. Soft Matter. 2007 (6).

35. Schwarz-Romond T, Fiedler M, Shibata N, Butler PJ, Kikuchi A, Higuchi Y, et al. The DIX domain of Dishevelled confers Wnt signaling by dynamic polymerization. Nature structural & molecular biology. 2007 Jun;14(6):484-92. PubMed PMID: 17529994. Epub 2007/05/29. eng.

36. Schaefer KN, Peifer M. Wnt/Beta-Catenin Signaling Regulation and a Role for Biomolecular Condensates. Developmental cell. 2019 Feb 25;48(4):429-44. PubMed PMID: 30782412. Pubmed Central PMCID: PMC6386181. Epub 2019/02/21. eng.

37. van Amerongen R, Nusse R. Towards an integrated view of Wnt signaling in development. Development (Cambridge, England). 2009 Oct;136(19):3205-14. PubMed PMID: 19736321. Epub 2009/09/09. eng.

38. Woll PS, Morris JK, Painschab MS, Marcus RK, Kohn AD, Biechele TL, et al. Wnt signaling promotes hematoendothelial cell development from human embryonic stem cells. Blood. 2008 Jan 1;111(1):122-31. PubMed PMID: 17875805. Pubmed Central PMCID: PMC2200802. Epub 2007/09/19. eng.

39. Bakre MM, Hoi A, Mong JC, Koh YY, Wong KY, Stanton LW. Generation of multipotential mesendodermal progenitors from mouse embryonic stem cells via sustained Wnt pathway activation. The Journal of biological chemistry. 2007 Oct 26;282(43):31703-12. PubMed PMID: 17711862. Epub 2007/08/23. eng.

40. Kaldis P, Pagano M. Wnt signaling in mitosis. Developmental cell. 2009 Dec;17(6):749-50. PubMed PMID: 20059944. Epub 2010/01/12. eng.

41. Clevers H, Nusse R. Wnt/beta-catenin signaling and disease. Cell. 2012 Jun 8;149(6):1192-205. PubMed PMID: 22682243. Epub 2012/06/12. eng.

42. Nusse R, Varmus HE. Wnt genes. Cell. 1992 Jun 26;69(7):1073-87. PubMed PMID: 1617723. Epub 1992/06/26. eng.

43. Clevers H. Wnt/beta-catenin signaling in development and disease. Cell. 2006 Nov 3;127(3):469-80. PubMed PMID: 17081971. Epub 2006/11/04. eng.

44. Huang YL, Anvarian Z, Doderlein G, Acebron SP, Niehrs C. Maternal Wnt/STOP signaling promotes cell division during early Xenopus embryogenesis. Proceedings of the National Academy of Sciences of the United States of America. 2015 May 5;112(18):5732-7. PubMed PMID: 25901317. Pubmed Central PMCID: PMC4426427. Epub 2015/04/23. eng.

45. MacDonald BT, Tamai K, He X. Wnt/beta-catenin signaling: components, mechanisms, and diseases. Developmental cell. 2009 Jul;17(1):9-26. PubMed PMID: 19619488. Pubmed Central PMCID: PMC2861485. Epub 2009/07/22. eng.

46. He X, Semenov M, Tamai K, Zeng X. LDL receptor-related proteins 5 and 6 in Wnt/beta-catenin signaling: arrows point the way. Development (Cambridge, England). 2004 Apr;131(8):1663-77. PubMed PMID: 15084453. Epub 2004/04/16. eng.

47. Cadigan KM. Wnt-beta-catenin signaling. Current biology : CB. 2008 Oct 28;18(20):R943-7. PubMed PMID: 18957245. Epub 2008/10/30. eng.

48. Cadigan KM. TCFs and Wnt/beta-catenin signaling: more than one way to throw the switch. Current topics in developmental biology. 2012;98:1-34. PubMed PMID: 22305157. Epub 2012/02/07. eng.

49. Komiya Y, Habas R. Wnt signal transduction pathways. Organogenesis. 2008 Apr;4(2):68-75. PubMed PMID: 19279717. Pubmed Central PMCID: PMC2634250. Epub 2009/03/13. eng.

50. Wu G, Huang H, Garcia Abreu J, He X. Inhibition of GSK3 phosphorylation of beta-catenin via phosphorylated PPPSPXS motifs of Wnt coreceptor LRP6. PLoS One. 2009;4(3):e4926. PubMed PMID: 19293931. Pubmed Central PMCID: PMC2654145. Epub 2009/03/19. eng.

51. Chodaparambil JV, Pate KT, Hepler MR, Tsai BP, Muthurajan UM, Luger K, et al. Molecular functions of the TLE tetramerization domain in Wnt target gene repression. The EMBO journal. 2014 Apr 1;33(7):719-31. PubMed PMID: 24596249. Pubmed Central PMCID: PMC4000089. Epub 2014/03/07. eng.

52. Willert J, Epping M, Pollack JR, Brown PO, Nusse R. A transcriptional response to Wnt protein in human embryonic carcinoma cells. BMC developmental biology. 2002 Jul 2;2:8. PubMed PMID: 12095419. Pubmed Central PMCID: PMC117803. Epub 2002/07/04. eng.

53. Daniels DL, Weis WI. Beta-catenin directly displaces Groucho/TLE repressors from Tcf/Lef in Wnt-mediated transcription activation. Nature structural & molecular biology. 2005 Apr;12(4):364-71. PubMed PMID: 15768032. Epub 2005/03/16. eng.

54. Schneikert J, Vijaya Chandra SH, Ruppert JG, Ray S, Wenzel EM, Behrens J. Functional comparison of human adenomatous polyposis coli (APC) and APC-like in targeting beta-catenin for degradation. PLoS One. 2013;8(7):e68072. PubMed PMID: 23840886. Pubmed Central PMCID: PMC3698177. Epub 2013/07/11. eng.

55. Stamos JL, Weis WI. The beta-catenin destruction complex. Cold Spring Harbor perspectives in biology. 2013 Jan 1;5(1):a007898. PubMed PMID: 23169527. Pubmed Central PMCID: PMC3579403. Epub 2012/11/22. eng.

56. Liu C, Kato Y, Zhang Z, Do VM, Yankner BA, He X. beta-Trcp couples beta-catenin phosphorylation-degradation and regulates Xenopus axis formation. Proceedings of the National Academy of Sciences of the United States of America. 1999;96(11):6273-8. PubMed PMID: 10339577.

57. Sakanaka C, Williams LT. Functional domains of axin. Importance of the C terminus as an oligomerization domain. The Journal of biological chemistry. 1999 May 14;274(20):14090-3. PubMed PMID: 10318824. Epub 1999/05/13. eng.

58. Noutsou M, Duarte AM, Anvarian Z, Didenko T, Minde DP, Kuper I, et al. Critical scaffolding regions of the tumor suppressor Axin1 are natively unfolded. Journal of molecular biology. 2011 Jan 21;405(3):773-86. PubMed PMID: 21087614. Epub 2010/11/23. eng.

59. Luo W, Zou H, Jin L, Lin S, Li Q, Ye Z, et al. Axin contains three separable domains that confer intramolecular, homodimeric, and heterodimeric interactions involved in distinct functions. The Journal of biological chemistry. 2005 Feb 11;280(6):5054-60. PubMed PMID: 15579909. Epub 2004/12/08. eng.

60. Mendoza-Topaz C, Mieszczanek J, Bienz M. The Adenomatous polyposis coli tumour suppressor is essential for Axin complex assembly and function and opposes Axin's interaction with Dishevelled. Open biology. 2011;1(3):110013-. PubMed PMID: 22645652.

61. Spink KE, Polakis P, Weis WI. Structural basis of the Axin-adenomatous polyposis coli interaction. The EMBO journal. 2000 May 15;19(10):2270-9. PubMed PMID: 10811618. Pubmed Central PMCID: PMC384355. Epub 2000/05/16. eng.

62. Schneikert J, Ruppert JG, Behrens J, Wenzel EM. Different Roles for the Axin Interactions with the SAMP versus the Second Twenty Amino Acid Repeat of Adenomatous Polyposis Coli. PLOS ONE. 2014;9(4):e94413.

63. Kim SE, Huang H, Zhao M, Zhang X, Zhang A, Semonov MV, et al. Wnt stabilization of beta-catenin reveals principles for morphogen receptor-scaffold assemblies. Science (New York, NY). 2013 May 17;340(6134):867-70. PubMed PMID: 23579495. Pubmed Central PMCID: PMC3788643. Epub 2013/04/13. eng.

64. Luo W, Peterson A, Garcia BA, Coombs G, Kofahl B, Heinrich R, et al. Protein phosphatase 1 regulates assembly and function of the beta-catenin degradation

complex. The EMBO journal. 2007 Mar 21;26(6):1511-21. PubMed PMID: 17318175. Pubmed Central PMCID: PMC1829374. Epub 2007/02/24. eng.

65. Hsu W, Zeng L, Costantini F. Identification of a domain of Axin that binds to the serine/threonine protein phosphatase 2A and a self-binding domain. The Journal of biological chemistry. 1999 Feb 5;274(6):3439-45. PubMed PMID: 9920888. Epub 1999/01/28. eng.

66. Mariotti L, Templeton CM, Ranes M, Paracuellos P, Cronin N, Beuron F, et al. Tankyrase Requires SAM Domain-Dependent Polymerization to Support Wnt-beta-Catenin Signaling. Mol Cell. 2016 Aug 4;63(3):498-513. PubMed PMID: 27494558. Pubmed Central PMCID: PMC4980433. Epub 2016/08/06. eng.

67. Rada P, Rojo AI, Offergeld A, Feng GJ, Velasco-Martin JP, Gonzalez-Sancho JM, et al. WNT-3A regulates an Axin1/NRF2 complex that regulates antioxidant metabolism in hepatocytes. Antioxidants & redox signaling. 2015 Mar 1;22(7):555-71. PubMed PMID: 25336178. Pubmed Central PMCID: PMC4333636. Epub 2014/10/23. eng.

68. Liu W, Rui H, Wang J, Lin S, He Y, Chen M, et al. Axin is a scaffold protein in TGF-beta signaling that promotes degradation of Smad7 by Arkadia. The EMBO journal. 2006 Apr 19;25(8):1646-58. PubMed PMID: 16601693. Pubmed Central PMCID: PMC1440825. Epub 2006/04/08. eng.

69. Azzolin L, Panciera T, Soligo S, Enzo E, Bicciato S, Dupont S, et al. YAP/TAZ incorporation in the beta-catenin destruction complex orchestrates the Wnt response. Cell. 2014 Jul 3;158(1):157-70. PubMed PMID: 24976009. Epub 2014/07/01. eng.

70. Azzolin L, Zanconato F, Bresolin S, Forcato M, Basso G, Bicciato S, et al. Role of TAZ as mediator of Wnt signaling. Cell. 2012 Dec 21;151(7):1443-56. PubMed PMID: 23245942. Epub 2012/12/19. eng.

71. Schwarz-Romond T, Metcalfe C, Bienz M. Dynamic recruitment of axin by Dishevelled protein assemblies. Journal of cell science. 2007;120(14):2402-12.

72. Anvarian Z, Nojima H, van Kappel EC, Madl T, Spit M, Viertler M, et al. Axin cancer mutants form nanoaggregates to rewire the Wnt signaling network. Nature structural & molecular biology. 2016 Apr;23(4):324-32. PubMed PMID: 26974125. Epub 2016/03/15. eng.

73. Wang S, Yin J, Chen D, Nie F, Song X, Fei C, et al. Small-molecule modulation of Wnt signaling via modulating the Axin-LRP5/6 interaction. Nature chemical biology. 2013 Sep;9(9):579-85. PubMed PMID: 23892894. Epub 2013/07/31. eng.

74. Huang SM, Mishina YM, Liu S, Cheung A, Stegmeier F, Michaud GA, et al. Tankyrase inhibition stabilizes axin and antagonizes Wnt signalling. Nature. 2009 Oct 1;461(7264):614-20. PubMed PMID: 19759537. Epub 2009/09/18. eng.

75. Kim MJ, Chia IV, Costantini F. SUMOylation target sites at the C terminus protect Axin from ubiquitination and confer protein stability. FASEB journal : official publication of the Federation of American Societies for Experimental Biology. 2008;22(11):3785-94. PubMed PMID: 18632848.

76. Lui TT, Lacroix C, Ahmed SM, Goldenberg SJ, Leach CA, Daulat AM, et al. The ubiquitin-specific protease USP34 regulates axin stability and Wnt/beta-catenin signaling. Molecular and cellular biology. 2011 May;31(10):2053-65. PubMed PMID: 21383061. Pubmed Central PMCID: PMC3133363. Epub 2011/03/09. eng.

77. Behrens J, Jerchow BA, Wurtele M, Grimm J, Asbrand C, Wirtz R, et al. Functional interaction of an axin homolog, conductin, with beta-catenin, APC, and GSK3beta. Science (New York, NY). 1998 Apr 24;280(5363):596-9. PubMed PMID: 9554852. Epub 1998/05/09. eng.

78. Salahshor S, Woodgett JR. The links between axin and carcinogenesis. Journal of clinical pathology. 2005 Mar;58(3):225-36. PubMed PMID: 15735151. Pubmed Central PMCID: PMC1770611. Epub 2005/03/01. eng.

79. Dahmen RP, Koch A, Denkhaus D, Tonn JC, Sorensen N, Berthold F, et al. Deletions of AXIN1, a component of the WNT/wingless pathway, in sporadic medulloblastomas. Cancer research. 2001 Oct 1;61(19):7039-43. PubMed PMID: 11585731. Epub 2001/10/05. eng.

80. Kim YD, Park CH, Kim HS, Choi SK, Rew JS, Kim DY, et al. Genetic alterations of Wnt signaling pathway-associated genes in hepatocellular carcinoma. Journal of gastroenterology and hepatology. 2008 Jan;23(1):110-8. PubMed PMID: 18171349. Epub 2008/01/04. eng.

81. Polakis P. Wnt signaling and cancer. Genes & development. 2000 Aug 1;14(15):1837-51. PubMed PMID: 10921899. Epub 2000/08/02. eng.

82. Alkan HF, Walter KE, Luengo A, Madreiter-Sokolowski CT, Stryeck S, Lau AN, et al. Cytosolic Aspartate Availability Determines Cell Survival When Glutamine Is Limiting. Cell metabolism. 2018 Nov 6;28(5):706-20 e6. PubMed PMID: 30122555. Epub 2018/08/21. eng.

83. Horvath A, Leber B, Schmerboeck B, Tawdrous M, Zettel G, Hartl A, et al. Randomised clinical trial: the effects of a multispecies probiotic vs. placebo on innate immune function, bacterial translocation and gut permeability in patients with cirrhosis. Alimentary Pharmacology & Therapeutics. 2016;44(9):926-35.

84. Huber K, Hofer DC, Trefely S, Pelzmann HJ, Madreiter-Sokolowski C, Duta-Mare M, et al. N-acetylaspartate pathway is nutrient responsive and coordinates lipid and energy metabolism in brown adipocytes. Biochimica et biophysica acta Molecular cell research. 2019 Mar;1866(3):337-48. PubMed PMID: 30595160. Epub 2019/01/01. eng.

85. Madreiter-Sokolowski CT, Waldeck-Weiermair M, Bourguignon M-P, Villeneuve N, Gottschalk B, Klec C, et al. Enhanced inter-compartmental Ca2+ flux modulates mitochondrial metabolism and apoptotic threshold during aging. Redox Biology. 2019 2019/01/01/;20:458-66.

86. Schmidt A, Abuzahu J, Carbajo-Lozoya J, Braunisch MC, Koneru N, Bachmann Q, et al. Acetate-free, citrate-acidified bicarbonate dialysis improves serum calcification propensity—a preliminary study. Nephrology Dialysis Transplantation. 2018;33(11):2043-51.

87. Stadlbauer V, Horvath A, Komarova I, Schmerboeck B, Feldbacher N, Wurm S, et al. A single alcohol binge impacts on neutrophil function without changes in gut barrier function and gut microbiome composition in healthy volunteers. PLOS ONE. 2019;14(2):e0211703.

88. Fan TW, Lane AN. Applications of NMR spectroscopy to systems biochemistry. Progress in nuclear magnetic resonance spectroscopy. 2016 Feb;92-93:18-53. PubMed PMID: 26952191. Pubmed Central PMCID: PMC4850081. Epub 2016/03/10. eng.

89. Kim J, Reed JL. Refining metabolic models and accounting for regulatory effects. Current opinion in biotechnology. 2014 Oct;29:34-8. PubMed PMID: 24632483. Epub 2014/03/19. eng.

90. Bingol K, Brüschweiler R. Multidimensional Approaches to NMR-Based Metabolomics. Analytical Chemistry. 2014 2014/01/07;86(1):47-57.

91. Lashinger LM, O'Flanagan CH, Dunlap SM, Rasmussen AJ, Sweeney S, Guo JY, et al. Starving cancer from the outside and inside: separate and combined effects of calorie restriction and autophagy inhibition on Ras-driven tumors. Cancer & metabolism. 2016;4:18. PubMed PMID: 27651895. Pubmed Central PMCID: PMC5025535. Epub 2016/09/22. eng.

92. Redmann M, Benavides GA, Berryhill TF, Wani WY, Ouyang X, Johnson MS, et al. Inhibition of autophagy with bafilomycin and chloroquine decreases mitochondrial quality and bioenergetic function in primary neurons. Redox Biol. 2017 Apr;11:73-81. PubMed PMID: 27889640. Pubmed Central PMCID: PMC5124357. Epub 2016/11/28. eng.

93. Zhao J, Wu X, Nie S, Gao X, Sun J, Li K, et al. Association of CDKN2B-AS1 rs1333049 with Brain Diseases: A Case-control Study and a Meta-analysis. Clinical psychopharmacology and neuroscience : the official scientific journal of the Korean College of Neuropsychopharmacology. 2017 Feb 28;15(1):53-8. PubMed PMID: 28138111. Pubmed Central PMCID: PMC5290720. Epub 2017/02/01. eng.

94. Worley B, Powers R. Multivariate Analysis in Metabolomics. Current Metabolomics. 2013;1(1):92-107. PubMed PMID: 26078916. Pubmed Central PMCID: PMC4465187. Epub 2013/01/01. eng.

95. Srivastava V, Obudulu O, Bygdell J, Lofstedt T, Ryden P, Nilsson R, et al. OnPLS integration of transcriptomic, proteomic and metabolomic data shows multi-level oxidative stress responses in the cambium of transgenic hipI- superoxide dismutase Populus plants. BMC genomics. 2013 Dec 17;14:893. PubMed PMID: 24341908. Pubmed Central PMCID: PMC3878592. Epub 2013/12/18. eng.

96. Karnovsky A, Weymouth T, Hull T, Tarcea VG, Scardoni G, Laudanna C, et al. Metscape 2 bioinformatics tool for the analysis and visualization of metabolomics and gene expression data. Bioinformatics (Oxford, England). 2012 Feb 1;28(3):373-80.

PubMed PMID: 22135418. Pubmed Central PMCID: PMC3268237. Epub 2011/12/03. eng.

97. Weidt S, Haggarty J, Kean R, Cojocariu CI, Silcock PJ, Rajendran R, et al. A novel targeted/untargeted GC-Orbitrap metabolomics methodology applied to Candida albicans and Staphylococcus aureus biofilms. Metabolomics : Official journal of the Metabolomic Society. 2016;12(12):189. PubMed PMID: 28003796. Pubmed Central PMCID: PMC5097782. Epub 2016/12/23. eng.

98. Aretz I, Meierhofer D. Advantages and Pitfalls of Mass Spectrometry Based Metabolome Profiling in Systems Biology. International journal of molecular sciences. 2016 Apr 27;17(5). PubMed PMID: 27128910. Pubmed Central PMCID: PMC4881458. Epub 2016/04/30. eng.

99. Stryeck S, Birner-Gruenberger R, Madl T. Integrative metabolomics as emerging tool to study autophagy regulation. Microbial cell (Graz, Austria). 2017 Aug 7;4(8):240-58. PubMed PMID: 28845422. Pubmed Central PMCID: PMC5568430. Epub 2017/08/29. eng.

100. Alonso A, Marsal S, Julià A. Analytical methods in untargeted metabolomics: state of the art in 2015. Frontiers in bioengineering and biotechnology. 2015;3:23. PubMed PMID: 25798438. Pubmed Central PMCID: PMC4350445. Epub 2015/03/24. eng.

101. Clarke CJ, Haselden JN. Metabolic Profiling as a Tool for Understanding Mechanisms of Toxicity. Toxicologic Pathology. 2008;36(1):140-7. PubMed PMID: 18337232.

102. Rodriguez-Colman MJ, Schewe M, Meerlo M, Stigter E, Gerrits J, Pras-Raves M, et al. Interplay between metabolic identities in the intestinal crypt supports stem cell function. Nature. 2017 Mar 16;543(7645):424-7. PubMed PMID: 28273069. Epub 2017/03/09. eng.

103. O'Prey J, Sakamaki J, Baudot AD, New M, Van Acker T, Tooze SA, et al. Application of CRISPR/Cas9 to Autophagy Research. Methods in enzymology. 2017;588:79-108. PubMed PMID: 28237120. Epub 2017/02/27. eng.

104. Blaise BJ, Correia G, Tin A, Young JH, Vergnaud AC, Lewis M, et al. Power Analysis and Sample Size Determination in Metabolic Phenotyping. Anal Chem. 2016 May 17;88(10):5179-88. PubMed PMID: 27116637. Epub 2016/04/27. eng.

105. Roessner U, Dias DA. Plant tissue extraction for metabolomics. Methods in molecular biology (Clifton, NJ). 2013;1055:21-8. PubMed PMID: 23963900. Epub 2013/08/22. eng.

106. Sukumaran DK, Garcia E, Hua J, Tabaczynski W, Odunsi K, Andrews C, et al. Standard operating procedure for metabonomics studies of blood serum and plasma samples using a 1H-NMR micro-flow probe. Magnetic resonance in chemistry : MRC. 2009 Dec;47 Suppl 1:S81-5. PubMed PMID: 19688872. Epub 2009/08/19. eng.

107. Preitner N, Quan J, Nowakowski DW, Hancock ML, Shi J, Tcherkezian J, et al. APC is an RNA-binding protein, and its interactome provides a link to neural development and microtubule assembly. Cell. 2014;158(2):368-82. PubMed PMID: 25036633.

108. Zhang B, Xie M, Bruschweiler-Li L, Bingol K, Bruschweiler R. Use of Charged Nanoparticles in NMR-Based Metabolomics for Spectral Simplification and Improved Metabolite Identification. Anal Chem. 2015 Jul 21;87(14):7211-7. PubMed PMID: 26087125. Pubmed Central PMCID: PMC5358793. Epub 2015/06/19. eng.

109. Tayyari F, Gowda GA, Gu H, Raftery D. 15N-cholamine--a smart isotope tag for combining NMR- and MS-based metabolite profiling. Anal Chem. 2013 Sep 17;85(18):8715-21. PubMed PMID: 23930664. Pubmed Central PMCID: PMC3803152. Epub 2013/08/13. eng.

110. Kind T, Cho E, Park TD, Deng N, Liu Z, Lee T, et al. Interstitial Cystitis-Associated Urinary Metabolites Identified by Mass-Spectrometry Based Metabolomics Analysis. Sci Rep. 2016 Dec 15;6:39227. PubMed PMID: 27976711. Pubmed Central PMCID: PMC5156939. Epub 2016/12/16. eng.

111. Ravanbakhsh S, Liu P, Bjorndahl TC, Mandal R, Grant JR, Wilson M, et al. Correction: Accurate, Fully-Automated NMR Spectral Profiling for Metabolomics. PLoS One. 2015;10(7):e0132873. PubMed PMID: 26222058. Pubmed Central PMCID: PMC4519291. Epub 2015/07/30. eng.

112. Bingol K, Bruschweiler R. Two elephants in the room: new hybrid nuclear magnetic resonance and mass spectrometry approaches for metabolomics. Current opinion in clinical nutrition and metabolic care. 2015 Sep;18(5):471-7. PubMed PMID: 26154280. Pubmed Central PMCID: PMC4533976. Epub 2015/07/15. eng.

113. Markley JL, Bruschweiler R, Edison AS, Eghbalnia HR, Powers R, Raftery D, et al. The future of NMR-based metabolomics. Current opinion in biotechnology. 2017 Feb;43:34-40. PubMed PMID: 27580257. Pubmed Central PMCID: PMC5305426. Epub 2016/09/01. eng.

114. Jurkiewicz A, Maciel GE. 13C NMR Spin-Lattice Relaxation Properties and Quantitative Analytical Methodology of 13C NMR Spectroscopy for Coals. Analytical Chemistry. 1995 1995/07/01;67(13):2188-94.

115. Dajani R, Fraser E, Roe SM, Yeo M, Good VM, Thompson V, et al. Structural basis for recruitment of glycogen synthase kinase 3beta to the axin-APC scaffold complex. The EMBO journal. 2003;22(3):494-501. PubMed PMID: 12554650.

116. Qin N, Yang F, Li A, Prifti E, Chen Y, Shao L, et al. Alterations of the human gut microbiome in liver cirrhosis. Nature. 2014 Sep 4;513(7516):59-64. PubMed PMID: 25079328. Epub 2014/08/01. eng.

117. Sharma S, Khalili K, Nguyen GC. Non-invasive diagnosis of advanced fibrosis and cirrhosis. World journal of gastroenterology. 2014 Dec 7;20(45):16820-30. PubMed PMID: 25492996. Pubmed Central PMCID: PMC4258552. Epub 2014/12/11. eng.

118. Barnett R. Liver cirrhosis. Lancet (London, England). 2018 Jul 28;392(10144):275. PubMed PMID: 30064644. Epub 2018/08/02. eng.

119. Hobson CH, Butt TJ, Ferry DM, Hunter J, Chadwick VS, Broom MF. Enterohepatic circulation of bacterial chemotactic peptide in rats with experimental colitis. Gastroenterology. 1988 Apr;94(4):1006-13. PubMed PMID: 3345870. Epub 1988/04/01. eng.

120. Ferry DM, Butt TJ, Broom MF, Hunter J, Chadwick VS. Bacterial chemotactic oligopeptides and the intestinal mucosal barrier. Gastroenterology. 1989 Jul;97(1):61-7. PubMed PMID: 2498147. Epub 1989/07/01. eng.

121. Lunn PG, Northrop CA, Northrop AJ. Automated enzymatic assays for the determination of intestinal permeability probes in urine. 2. Mannitol. Clinica chimica

acta; international journal of clinical chemistry. 1989 Aug 15;183(2):163-70. PubMed PMID: 2507200. Epub 1989/08/15. eng.

122. Hossain MI, Nahar B, Hamadani JD, Ahmed T, Roy AK, Brown KH. Intestinal mucosal permeability of severely underweight and nonmalnourished Bangladeshi children and effects of nutritional rehabilitation. Journal of pediatric gastroenterology and nutrition. 2010;51(5):638-44. PubMed PMID: 20871416.

123. Vogt A, Reuken PA, Stengel S, Stallmach A, Bruns T. Dual-sugar tests of small intestinal permeability are poor predictors of bacterial infections and mortality in cirrhosis: A prospective study. World journal of gastroenterology. 2016;22(11):3275-84. PubMed PMID: 27004006. Epub 03/21.

124. Giofre MR, Meduri G, Pallio S, Calandra S, Magnano A, Niceforo D, et al. Gastric permeability to sucrose is increased in portal hypertensive gastropathy. European journal of gastroenterology & hepatology. 2000 May;12(5):529-33. PubMed PMID: 10833096. Epub 2000/06/01. eng.

125. Kubica P, Kot-Wasik A, Wasik A, Namiesnik J, Landowski P. Modern approach for determination of lactulose, mannitol and sucrose in human urine using HPLC-MS/MS for the studies of intestinal and upper digestive tract permeability. Journal of chromatography B, Analytical technologies in the biomedical and life sciences. 2012 Oct 15;907:34-40. PubMed PMID: 22985725. Epub 2012/09/19. eng.

126. Hessels J, Snoeyink EJ, Platenkamp AJ, Voortman G, Steggink J, Eidhof HH. Assessment of intestinal permeability: enzymatic determination of urinary mannitol, raffinose, sucrose and lactose on Hitachi analyzer. Clinical chemistry and laboratory medicine. 2003 Jan;41(1):33-8. PubMed PMID: 12636047. Epub 2003/03/15. eng.

127. Jayalakshmi K, Ghoshal UC, Kumar S, Misra A, Roy R, Khetrapal CL. Assessment of small intestinal permeability using 1H-NMR spectroscopy. Journal of gastrointestinal and liver diseases : JGLD. 2009 Mar;18(1):27-32. PubMed PMID: 19337630. Epub 2009/04/02. eng.

128. Kumar D, Pandey G, Bansal D, Rawat A, Kumar U, Dubey D, et al. NMR-based urinary profiling of lactulose/mannitol ratio used to assess the altered intestinal permeability in acute on chronic liver failure (ACLF) patients. Magnetic resonance in

chemistry : MRC. 2017 Apr;55(4):289-96. PubMed PMID: 27623987. Epub 2016/09/15. eng.

129. Fiedler M, Mendoza-Topaz C, Rutherford TJ, Mieszczanek J, Bienz M. Dishevelled interacts with the DIX domain polymerization interface of Axin to interfere with its function in down-regulating β-catenin. Proceedings of the National Academy of Sciences. 2011;108(5):1937-42.

130. Delaglio F, Grzesiek S, Vuister GW, Zhu G, Pfeifer J, Bax A. NMRPipe: A multidimensional spectral processing system based on UNIX pipes. Journal of Biomolecular NMR. 1995 November 01;6(3):277-93.

131. Vranken WF, Boucher W, Stevens TJ, Fogh RH, Pajon A, Llinas M, et al. The CCPN data model for NMR spectroscopy: development of a software pipeline. Proteins. 2005 Jun 1;59(4):687-96. PubMed PMID: 15815974. Epub 2005/04/09. eng.

132. Tamiola K, Acar B, Mulder FA. Sequence-specific random coil chemical shifts of intrinsically disordered proteins. Journal of the American Chemical Society. 2010 Dec 29;132(51):18000-3. PubMed PMID: 21128621. Epub 2010/12/07. eng.

133. Oteri F, Nadalin F, Champeimont R, Carbone A. BIS2Analyzer: a server for co-evolution analysis of conserved protein families. Nucleic acids research. 2017 Jul 3;45(W1):W307-W14. PubMed PMID: 28472458. Pubmed Central PMCID: PMC5570204. Epub 2017/05/05. eng.

134. Sievers F, Wilm A, Dineen D, Gibson TJ, Karplus K, Li W, et al. Fast, scalable generation of high-quality protein multiple sequence alignments using Clustal Omega. Molecular systems biology. 2011;7:539. PubMed PMID: 21988835. Pubmed Central PMCID: PMC3261699. Epub 2011/10/13. eng.

135. Armon A, Graur D, Ben-Tal N. ConSurf: an algorithmic tool for the identification of functional regions in proteins by surface mapping of phylogenetic information. Journal of molecular biology. 2001 Mar 16;307(1):447-63. PubMed PMID: 11243830. Epub 2001/03/13. eng.

136. Buhner S, Reese I, Kuehl F, Lochs H, Zuberbier T. Pseudoallergic reactions in chronic urticaria are associated with altered gastroduodenal permeability. Allergy. 2004;59(10):1118-23.

137. Sakhaii P, Bermel W. Improving the sensitivity of conventional spin echo spectra by preservation of initial signal-to-noise ratio. Journal of magnetic resonance (San Diego, Calif : 1997). 2014 May;242:220-3. PubMed PMID: 24694868. Epub 2014/04/04. eng.

138. Martinez A, Bourdreux F, Riguet E, Nuzillard JM. High-resolution and high-sensitivity 2D homonuclear J-resolved NMR spectroscopy. Magn Reson Chem. 2012 Jan;50(1):28-32. PubMed PMID: 22271331. Epub 2012/01/25. eng.

139. Nuzillard J-M. Time-reversal of NMR signals by linear prediction. application to phase-sensitive homonuclear J-resolved spectroscopy. Journal of magnetic resonance (San Diego, Calif : 1997). 1996 1996/01/01/;118(1):132-5.

140. Chong J, Soufan O, Caraus I, Xia J, Li C, Wishart DS, et al. MetaboAnalyst 4.0: towards more transparent and integrative metabolomics analysis. Nucleic acids research. 2018;46(W1):W486-W94.

141. http://www.cbioportal.org/.

142. http://cancer.sanger.ac.uk/cosmic/gene/overview?ln=AXIN1.

143. Shibata N, Tomimoto Y, Hanamura T, Yamamoto R, Ueda M, Ueda Y, et al. Crystallization and preliminary X-ray crystallographic studies of the axin DIX domain. Acta crystallographica Section F, Structural biology and crystallization communications. 2007 Jun 1;63(Pt 6):529-31. PubMed PMID: 17554179. Pubmed Central PMCID: PMC2335085. Epub 2007/06/08. eng.

144. Albers MJ, Butler TN, Rahwa I, Bao N, Keshari KR, Swanson MG, et al. Evaluation of the ERETIC method as an improved quantitative reference for 1H HR-MAS spectroscopy of prostate tissue. Magnetic resonance in medicine. 2009 Mar;61(3):525-32. PubMed PMID: 19235261. Pubmed Central PMCID: PMC2879886. Epub 2009/02/24. eng.

145. Xing Y, Clements WK, Kimelman D, Xu W. Crystal structure of a beta-catenin/axin complex suggests a mechanism for the beta-catenin destruction complex. Genes & development. 2003 Nov 15;17(22):2753-64. PubMed PMID: 14600025. Pubmed Central PMCID: PMC280624. Epub 2003/11/06. eng.

146. http://cancer.sanger.ac.uk/cosmic/gene/overview?ln=APC.

147. Fukuda K, Watanabe T, Tokisue T, Tsujita T, Nishikawa S, Hasegawa T, et al. Modulation of double-stranded RNA recognition by the N-terminal histidine-rich region of the human toll-like receptor 3. The Journal of biological chemistry. 2008 Aug 15;283(33):22787-94. PubMed PMID: 18544529. Epub 2008/06/12. eng.

148. Del Valle-Pinero AY, Van Deventer HE, Fourie NH, Martino AC, Patel NS, Remaley AT, et al. Gastrointestinal permeability in patients with irritable bowel syndrome assessed using a four probe permeability solution. Clinica chimica acta; international journal of clinical chemistry. 2013 Mar 15;418:97-101. PubMed PMID: 23328210. Pubmed Central PMCID: PMC3594104. Epub 2013/01/19. eng.

149. Akoka S, Barantin L, Trierweiler M. Concentration Measurement by Proton NMR Using the ERETIC Method. Analytical Chemistry. 1999 1999/07/01;71(13):2554-7.

Appendix

Buffers and solutions

Kanamycin (50 mg/ml)

5 g Kanamycin (Applichem Panreac) in 100 ml of MilliQ H_2O

Filter sterilize

(Selective) LB medium

2 % (w/v) lysogeny broth (Roth) (+ 0.1 % (v/v) Kanamycin)

10 x Salt

1 M KH_2PO_4 (VWR 99.8%)

0.5 M K_2HPO_4 (VWR 99.8%)

0.6 M Na_2HPO_4 (Applichem Panreac anhydrous >99%)

0.14 M K_2SO_4 (VWR 99-101%)

pH 7.2 adjusted with HCl (12.2 M) and NaOH (5 M)

Trace element solution

41 mM $CaCl_2$ x 2 H_2O (Applichem Panreac 97%)

22 mM $FeSO_4$ x 7 H_2O (VWR 84%)

6 mM $MnCl_2$ x 4 H_2O (Applichem Panreac)

3 mM $CoCl_2$ x 6 H_2O (Applichem Panreac)

1 mM $ZnSO_4$ x 7 H_2O (VWR 99.9%)

0.1 mM $CuCl_2$ x 2 H_2O (VWR)

0.2 mM $(NH_4)_6Mo_7O_{24}$ x 4 H_2O (VWR 98.5%)

17 mM EDTA (Alfa Aesar 99+%)

Minimal medium

It was used for production of labeled or non-labeled proteins. In case of labeling, ^{15}N and/or ^{13}C isotopes were used.

900 ml MilliQ H_2O

100 ml 10 x Salt

5 ml Trace element solution

5 ml 1 M $MgCl_2$ (Alfa Aesar 99%)

1g $^{15}NH_4Cl$ (Sigma Aldrich 98%)/2 g $^{14}NH_4Cl$ (Alfa Aesar 99.5%)

2g $^{13}C_6H_{12}O_6$ (Cambridge Isotope Laboratories 99%)/ 6 g $C_6H_{12}O_6$ (Roth 99%)

0.1% (w/w) Kanamycin (1000x)

Chook buffer (lysis buffer for structured proteins)

150 mM NaCl (VWR 99.6%)

50 mM Tris (VWR ultra pure)

20 % glycerol (VWR 99%)

20 mM imidazole (Millipore 99.0%)

2 mM BME (Roth 98%)

pH 7.5 adjusted with HCl (12.2 M) and NaOH (5 M)

Urea buffer (lysis buffer for disordered proteins)

150 mM NaCl (VWR 99.6%)

50 mM Tris (VWR ultra pure)

6 M Urea (Roth >99.5%)

20 M imidazole (Millipore 99.0%)

2 mM BME (Roth 98%)

pH 7.5 adjusted with HCl (12.2 M) and NaOH (5 M)

Buffer A

150 mM NaCl (VWR 99.6%)

50 mM Tris (VWR ultra pure)

20 mM imidazole (Millipore 99.0%)

2 mM BME (Roth 98%)

pH 7.5 adjusted with HCl (12.2 M) and NaOH (5 M)

Buffer A'

1 M NaCl (VWR 99.6%)

50 mM Tris (VWR ultra pure)

20 mM imidazole (Millipore 99.0%)

2 mM BME (Roth 98%)

pH 7.5 adjusted with HCl (12.2 M) and NaOH (5 M)

Buffer B'

1 M NaCl (VWR 99.6%)

50 mM Tris (VWR ultra pure)

500 mM imidazole (Millipore 99.0%)

2 mM BME (Roth 98%)

pH 7.5 adjusted with HCl (12.2 M) and NaOH (5 M)

NMR buffer

150 mM NaCl (VWR 99.6%)

50 mM Na_2HPO_4/NaH_2PO_4 (VWR ultra pure)

2 mM DTT (Roth 98%)

pH 6.5 adjusted with HCl (12.2 M) and NaOH (5 M)

ß-catenin buffer

150 mM NaCl (VWR 99.6%)

50 mM Tris (VWR ultra pure)

2 mM DTT (Roth 98%)

pH 7.5 adjusted with HCl (12.2 M) and NaOH (5 M)

Blocking buffer for immunofluorescence microcopy

2% BSA

0.1% saponin

dissolved in PBS

NMR-based metabolomics buffer

0.08 M Na_2HPO_4 (Applichem/A2943,1000)

0.04 % NaN3 (Merck/1.06688.0100)

5 mM TSP (Eurisotop/D219PF)

Dissolved in ^2H_2O (SIAL/151882-1)

pH 7.3 adjusted with HCl (12.2 M) and NaOH (5 M)

NMR-based metabolomics buffer for urine

1.5 M KH_2PO_4 (VWR/26936.293)

2 mM NaN_3 (Merck/1.06688.0100)

0,1 % TSP (Eurisotop/D219PF)

Dissolved in ^2H_2O (SIAL/151882-1)

pH 7.3 adjusted with HCl (12.2 M) and NaOH (5 M)

List of publications and licences

Sarah Stryeck, Angela Horvath, Bettina Leber, Vanessa Stadlbauer, Tobias Madl. NMR spectroscopy enables simultaneous quantification of carbohydrates for diagnosis of intestinal and gastric permeability. Scientific Reports (2018)

Sarah Stryeck, Ruth Birner-Gruenberger, Tobias Madl. Integrative metabolomics as emerging tool to study autophagy regulation. Microbial Cell (2017)